

FINAL REPORT

Precision Geolocation of Active Electromagnetic Sensors Using Stationary Magnetic Sensors

SERDP Project MM-1643

SEPTEMBER 2009

Dr. Stephen Billings
Sky Research, Inc.

Kyle Blay
Keith Leslie
David Tilbrook
CSIRO

This document has been approved for public release.



SERDP

Strategic Environmental Research and
Development Program

This report was prepared under contract to the Department of Defense Strategic Environmental Research and Development Program (SERDP). The publication of this report does not indicate endorsement by the Department of Defense, nor should the contents be construed as reflecting the official policy or position of the Department of Defense. Reference herein to any specific commercial product, process, or service by trade name, trademark, manufacturer, or otherwise, does not necessarily constitute or imply its endorsement, recommendation, or favoring by the Department of Defense.

REPORT DOCUMENTATION PAGE

Form Approved
OMB No. 0704-0188

The public reporting burden for this collection of information is estimated to average 1 hour per response, including the time for reviewing instructions, searching existing data sources, gathering and maintaining the data needed, and completing and reviewing the collection of information. Send comments regarding this burden estimate or any other aspect of this collection of information, including suggestions for reducing the burden, to the Department of Defense, Executive Services and Communications Directorate (0704-0188). Respondents should be aware that notwithstanding any other provision of law, no person shall be subject to any penalty for failing to comply with a collection of information if it does not display a currently valid OMB control number.

PLEASE DO NOT RETURN YOUR FORM TO THE ABOVE ORGANIZATION.

1. REPORT DATE (DD-MM-YYYY) 29-09-2009	2. REPORT TYPE Final Technical Report	3. DATES COVERED (From - To) May 2008 - September 2009		
4. TITLE AND SUBTITLE Precision Geolocation of Active Electromagnetic Sensors Using Stationary Magnetic Sensors Final Technical Report		5a. CONTRACT NUMBER W912HQ-08-P-0049		
		5b. GRANT NUMBER		
		5c. PROGRAM ELEMENT NUMBER		
6. AUTHOR(S) Dr. Stephen Billings (Sky Research, Inc.) Kyle Blay (CSIRO) Keith Leslie (CSIRO) David Tilbrook (CSIRO)		5d. PROJECT NUMBER MM 1643		
		5e. TASK NUMBER		
		5f. WORK UNIT NUMBER		
7. PERFORMING ORGANIZATION NAME(S) AND ADDRESS(ES) Sky Research, Inc. 445 Dead Indian Memorial Road Ashland, OR 97520		8. PERFORMING ORGANIZATION REPORT NUMBER		
9. SPONSORING/MONITORING AGENCY NAME(S) AND ADDRESS(ES) Strategic Environmental Research and Development Program 901 North Stuart Street, Suite 303 Arlington, VA 22203-1821		10. SPONSOR/MONITOR'S ACRONYM(S)		
		11. SPONSOR/MONITOR'S REPORT NUMBER(S)		
12. DISTRIBUTION/AVAILABILITY STATEMENT unlimited				
13. SUPPLEMENTARY NOTES				
14. ABSTRACT The objective of this project was to conduct a proof-of-principle demonstration that a single, fixed gradiometer or vector magnetometer could track an active EM sensor at sub-centimeter position and sub-degree accuracy over short baselines. We have shown that the concept of locating a UXO cart via the measurement of its transmitter signal is sound. Further work is warranted to develop a more precise system. Some of the areas that we recommend pursuing are: Develop and trial a refined model of the transmitter source for inversion optimization; investigate the potential of other sensors; investigate the observed unexpected limitation in both the fluxgate and SQUID sensor systems' signal to noise ratio; determine the level of accuracy obtainable when the cart is in motion; Develop and trial improved signal processing and inversion algorithms; and investigate the feasibility of using the technique within the marine environment.				
15. SUBJECT TERMS Active EM sensor tracking, fixed gradiometer, vector magnetometer, UXO cart tracking				
16. SECURITY CLASSIFICATION OF: a. REPORT U b. ABSTRACT UU c. THIS PAGE		17. LIMITATION OF ABSTRACT	18. NUMBER OF PAGES 139	19a. NAME OF RESPONSIBLE PERSON Dr. Stephen Billings
				19b. TELEPHONE NUMBER (Include area code) 541-552-5185

Reset

Standard Form 298 (Rev. 8/98)
Prescribed by ANSI Std. Z39-18

EXECUTIVE SUMMARY

The objective of this project was to conduct a proof-of-principle demonstration that a single, fixed gradiometer or vector magnetometer could track an active EM sensor at sub-centimeter position and sub-degree accuracy over short baselines (< 15 m for cued interrogation) and at ~10 cm position accuracy over longer baselines (up to 50 m for application in wooded terrain or underwater). To summarize the project:

- A full-tensor magnetic gradiometer consisting of 4, 3-axis fluxgates was built to test the feasibility of the concept.
- A trial was performed with an EM63 UXO cart, a GPS receiver and the gradiometer instrument and electronics.
- The techniques and inversions applied to the data gathered were successful in locating the position of the cart with an accuracy of better than 20 cm at distances up to 9.1 m. This accuracy was not strongly dependent on distance.
- The measurement error (standard deviation) of the inversions ranged from sub-millimetre at a distance of 2.8 m, increasing to 50 – 300 mm at a distance of 9.1 m. Measurements / inversions were made at a rate of ~ 10 Hz. The measurement error was not uniform in all dimensions, with the spread of the radial component (from the instrument to the cart) being up to 5 times smaller than the spread of the tangential component.
- These measurement errors may be reduced by using more sensitive sensors (such as SQUIDs) and better acquisition electronics / processing.
- Modeling the field produced by a distributed source (EM63 cart) will enable an improvement in the system accuracy, particularly at close range.
- Work on an iterative higher-order gradient estimation and inversion algorithm may improve the basic gradiometer inversion techniques, obviating the need for computationally-heavy optimization techniques.
- Investigations / modeling of different instrument geometries and the possibility of combining two instruments, located at right angles, will improve the system performance.
- Modeling the effectiveness of alternative sensors may result in reduced costs and complexity (e.g. total field gradiometry).
- The effects of differing soil characteristics on the EM waveform were investigated in a theoretical study. Soil susceptibility was the dominant effect with soil conductivity only having a significant effect at large ranges (> 16 m) and conductivities approaching 1 S/m.
- Localization techniques based on magnetic field sensors (as in this study) are significantly less sensitive to soil conductivity than equivalent techniques that utilize coils to measure the time-rate of change of the magnetic field).
- We studied the effect of the secondary field from a large ferrous object on the localization accuracy. For a worst case scenario of a vertical 155 mm projectile located 50 cm directly below the transmitter, we found that the localization error could be

significant (e.g. 4 cm at 5 meters lateral offset). However, for deeper depths, or smaller items, the localization error was generally less than 1 cm at 5 m lateral offset.

- While some preliminary investigation using a SQUID gradiometer showed potential for greater sensitivity than the fluxgate system, the full potential of these sensors was not realised in this trial.

Recommendations:

We have shown that the concept of locating a UXO cart via the measurement of its transmitter signal is sound. Further work is warranted to develop a more precise system. Some of the areas that we recommend pursuing are:

- Develop and trial a refined model of the transmitter source for inversion optimization. This model could be trialled on the already existing data set.
- Investigate the potential of other sensors, including compact SQUID gradiometers and extended total field magnetometers on a ~ 1 m baseline.
- Investigate the observed unexpected limitation in both the fluxgate and SQUID sensor systems' signal to noise ratio (S/N).
- The majority of the trials were performed while the cart was stationary and thus it was possible to reject power lines interference signals using a "stacking" filter. Further investigation is required to determine the level of accuracy obtainable when the cart is in motion where the use of a stacking filter will limit the time resolution to a multiple of the power line period (i.e 16.6 or 20 ms).
- Develop and trial improved signal processing and inversion algorithms.
- Investigate the feasibility of using the technique within the marine environment via controlled laboratory tests and more comprehensive modeling.

TABLE OF CONTENTS

Executive Summary	ii
Table of Contents.....	iv
ACRONYMS.....	x
ACKNOWLEDGEMENTS.....	xi
1. Extended Abstract.....	1
1.1. Summary	5
2. Introduction.....	6
2.1. Motivation for project.....	6
2.2. Preliminary theoretical study	8
2.3. Report scope	8
3. Instrument, Source and System	9
3.1. Instrument Design.....	9
3.2. Reference Frames	10
3.3. Instrument Theory.....	10
3.3.1. Influence on Design.....	10
3.3.2. Instrument Imperfections	12
3.4. EM63 Magnetic Dipole Source	13
3.5. Auxiliary sensors	16
3.5.1. Tilt-meters.....	16
3.5.2. Reference fluxgate	16
3.5.3. SQUID sensor.....	16
3.6. Data Acquisition System	17
3.6.1. Instrument fluxgate offsets	18
3.6.2. Auxiliary sensors	19
3.6.3. Filtering.....	19
4. Inversion techniques	20
4.1. Nara's method.....	20
4.2. Wilson's method	20
4.3. LSQ Optimization.....	20
5. Model	22

5.1.	Limitations and assumptions of the model	22
6.	Calibration	24
7.	CSIRO Trial.....	25
7.1.	Setup	25
7.1.1.	Trial geometry.....	26
7.1.2.	Extraction of fluxgate measurements	28
7.2.	SQUID measurements	30
7.2.1.	Repeat of SQUID measurements.....	31
7.3.	Measurement bandwidth and rate.....	32
7.4.	The magnetic moment of the EM63	32
7.5.	Modeling of EM63 source	33
7.6.	Presentation of results.....	34
7.7.	Sensor measurement statistics	34
7.7.1.	No source	34
7.7.2.	With source	37
7.7.3.	SQUID measurement statistics	39
7.8.	SQUID Results	40
7.9.	Nara's method results	41
7.10.	Wilson inversion	42
7.11.	Wilson inversion with LSQ	43
7.12.	Accuracy and spread in Wilson inversions.....	43
7.12.1.	Standard deviation – Spread	43
7.12.2.	Accuracy – expected value	44
7.13.	Comparisons between data and model.....	45
7.14.	Motion results	46
7.15.	Tilt Results.....	48
8.	Effect of secondary fields on localization.....	50
8.1.	Concept	50
8.2.	B-field response from a conductive/susceptible half-space.....	51
8.3.	dB/dt response from a conductive/susceptible half-space	53
8.4.	Localization error from the half-space.....	54
8.5.	Generalization to other waveforms.....	56
8.6.	Application to the Geonics EM61	56

8.7.	Preliminary look at application in the marine environment	58
8.8.	Localization error caused by ferrous objects	60
9.	Conclusions.....	62
9.1.	Concept	62
9.2.	Accuracy of modelled system.....	62
9.3.	Ideal dipole assumption of the source.....	62
9.4.	SQUID gradiometer.....	62
9.5.	Effect of soil conductivity and susceptibility	63
9.6.	Potential application in the marine environment	63
9.7.	Effect of large ferrous objects.....	64
10.	Future work recommendations	65
10.1.	Improve EM63 / source model	65
10.2.	Iterative higher-order gradient estimation	65
10.3.	Different geometries and multiple instruments	65
10.4.	Total field sensors.....	65
10.5.	SQUID sensors	66
10.6.	Acquisition systems	66
10.7.	Signal processing	66
10.8.	Potential application for underwater positioning.....	67
11.	References.....	68
Appendix A:	Data	69
1.	Summary of the numbered runs	69
2.	Overall results from field trial.....	71
3.	Overall results from field trial (with Nara)	72
4.	Overall results from Model.....	73
5.	Individual Run Results.....	74
6.	Summary of Errors for each run	90
Appendix B:	Evaluating the on-time response of a conducting, permeable half-space	94
Appendix C:	Reproduction of initial feasibility report.....	96

LIST of TABLES

Table 7-1. Positions, fields and estimated dipole moment from fluxgates at two positions at two times during the field trial.....	33
---	----

LIST of FIGURES

Figure 1-1. Photo of trial with EM63 cart and the gradiometer instrument (right).	1
Figure 1-2. Comparison between model and field trial data (left and right, respectively) showing the level of agreement between the two data sets. ‘Actual Position’ was the position of the cart measured via a “100 m” survey tape. A differential Global Positioning System (GPS) system was also used to locate the fixed positions. These ‘GPS Positions’ are more accurate than those determined via the tape and were used in the model results to determine the actual dipole location. These graphs indicate that the Wilson inversion suffers from inaccuracy (offset from the true value) compared to the LSQ technique, but that they both have similar standard deviations (spread of solutions).	2
Figure 3-1. Wireframe render of instrument. Fluxgate ‘B’ centre-top, ‘D’ left, ‘A’ right, and ‘C’ centre-bottom.	9
Figure 3-2. 3D Geometry of the fluxgate-based instrument frame (left) and the practical realisation of the instrument shown in position during a trial (right).	9
Figure 3-3. Waveform produced by the EM63. This was taken from a fluxgate mounted on the EM63 cart itself. The annotations correspond to the magnitude plots in Figure 3-4 below.....	14
Figure 3-4. Peak pulse amplitude for the three parts of the EM63 transmit cycle, illustrating the general decline, sporadic short-term variation, and the different relative magnitudes of the three parts of the cycle pulses.	14
Figure 3-5. Detail of sample counts between recognized pulses.	15
Figure 3-6. Overall delays for a complete run. The random sporadic long-delays are evident....	15
Figure 3-7. Schematic of SQUID gradiometer illustrating general operation.	17
Figure 3-8. Overview of the signal path of the entire system.	17
Figure 3-9. Block diagram of the offset removal electronics used in the acquisition system.	18
Figure 7-1. Overview of the system setup for the field trial.	25
Figure 7-2. Layout of the experiment. The centre of the instrument was actually 160 mm further West than indicated due to the location of the plumb-bob. The photo is from Google Maps.....	27
Figure 7-3. Plot of the different cart positions, comparing hand-measured and GPS measured..	28
Figure 7-4. Impulse response of the measurement extraction technique / filter. The central portion of this response (where zero weighting is applied to the signal) covers the falling edge transition of the transmit pulse, which occurs usually around the 21-22 ms mark. Thus this filter describes the result of taking a 20 sample average of the pulse peak, and subtracting from that average a 20 sample average of the off-time.	29
Figure 7-5. Frequency response of the extraction filter. Good cancellation of any 50 Hz interference is evident, as well as a good rejection of very low frequency noise. The bandwidth of this response is approximately 12 Hz, centred at 11.5 Hz.....	30
Figure 7-6. Extracted SQUID signal for Run #10, eight different sustained voltage levels can be identified (with resets in between).....	31
Figure 7-7. Calculated moments from on-axis measurements of the field produced by the EM63, compared with theoretical predictions using the Biot-Savart law.	34

Figure 7-8. Run #1, the x-axis of the A fluxgate with the EM63 deactivated. The blue trace is the raw data with the DC offset removed; the red is the processed data-stream.	35
Figure 7-9. This plots the raw and processed noise / interference spectra of the A fluxgate during Run #1, with the EM63 deactivated. Note the low frequency (1/f) ramp and 50 Hz spike in the blue plot, which has been successfully attenuated in the processed signal.	36
Figure 7-10. Raw gradient signal for one of the gradiometer baselines on the fluxgates. It's associated spectrum is shown on the right.	37
Figure 7-11. Illustration of the slow variability of the estimated / extracted peak amplitude of the measured pulse.	38
Figure 7-12. Standard deviations of all 12 fluxgate sensors for all runs from the field trial. Generally they range between 0.5 and 0.8 nT, with a few outliers.	38
Figure 7-13. The raw / processed SQUID signals, and raw spectrum, without the EM63 source.	39
Figure 7-14. Spectrum of the raw SQUID gradiometer signal.	39
Figure 7-15. Extracted SQUID signal for Run #10, eight different sustained voltage levels can be identified (with resets in between).	40
Figure 7-16. Illustration of the Nara inversions. They are generally less accurate and suffer from a greater spread than the Wilson and Wilson+LSQ inversions.	41
Figure 7-17. Average condition number of the gradient tensor against distance for each run.	42
Figure 7-18. Two plots of run #14 illustrating the ambiguous solutions (left), and the automatic rejection working (right). (Note: the scales of each axis are not the same.)	42
Figure 7-19. Runs 42 (left) and 14 (right) illustrating the non-symmetric spread (cyan bars) in the components of the solutions, depending on the position of the source.	44
Figure 7-20. These two graphs plot the maximum or minimum standard deviation found (out of all three components of the solution) in all the runs, against the known distance of the EM63 from the instrument.	44
Figure 7-21. Two examples of the model correlating closely with the data. Modelled geometry on the left, actual data on the right.	46
Figure 7-22. Run #36. Cart was walked West across reference marks S-I-E. The cyan line is an extrapolation between points S and E, as measured by the GPS system.	47
Figure 7-23. Run #37. Cart was walked North across reference marks V and N. The cyan line is an extrapolation between points V and N, as measured by the GPS system.	47
Figure 7-24. Tilt-meter vs calculated tilt from moment. While the shapes agree, the magnitude of the tilts do not.	48
Figure 7-25. Tilt-meter signal scaled to match calculated tilt.	49
Figure 8-1. Transmitter waveform for the EM63 showing where B-field and dB/dt measurements would be made.	50
Figure 8-2. B-field response from a half-space of different conductivities/susceptibilities at (a) 4 m from the dipole source; and (b) 32 m distance. The conductivities are given in S/m and the volume susceptibilities in SI.	52
Figure 8-3. Time-evolution of smoke-ring radius for half-spaces of different conductivities.	52
Figure 8-4. B-field (a) dB/dt (b) response from a non-conducting half-space of different susceptibilities (SI units) at 4 meters from the dipole source.	53
Figure 8-5. B-field (a and c) and dB/dt (b and d) response from a half-space of different conductivities and a susceptibility of 0.001 SI at 4 (a and b) and 32 (c and d) meters from the dipole source. The conductivities are given in S/m.	54

Figure 8-6. (a) Effect of conductivity (in S/m) and permeability on localization of the transmitter using the value of the B-field; (b) impact on localization error when using the horizontal gradient of the directed B-field (conductivity = 0 S/m).....	55
Figure 8-7. Effect of conductivity (in mS/m) and permeability on localization of the transmitter on B-field and dB/dt sensors: (a) and (b) compare the localization error at distances of 4 and 32 m respectively; and (c) compares the localization error for a 10 mS/m conductivity at a range is distances from the transmitter.....	55
Figure 8-8. For a B-field sensor, the estimated localization error as a function of time (a) after current initiation for a exponential turn-on at three different distances (4, 16 and 32 m) for a half-space with susceptibility $\chi=0.01$ SI. The results are given in terms of σ/τ which has units of $\text{Sm}^{-1}\text{t}^{-1}$. In (b) the localization error as a function of range at a time of $t=4\tau$ is shown for different conductivities.....	57
Figure 8-9. For a dB/dt sensor, the estimated localization error as a function of time after the start of the linear ramp-off at three different distances (4, 16 and 32 m) for a half-space with susceptibility $\chi=0.01$ SI. The results are given in terms of $\sigma/\Delta t$ which has units of $\text{Sm}^{-1}\text{t}^{-1}$. In (b) the localization error as a function of range at a time of $t=\Delta t$ is shown for different conductivities.....	57
Figure 8-10. The ratio of the B_y (a) and B_z (b) fields in sea-water (4 S/m conductivity) versus free-space as a function of time following the step turn-on of a directed magnetic dipole 5 meters below the receiver at different lateral offsets (in the y-direction). (c) The spatial profile along the y-direction of the magnetic field in free-space (note that $B_x=0$). The time-taken (d) for the sea-water/free-space ratio of B_y to reach 0.1 and 99.9%, for directed magnetic dipoles at 5 and 10 m below the receiver.....	59
Figure 8-11. Estimated worst-case localization errors for (a) a 155 mm projectile and (b) a 81 mm mortar located 0.5 or 1.0 m directly below the transmitter.	61

ACRONYMS

AC	Alternating Current
ADC	Analog to Digital Conversion
AWGN	Additive White Gaussian Noise
Am ²	Ampere-meters squared
cm	Centimeter
CSIRO	Commonwealth Scientific and Industrial Research Organization
DAC	Digital to Analog Converter
DAQ	Data Acquisition System
DC	Direct Current
EM	Electromagnetic
EMI	Electromagnetic Induction
FEM	Frequency Domain Electromagnetic
FIR	Finite Impulse Response
GPS	Global Positioning System
Hz	Hertz
HTS	High Temperature Superconductor
kHz	Kilohertz
LSQ	Least Squares Optimization
m	Meters
µT	microTesla
mm	Millimeters
ms	Millisecond
NI	National Instruments
nT	nanoTesla
pT	picoTesla
RTK	Real Time Kinematic
s	Second
SI	System International
SNR	Signal to Noise Ratio
SQUID	Superconducting Quantum Interference Device
TEM	Time Domain Electromagnetic
Tx	Transmitter
UXO	Unexploded Ordnance
V	Volt

ACKNOWLEDGEMENTS

This technical report for project MM-1643, “*Precision geolocation of active electromagnetic sensors using stationary magnetic sensors*”, documents the results of field measurements and theoretical studies undertaken to test the feasibility of locating an electromagnetic induction device using its magnetic field.

The work was performed by Sky Research, Inc and the Commonwealth Scientific and Industrial Research Organization (CSIRO) Materials Science and Engineering laboratory. Dr Stephen Billings from Sky Research was the principal investigator. Keith Leslie, Kyle Blay and Dr David Tilbrook from CSIRO performed the majority of the work. Dr Leonard Pasion from Sky Research provided numerical codes and assistance with the soil modeling work.

Mr Ryan North of US Army Corps of Engineers, Engineer Research and Development Center, loaned the EM63 cart which was used extensively in the laboratory trials of the system.

Funding for this project was provided by the Strategic Environmental Research and Development Program Office. We wish to express our sincere appreciation to Dr. Jeffrey Marqusee, Dr. Anne Andrews, Dr. Herb Nelson, and staff of the SERDP Office for providing support and funding for this project.

This report was prepared under contract to the Department of Defense Strategic Environmental Research and Development Program. The publication of this report does not indicate endorsement by the Department of Defense, nor should the contents be construed as reflecting the official policy or position of the Department of Defense. Reference herein to any specific commercial product, process, or service by trade name, trademark, manufacturer, or otherwise, does not necessarily constitute or imply its endorsement, recommendation, or favoring by the Department of Defense.

1. Extended Abstract

The Sky Research Inc. and the Commonwealth Scientific and Industrial Research Organization (CSIRO) Materials Science and Engineering laboratory has examined the feasibility of using the magnetic field produced by an unexploded ordnance (UXO) detection cart (EM63) as a means to accurately locate the cart's position using dipole-tracking techniques based on magnetic gradiometry.

In a series of field trials, a full tensor magnetic gradiometer, constructed from four 3-axis vector magnetometers (fluxgates) mounted on a wooden tripod, was used to accurately measure the field produced by the cart while both stationary and in motion. During the stationary trials, the cart was placed at various known positions ranging from between 2.9 meters (m) to 9 m away from the gradiometer. The transmitter waveform signal strengths were measured over a minimum interval of 10 seconds at each position. The measured fields were used to calculate the location of the cart, with respect to the sensor system, using three different dipole-inversion algorithms. Examining the accuracy and spread of the calculated inversions of each algorithm for all cart positions, enabled a comparison of the effectiveness of the algorithms. Two algorithms, Wilson's and a least-squares optimization routine, produced promising results with both techniques locating the cart reliably.

The Wilson inversion uses a single estimate of the magnetic gradient to provide position and orientation of a dipole source. This inversion can be improved by using a least-squares optimization (LSQ) that fits the measurements from all 12 sensors in the instrument to the theoretical dipole field produced by the source (EM63).



Figure 1-1. Photo of trial with EM63 cart and the gradiometer instrument (right).

Modeling of the instrument geometry and inversion techniques indicated that the Wilson inversion suffered from an intrinsic inaccuracy. The assumption of a static gradient field at all parts of the instrument, when in reality the gradient is slightly different at each sensor, produced

an inaccuracy of up to 450 millimeters (mm) in locating the cart. This model was confirmed via the field trial results. The trial solutions correlate well with modelled results, including exhibiting similar inaccuracies. Figure 1-2 demonstrates these predictions, comparing a modelled scenario with the actual results from the trial.

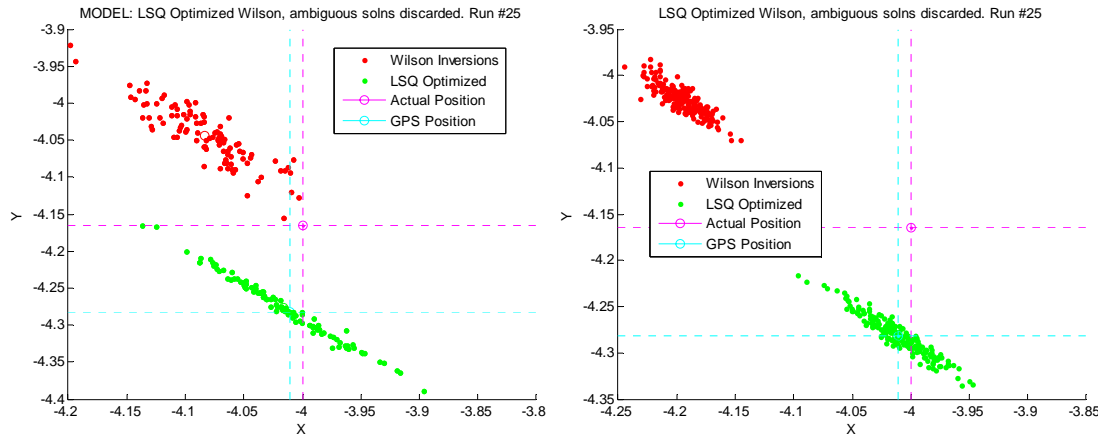


Figure 1-2. Comparison between model and field trial data (left and right, respectively) showing the level of agreement between the two data sets. ‘Actual Position’ was the position of the cart measured via a “100 m” survey tape. A differential Global Positioning System (GPS) system was also used to locate the fixed positions. These ‘GPS Positions’ are more accurate than those determined via the tape and were used in the model results to determine the actual dipole location. These graphs indicate that the Wilson inversion suffers from inaccuracy (offset from the true value) compared to the LSQ technique, but that they both have similar standard deviations (spread of solutions).

Conversely, the model predicted that the LSQ optimized Wilson solutions would converge on the actual position of the dipole source. Figure 1-2 demonstrates the accuracy of this prediction; the LSQ solutions are closer to the actual source than those derived from the Wilson algorithm.

While the accuracy of the instrument with the LSQ algorithm was better than the Wilson inversion and generally better than 150 mm at all distances tested, not all solutions converged on the measured position of the cart. Possible factors affecting the accuracy are:

- Remaining un-calibrated errors in the geometry of the instrument.
- Difficulty in estimating the size of the variable EM63 dipole field.
- The distributed source characteristics of the EM63 which diverges considerably from the assumed dipole nature of the field used in the source locating algorithms.
- Effects of the ground half-space on the shape of the transmit pulse (see section 8).

The standard deviation (spread) of each solution from the measurement of a single pulse of the EM63 was of the order 0.2 – 0.6 mm at a distance of 2.86 m, increasing to 50 – 300 mm at a distance of 9.16 m. Noise estimates of the measured field during the transmitter (Tx) “off” time were measured to be ~ 0.25 nanoTeslas (nT). During the Tx “on” time, these estimates ranged between ~ 0.5 to ~ 1.0 nT. Neither of these compare favorably to the specified noise floor of the fluxgate sensor used (~ 0.025 nT) and thus the level of spread is greater than that predicted by our original theoretical analysis [Appendix C] which suggested that at 9.1 m distance, the radial

spread should be ~ 1 cm (assuming fluxgate noise = 7 pT/ $\sqrt{\text{Hz}}$, with baseline = 0.54 m and signal bandwidth of 10 hertz [Hz]).

It was found that the spread was smaller in the direction of the instrument than it was in the perpendicular, or tangential direction, sometimes by a factor of 6. That is, the distance from the instrument is known with more precision than the position around the instrument. This is evident in Figure 1-2 with the instrument at the origin.

High Temperature Superconducting Quantum Interference Device (HTS SQUID) gradiometers can provide lower intrinsic noise floors than gradiometers based on fluxgates. In a brief trial, an axial HTS gradiometer (Schmidt et al., 2004) was deployed to measure the EM63 cart's magnetic gradient field. The measured standard deviation of the SQUID gradient estimates, without a Tx pulse present, was 0.19 nT / m. This level compares favorably with the measured fluxgate system gradient of 0.71 nT / m. The SQUID noise also demonstrated a flatter noise profile with less low-frequency drift than the fluxgate system.

However, for the SQUID gradiometer, the standard deviation of the gradient estimates measured during the Tx "on" time increased to ~ 1.5 nT / m; an increase of ~ 7 times the "off" time spread and worse than the fluxgate performance (~ 0.5 nT / m). The reason for this increase in spread is currently unknown.

As SQUID gradiometers have smaller baselines and can have intrinsic lower noise than fluxgates, a future direction for research is the design, fabrication and systemization of HTS SQUID-based systems suited to UXO cart tracking. Planar gradiometer systems with intrinsic noise performance of ~ 30 fT / cm / $\sqrt{\text{Hz}}$ (at 1 kHz) are currently being trialed within CSIRO and could form the basis of SQUID-based system.

We investigated the effect of the conductivity and susceptibility of the ground on the location error. Within North America soil conductivity generally lies in the range of 0.5 to 30 mS/m (FCC, 2009). As far as we are aware there is no comprehensive database of soil susceptibility within the United States. Analysis of measurements presented in Van Dam and Velbel (2009) indicate that, within the continental USA, susceptibility would usually lie in the range of 10^{-5} to 0.005 SI. We generated location error estimates for an EM63 like transmitter waveform which comprises an exponentially increasing ramp-up ($\tau=4.3$ ms), followed by a rapid linear ramp-off ($\Delta t=0.1$ millisecond [ms]). The B-field of the primary field is a maximum towards the end of the ramp-up, and we assumed that the B-field was monitored from 25 to 33 ms after pulse turn-on. The dB/dt field is a maximum during the linear ramp-down, and we assumed that the dB/dt field was monitored from 0.05 to 0.1 ms after the start of the ramp-down. We found that for a B-field sensor, conductivity effects are only significant (> 1 cm location error) whenever $\sigma/\tau > 1000$ $\text{Sm}^{-1}\text{t}^{-1}$ and the range is greater than 15 m (e.g. $\sigma=1000$ mS/m and $\tau=1$ ms).

For a dB/dt sensor conductivity effects are important whenever:

- $\sigma/\Delta t > 100$ $\text{Sm}^{-1}\text{t}^{-1}$ at ranges of 15 m or more (e.g. $\sigma=1$ mS/m and $\Delta t=10$ μs , or $\sigma=10$ mS/m and $\Delta t=100$ μs)

- $\sigma/\Delta t > 1000 \text{ Sm}^{-1}\text{t}^{-1}$ at ranges of 5 m or more (e.g. $\sigma=10 \text{ mS/m}$ and $\Delta t=10 \mu\text{s}$, or $\sigma=100 \text{ mS/m}$ and $\Delta t=100 \mu\text{s}$);
- $\sigma/\Delta t > 10000 \text{ Sm}^{-1}\text{t}^{-1}$ at any range (e.g. $\sigma=100 \text{ mS/m}$ and $\Delta t=10 \mu\text{s}$, or $\sigma=1000 \text{ mS/m}$ and $\Delta t=100 \mu\text{s}$).

Soil susceptibility strongly affects the localization error and has the same impact on B-field and dB/dt sensors. Errors of 1 cm or greater are caused whenever:

- $>0.02 \text{ SI}$ at ranges of 4 m or more;
- $>0.008 \text{ SI}$ at ranges of 8 m or more;
- $>0.004 \text{ SI}$ at ranges of 16 m or more;
- $>0.002 \text{ SI}$ at ranges of 32 m or more.

A ten-fold increase in the susceptibility will cause a 10 fold increase in the localization error at a given range. For example a susceptibility of 0.04 SI will cause a 10 cm location error at 16 m distance.

We conclude that the relative immunity of the B-field localization technique to conductivity makes it a better choice for this application than a dB/dt sensor.

For underwater positioning in the marine environment the conductivity of the seawater (4 S/m) can impact the localization accuracy. Using a whole-space model we found that:

- 1) Coil based sensors (dB/dt) are unsuitable because of the strong effects of conductivity in the $100 \mu\text{s}$ time-range.
- 2) B-field sensors could be used for positioning of transmitters with EM63 characteristics without undue influence from the sea-water at ranges up to 30-40 meters.
- 3) B-field sensors may be applicable for positioning transmitters with shorter on-times (such as the EM61), although the sea-water conductivity would need to be included in the analysis at ranges exceeding 10 meters.

We studied the effect of the secondary field from a large ferrous object on the localization accuracy. For a worst case scenario of a vertical 155 mm projectile located 50 cm directly below the transmitter, we found that the localization error was 4 cm at 5 meters lateral offset and 15 cm at 20 meters lateral offset. For horizontal orientation, or when the projectile was 1 m below the transmitter, the location error was always smaller than 1 cm at 5 meters and 4 cm at 20 meters. For an 81 mm mortar at 0.5 m below the transmitter, the location error was 0.5 cm at 5 meters and 2 cm at 20 meters.

We would not expect to encounter too many vertical 155 mm projectiles (or larger items) just 50 cm below the transmitter. Thus, while large ferrous objects have the potential to distort the localization results, in practice we don't anticipate that they will be a significant source of error in the localization procedure.

1.1. Summary

We have shown that the concept of locating a UXO cart via the measurement of its transmitter signal is sound. Further work is warranted to develop a more precise system. Some of the areas that we recommend pursuing are:

- Model the non-dipole characteristics of the EM63 (or similar) to incorporate into the inversion algorithms, for a higher accuracy.
- Model / trial the effects of different geometries and multiple instruments to improve the variability of the solutions. (e.g. with two instruments in an L-configuration, can the best estimates of position in each direction be combined?)
- Investigate total-field sensors as an alternative to 3-axis vector magnetometers.
- Investigate small baseline SQUID sensors to improve the noise performance and systematic inaccuracies of the large baseline fluxgate instrument. (5 cm vs. 60 cm)
- Utilize a customized, higher resolution / synchronous sampling system to reduce the level of quantization noise and signal differencing errors introduced by the current use of an asynchronous sampling, 16-bit resolution, ADC.
- Develop and test some more advanced inversion techniques involving iterative estimation of higher-order gradient fields.
- Identify ways to reduce the sensor count without compromising on accuracy or variability.
- Develop / improve the signal processing / estimation process to increase the realised sensitivity of the sensors. Examples include incorporating correlation techniques using the known shape of the transmit waveform and improving the transition-edge timing estimation.
- Investigate the feasibility of using the technique within the marine environment via controlled laboratory tests and more detailed modeling studies.

2. Introduction

The objective of this project was to conduct a proof-of-principle demonstration that a single, fixed gradiometer or vector magnetometer could track an active electromagnetic (EM) sensor at sub-centimeter (cm) position and sub-degree accuracy over short baselines (< 15 m for cued interrogation) and at ~10 cm position accuracy over longer baselines (up to 50 m for application in wooded terrain or underwater). Specific technical objectives were to

- 1) Conduct a paper-study to compare magnetic vector magnetometry against magnetic tensor gradiometry for localizing and tracking a transmitter and receiver coil system with high accuracy. These comparisons will examine the sensitivity, noise-level, orthogonality, band-width and linearity requirements for the two generic types of magnetic field sensors.
- 2) Based on the outcome of this paper study, a sensor will be selected from a range of systems readily available to CSIRO for use in verification of the feasibility of the method. The systems available include conventional 3-axis fluxgates, 3-axis HTS SQUID magnetometers, a unique 2-axis HTS rotating gradiometer systems and planar HTS SQUID gradiometers. The system chosen will be used in a trial to test whether it is possible to achieve sub-cm and sub-degree accuracy in positioning of a transmitter coil.
- 3) Write a report detailing all hardware, software and logistical requirements to develop a magnetic sensor based-system that can meet the required performance specifications.

Each of these objectives was met. The paper-study is reproduced in Appendix C, and this report covers objectives 2) and 3).

2.1. Motivation for project

Electromagnetic Induction (EMI) is generally considered to be the most promising technology for discriminating between UXO and non-UXO items. Techniques for EMI-based discrimination generally depend on the accurate recovery of the parameters of a physics-based model that can reproduce the observed anomaly. The EMI response is typically modeled as a dipole through a magnetic polarization tensor, which provides a model vector to infer target characteristics. Target identification is achieved by using the recovered model parameters as feature vectors in a statistical classification algorithm.

The success of dipole model based discrimination algorithms depends on the accuracy with which the axial and transverse components of the polarization tensor can be estimated. With noisy and inaccurately positioned data it is difficult to constrain the depth and location of the item, leading to considerable uncertainty in the magnitude and ratio of the components of the polarization tensor (e.g. Smith *et al.*, 2004a, 2004b). For instance, when using Geonics EM61 and Held (EM61-HH) data¹, Bell (2005) found that a SNR of 30 dB and positional accuracy on the centimeter level were required for successful discrimination. Bell further argues that the data quality requirements of the EM61-HH are indicative of those required by other sensors such as the production standard 1 m by 0.5 m coil Geonics EM61. Existing methods for positioning EMI

¹ The transmit and receive coils of the EM61-HH are each about 17 cm in diameter

sensors typically involve the use of real-time-kinematic (RTK) GPS or line-of-sight laser technologies such as RTS augmented with pitch and roll measurements from an IMU. These systems typically approach but do not meet the required positional and orientation specifications. The accuracy of laser and GPS based technologies degrades rapidly in non-ideal conditions such as in wooded terrain or underwater. For instance, ESTCP-MM-0129 studied the accuracy of various positional systems in a wooded environment, including GPS, RTS, the ENSCO Ranger System (based on time-modulated ultra-wideband communications) and a GPS system with inertial aiding. These systems were only able to be positioned (on average) with >10 cm accuracy², with positional errors above 30 cm experienced by all tested systems. Thus, there is a need for a system that can accurately position active EM sensors in obstructed environments.

The basis of the concept explored in this proposal is that active EMI sensors generate large, predominantly, dipolar fields and that the direction, strength and gradients of these fields varies in a systematic way as a function of distance, bearing and orientation from the transmitter. The position and orientation of the transmitter can, in principal, be obtained by making either one 3-component vector or one tensor gradient magnetic measurements (assuming the transmitter moment is known). The envisioned deployment scenario for the system is as follows:

- Establish the vector magnetometer or tensor gradiometer in a fixed location;
- Continuously record the vector or gradient field as the active EM sensor moves around collecting data;
- Post-process the data and extract estimates of the transmitter position and orientation during each on-time event (for a time-domain system) or at regular intervals (for a frequency domain system).

Relevant features of the system include:

- Range: The position and orientation accuracy will degrade with distance away from the sensor (magnetic fields decay as $1/r^3$ and gradients as $1/r^4$) and will be dependent on the transmitter moment of the EMI device. While the system could be used for both time (TEM) and frequency (FEM) domain systems we anticipate focusing on TEM as these systems typically have much larger moments, for example:
 - Geonics EM-61 with 0.5 m by 1 m coil has a moment between 156 to 500 ampere-meters squared (Am^2) (high powered);
 - Geonics EM63 with 1 m by 1 m coil has a moment of 1024 Am^2
- Close Range: As the transmitter approaches the sensor, the field will progressively deviate from an ideal dipole and the transmitter shape will need to be taken into account;
- Orientation ambiguity: The dipole field will not change as the transmitter coil rotates in a horizontal plane. Thus the pitch and roll but not the azimuth of the transmitter can be obtained.
- Timing precision: As the system uses the transmitter on-time to position each measurement, the timing precision between position and EM-sensor measurements will be very precise;

² These accuracy tests were for static measurements so are a lower limit on what can be achieved dynamically

- No lever-arm: The system directly positions the transmitter coil itself, so that there is no lever-arm that can potentially degrade the accuracy;
- Number of sensors: In principal the system can operate with a single vector magnetometer or tensor gradiometer and that is our preferred configuration (for ease of deployment). The accuracy and/or range may be extended by deployment of multiple sensors and that is an option we will consider;
- Auxiliary sensors: If the transmitter orientation cannot be determined with the required precision, then an inertial motion unit can be used to measure the pitch and roll.

A central question we will address in the project is whether the sensors can achieve centimeter position accuracy at sufficient range for them to be suitable for area detection and discrimination scenarios. If not, then the system will need to be deployed in a cued-interrogation mode and also for ~ 10 cm level positioning in wooded or underwater scenarios at ranges of 30 m or perhaps greater.

We are aware of one other system for tracking of active EM-devices (O'Neill, 2006). That system uses two spatially separated induction coils and is intended for precise positioning of small coil frequency-domain systems (the Geophex GEM-3) over short baselines of 1-2 meters.

2.2. Preliminary theoretical study

A theoretical study of the feasibility of determining the position of a UXO cart with respect to a magnetic gradient field sensor was undertaken in a preliminary phase of this SEED project [see Appendix C]. This study showed that it is theoretically possible, using fluxgate sensors, to locate the position of an EM63 cart (transmitter moment of ~ 420 Am 2) at a range of 10 m to an accuracy of 4 cm.

2.3. Report scope

This report details the practical aspects of building, calibrating and trialing a fluxgate-based magnetic gradiometer to test the validity of the initial theoretical study. The results show that locating a UXO cart via monitoring its Tx signal is feasible. While the accuracy achieved was less than what was expected from our initial theoretical study, it should be possible, using two appropriately located instruments, to achieve 5 cm accuracy over distances of up to 10 m.

We focused our attention on the positioning issue and did not attempt to recover the transmitter orientation from the measurements.

In this report, the results of trialing three different algorithms to deduce the location of the dipole with respect to the measuring instrument are examined. These algorithms assume that the EM63 Tx source is dipole-like and can be described analytically. This assumption proved to be invalid for distances less than 2 m. At these distances, improved modeling of the extended Tx source is expected to improve the accuracy of cart localization.

3. Instrument, Source and System

There are three main components to these trials. The basic instrument that permits the required measurements of the magnetic field; the dipole source generator which provides the field to be measured; and the system that facilitates the extraction of the useful information from the instrument's sensors.

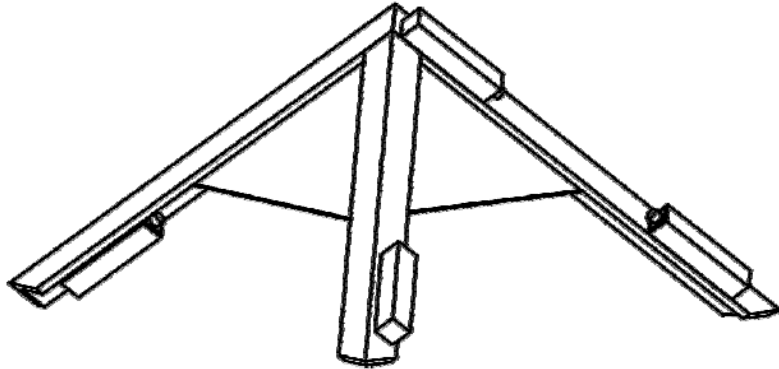


Figure 3-1. Wireframe render of instrument. Fluxgate 'B' centre-top, 'D' left, 'A' right, and 'C' centre-bottom.

3.1. Instrument Design

The instrument chosen was a fluxgate gradiometer design (Figure 3-1). This instrument utilized 4, 3-axis low-noise fluxgates mounted in an orthogonal orientation and separated by baselines of approximately 60 cm. This design was chosen mainly due to the ease of use and availability of high-performance fluxgates (Bartington, MAG-03MSEL70; noise ~ 5 picoTeslas (pT) / $\sqrt{\text{Hz}}$ at 10 Hz). These fluxgate devices are compact, easily mounted in a relatively well-understood orientation and are simple to both power and read-out. An advantage over SQUID systems is that they do not require cryogenic cooling.

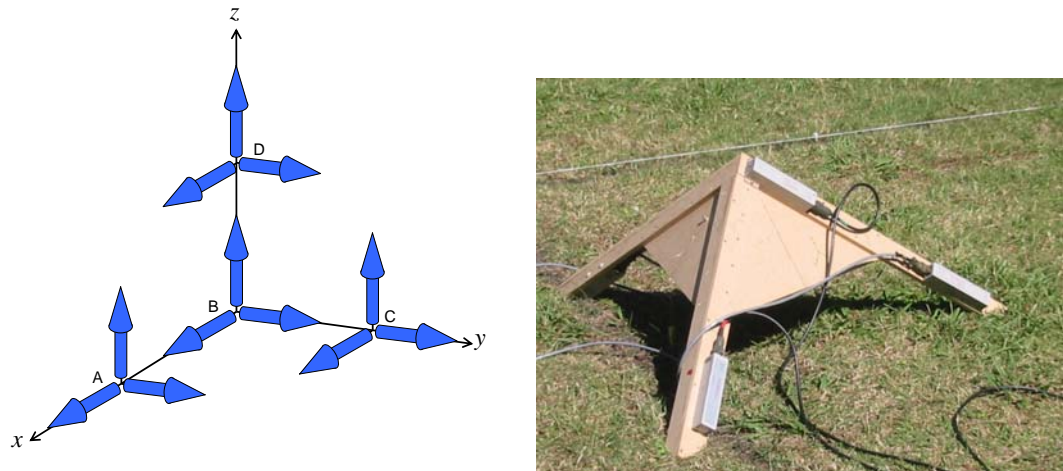


Figure 3-2. 3D Geometry of the fluxgate-based instrument frame (left) and the practical realisation of the instrument shown in position during a trial (right).

The orthogonal geometry and practical implementation of the instrument is illustrated in Figure 3-2. The instrument was constructed using medium-density fibre-board. The design resembles a pyramid / tripod, with a fluxgate at the end of each leg and one at the apex. The legs of the instrument are all nominally orthogonal to each other and thus form the basis for the ‘instrument frame’ of reference. This frame allows the relative displacements of the fluxgates, with respect to the legs and to each other, to be easily measured and recorded. Each fluxgate was assigned a letter designation:

- A** – Placed at the end of the ‘x-axis’ of the instrument frame.
- B** – Placed at the apex or ‘origin’ of the instrument frame.
- C** – Placed at the end of the ‘y-axis’ of the instrument frame.
- D** – Placed at the end of the ‘z-axis’ of the instrument frame.

The specific orientation and location of each fluxgate in its respective position on the instrument was arranged to optimize the accuracy of the gradiometer measurements derived from the fluxgates, and is described below.

3.2. Reference Frames

The instrument’s three wooden legs provide a convenient orthogonal set of axes in which to take and derive measurements. This is known as the ‘instrument frame’ and is described in §3.1. However, it is convenient to consider objects near the instrument in terms of a ‘world frame’, where the ground is considered the x' - y' plane and the z' -axis projects upwards towards the sky. This is compatible with layouts for field trials and GPS measurements. In its natural position on the ground, the three axes of the ‘instrument frame’ of reference project into the ground and do not match the ‘world frame’. Thus a transformation matrix is required to rotate the coordinates / gradients / vectors created in the ‘instrument frame’ into the more useful ‘world frame’.

In our ‘world frame’, the origin is located on the ground directly beneath the vertical apex of the instrument and the y' -axis of the world frame is aligned with the projection of the x -axis of the instrument frame onto the ground / x' - y' plane.

3.3. Instrument Theory

3.3.1. Influence on Design

The instrument was initially designed to enable a simple estimation of the gradient tensor. For this only five independent terms, or five separate baseline measurements were needed from the instrument.

The measurements of interest are highlighted below in bold. The remaining four terms are derived entirely from the first five. For each term, B_{ij} refers to the change of the i^{th} component of the field over the j^{th} dimension, e.g. B_{yz} refers to the change in the magnetic field component aligned with the y -axis per change in the spatial direction of the z -axis.

$$\mathbf{G} = \begin{bmatrix} \mathbf{B}_{xx} & \mathbf{B}_{xy} & \mathbf{B}_{xz} \\ \mathbf{B}_{yx} & \mathbf{B}_{yy} & \mathbf{B}_{yz} \\ \mathbf{B}_{zx} & \mathbf{B}_{zy} & \mathbf{B}_{zz} \end{bmatrix}, \quad \mathbf{B}_{xx} + \mathbf{B}_{yy} + \mathbf{B}_{zz} = 0, \quad \mathbf{B}_{ij} = \mathbf{B}_{ji}$$

G is the 3x3 gradient matrix, the bold terms highlight the minimum required measurements to be made to determine the entire matrix using the two properties of the magnetic gradient tensor – it is both traceless and symmetric.

The placement of the fluxgates on the wooden framed instrument was chosen to optimize sensitivity to the highlighted gradient components.

In particular, it was deemed important to align the A and B fluxgates axially to ensure their baseline was parallel to the x -axis of the instrument. These two fluxgates provide three of the gradient tensor terms (B_{xx} , B_{yx} , B_{zx}). The C fluxgate was aligned to ensure the baseline between the axis components was parallel to the y -axis (B_{zy}), and the D fluxgate was aligned to ensure the baseline between the axis components was parallel to the axis (B_{zz}).

The use of 3-axis fluxgates actually allows for the other 4 terms of the tensor to be calculated. However for these terms, the positioning of the fluxgates is such that the differencing baselines do not line up exactly with an axis of the instrument frame. Deriving these terms is not simply a matter of differencing two fluxgate signals and dividing the result by the baseline. Therefore in the early phase of the project, these terms were not calculated.

Towards the end of the project, a more generalized technique to estimate the gradient was developed. This technique allows measurements from all 12 individual sensors to be used in determining both the magnetic field and its gradient, referenced to the origin of the instrument. The technique assumes that the instrument exists in a static first-order gradient magnetic field. On this basis, each sensors' measurement can be mathematically described in terms of the field at a common reference point, plus the displacement of the fluxgate from the reference point scaled by the gradient. Mathematically,

$$\mathbf{B}_i = \mathbf{B}_{ref} + \mathbf{G} \cdot \mathbf{s}_{ref,i}$$

where \mathbf{B}_i is a 3x1 column vector containing the value of the magnetic field measured by fluxgate i ; \mathbf{B}_{ref} is a 3x1 column vector containing the (unknown) value of the magnetic field at a particular reference point; \mathbf{G} is the 3x3 matrix describing the (unknown) first-order gradient of the magnetic field in the vicinity of the instrument, and $\mathbf{s}_{ref,i}$ is the displacement of fluxgate i with respect to the reference point.

With four fluxgates, these set of four formulas can be combined into a system of 12 equations in 12 unknown variables. However this system is over-determined due to the fact that 9 of these variables, the gradient terms, can be represented wholly by 5 independent variables, thus reducing the system to 12 equations in 8 unknowns. Re-arranging results in the following system of equations:

$$\mathbf{x} = M\mathbf{y}$$

$$\mathbf{y} = (M^T M)^{-1} M^T \mathbf{x}$$

Where,

$$\mathbf{x} = \begin{bmatrix} \mathbf{B}_A \\ \mathbf{B}_B \\ \mathbf{B}_C \\ \mathbf{B}_D \end{bmatrix}, \mathbf{y} = \begin{bmatrix} \mathbf{B}_{ref} \\ B_{xx} \\ B_{xy} \\ B_{xz} \\ B_{yy} \\ B_{yz} \end{bmatrix}, M = \begin{bmatrix} 1 & 0 & 0 & s_{ref,Ax}^x & s_{ref,Ax}^y & s_{ref,Ax}^z & 0 & 0 \\ 0 & 1 & 0 & 0 & s_{ref,Ay}^x & 0 & s_{ref,Ay}^y & s_{ref,Ay}^z \\ 0 & 0 & 1 & -s_{ref,Az}^z & 0 & s_{ref,Az}^x & -s_{ref,Az}^y & s_{ref,Az}^y \\ 1 & 0 & 0 & s_{ref,Bx}^x & s_{ref,Bx}^y & s_{ref,Bx}^z & 0 & 0 \\ 0 & 1 & 0 & 0 & s_{ref,By}^x & 0 & s_{ref,By}^y & s_{ref,By}^z \\ 0 & 0 & 1 & -s_{ref,Bz}^z & 0 & s_{ref,Bz}^x & -s_{ref,Bz}^y & s_{ref,Bz}^y \\ 1 & 0 & 0 & s_{ref,Cx}^x & s_{ref,Cx}^y & s_{ref,Cx}^z & 0 & 0 \\ 0 & 1 & 0 & 0 & s_{ref,Cy}^x & 0 & s_{ref,Cy}^y & s_{ref,Cy}^z \\ 0 & 0 & 1 & -s_{ref,Cz}^z & 0 & s_{ref,Cz}^x & -s_{ref,Cz}^y & s_{ref,Cz}^y \\ 1 & 0 & 0 & s_{ref,Dx}^x & s_{ref,Dx}^y & s_{ref,Dx}^z & 0 & 0 \\ 0 & 1 & 0 & 0 & s_{ref,Dy}^x & 0 & s_{ref,Dy}^y & s_{ref,Dy}^z \\ 0 & 0 & 1 & -s_{ref,Dz}^z & 0 & s_{ref,Dz}^x & -s_{ref,Dz}^y & s_{ref,Dz}^y \end{bmatrix}$$

and $s_{ref,Kj}^i$ represents the i^{th} component of the spatial displacement of the j^{th} component of the magnetic field sensor on the K^{th} fluxgate with respect to the reference point. Providing this level of detail in the formulation of the matrix allows for the fact that each fluxgate unit contains three independent sensors located at three slightly different positions.

For this instrument, the origin (apex) of the instrument was chosen as the reference point, and the positions of all the fluxgate sensors were measured with respect to this point.

It is important to acknowledge that both the estimation of the gradient terms via simple signal differencing and by the more generalized techniques described above, assumes the instrument is located within a first-order gradient field. This is generally not the case, and thus both techniques estimate an approximation of the gradient somewhere in the vicinity of the instrument. The precise location where the estimate and the actual gradients match is unknown and is somewhat dependent on the strength of the higher-order gradients produced by the “dipole” source. These higher-order terms are governed analytically by the (unknown) position of the source.

3.3.2. Instrument Imperfections

The wooden frame for the instrument was designed in Autodesk’s Inventor software. The orthogonality of the instrument is provided by angled cuts on the ends of two of the legs and corresponding angled cuts on the piece supporting them. These cuts were made on a bandsaw using a standard 45° jig to define the angle. The pieces were screwed and glued together. Measurements of the orthogonality of the legs of the instrument were made by noting the

positions of the apex and end-points of two legs on a flat surface, then evaluating the deviation from 90° with a large set-square. Deviations between 2-5 mm were measured along a leg length of ~800 mm, resulting in an error on the order of 0.2° - 0.35°.

The individual fluxgate units each contain three, nominally mutually orthogonal fluxgate sensors. The deviance from orthogonality of the 3 fluxgate sensors and fluxgate sensitivity was characterized at the Australian National Magnetic Calibration Facility, run by Geoscience Australia. This information was used to derive a sensitivity error correction matrix that took into account both non-orthogonality between sensors and variations in individual sensor sensitivity (nominally 7 μ T / V).

Finally, while the fluxgates are attached firmly to the instrument frame, they are not necessarily perfectly aligned with the legs (and thus the assumed instrument reference frame). This effectively results in the fluxgates ‘pointing’ in slightly different directions to the instrument’s frame of reference. A calibration technique to rotate all the fluxgates back to a common frame of reference was developed. However at this stage no attempt has been made to calibrate this common frame with respect to the instrument’s physical frame of reference. Fluxgate ‘B’, at the apex of the instrument, was chosen to represent the common reference frame. An estimate of the degree of misalignment between the axis of fluxgate “B” and the leg to which it was attached was determined by placing a straight-edge along the fluxgate and measuring its apparent deviation from the edge of the leg. Over a distance of 30 cm, ~1 mm of deviation was observed, this equates to a misalignment of ~ 0.2°.

The effects of these imperfections have not been modelled but could be included in any future work.

3.4. EM63 Magnetic Dipole Source

For these trials a Geonics EM63, supplied by the US Army Corps of Engineers, was used to generate a rapidly pulsed magnetic field.

As can be seen in Figure 3-3, this cart generates a repetitive magnetic waveform that reverses polarity during one complete cycle.

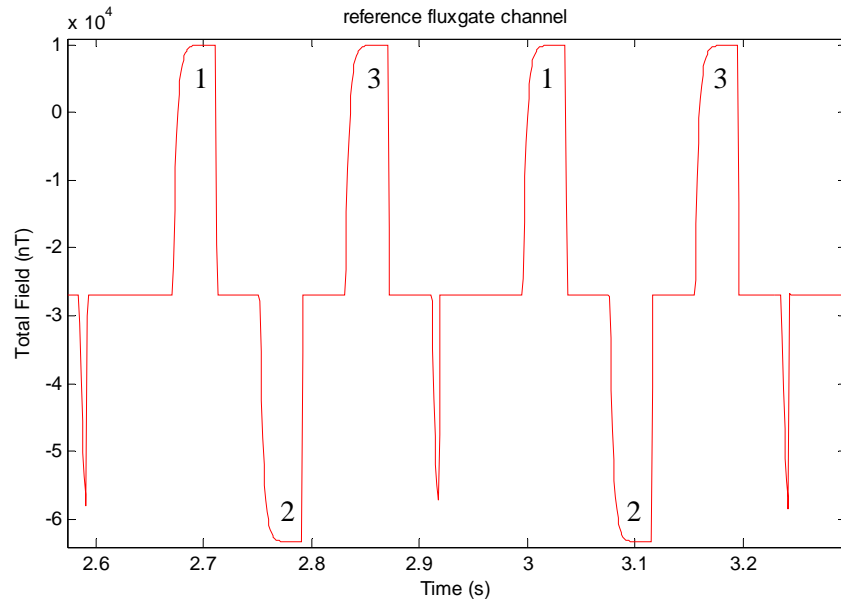


Figure 3-3. Waveform produced by the EM63. This was taken from a fluxgate mounted on the EM63 cart itself. The annotations correspond to the magnitude plots in Figure 3-4 below.

The magnetic moment of the dipole that this pulse generates is quoted as being 1024 Am^2 peak to peak. In practice it was found that:

- The overall peak-to-peak dipole moment magnitude approached a maximum of $\sim 920 \text{ Am}^2$.
- The peak dipole magnitude moment declined over time, presumably due to a dropping battery voltage, initially peaking at $\sim 460 \text{ Am}^2$
- The dipole magnitude moment also varied in the short-term
- Each of the three pulses in each cycle had a different average peak magnitude
- The latter three characteristics are evident in Figure 3-4, which plots the extracted absolute peak magnitude of each pulse over a 70 second (s) sampling period.

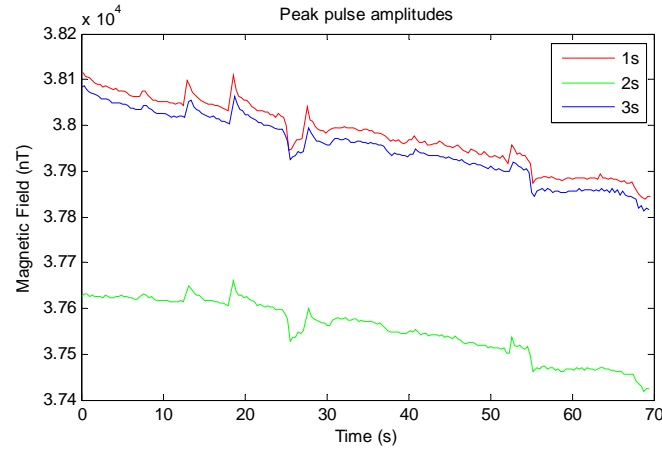


Figure 3-4. Peak pulse amplitude for the three parts of the EM63 transmit cycle, illustrating the general decline, sporadic short-term variation, and the different relative magnitudes of the three parts of the cycle pulses.

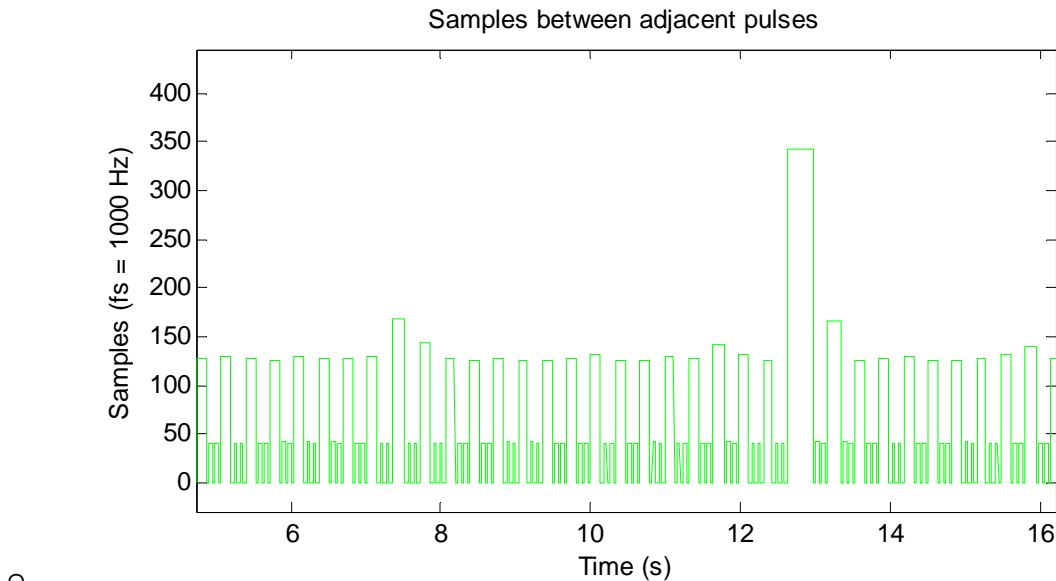


Figure 3-5. Detail of sample counts between recognized pulses.

The exact timing of the EM63 pulse cycles was also examined; a detailed look is shown in Figure 3-5. The short delays between pulses 1 & 2, and 2 & 3, as well as the longer delay between pulses 3 & 1 (or between cycles) are evident. However there is also a longer between-cycle delay occurring regularly, as well as sporadic delays that are more than twice as long. See Figure 3-6 for an example of these long delays.

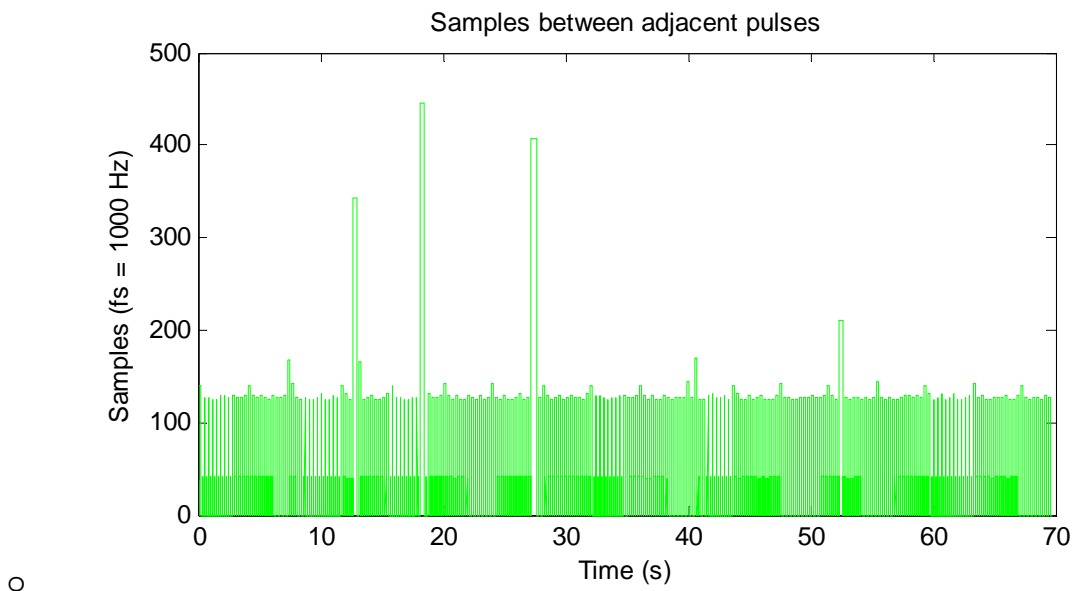


Figure 3-6. Overall delays for a complete run. The random sporadic long-delays are evident.

The transmit signal of the EM63 was monitored with an on-board 3-axis fluxgate, mounted in the centre of the transmit coil. Due to the strong field produced by this coil, the fluxgate axis (y) parallel to the generated field was saturated by the field, and an axis that is nominally normal (x) to the generated field was used to monitor the field. The slight deviation of the x-axis sensor

from a perpendicular orientation ($< 2^\circ$) was still sufficient to generate an applied field of 38 microTeslas (μT) in this fluxgate, a significant proportion of its full scale deflection (70 μT).

This signal provided an unambiguous reference to determine the on-times / off-times of the EM63 – valuable information for extracting the response of the instrument's fluxgate sensors.

3.5. Auxiliary sensors

In addition to the instrument's 4, 3-axis fluxgate sensors, several other sensors were used in the trials.

3.5.1. Tilt-meters

A two-axis tilt-meter (CXTLA02, from Crossbow) was attached to the EM63 above the main axle-line, level with the transmit coil. These two signals provided pitch and roll information from the EM63 during use.

3.5.2. Reference fluxgate

A 3-axis Bartington low-noise fluxgate was attached to the EM63 above the main axle-line, level with the transmit coil. Only the x -axis was sampled, this axis was nominally normal to the applied field, and was aligned with the front-rear axis of the EM63.

3.5.3. SQUID sensor

A CSIRO-built high-temperature (YBCO) SQUID sensor was also used for a short time during the final trial. This sensor is part of a prototype gradiometer developed for a previous geophysical project (Schmidt et al., 2004)

It consists of a single SQUID magnetometer coupled to a tilted axial gradiometer. By rotating the gradiometer through 360° in eight steps, gradient terms from two axes can be deduced. By rotating the entire instrument through 360° in three steps of 120° , the entire gradient tensor can be measured. The instrument and process is shown in Figure 3-7. The gradiometer has a baseline of 50 mm, and the three instrument positions co-locate the SQUID and gradiometer in approximately the same volume. This reduces the effects of any higher order gradient terms on the first-order gradient estimate (compared to the fluxgate instrument).

While this system is not a practical solution for locating the cart, it provides an indication of the performance level that may be achieved with a SQUID-based system.

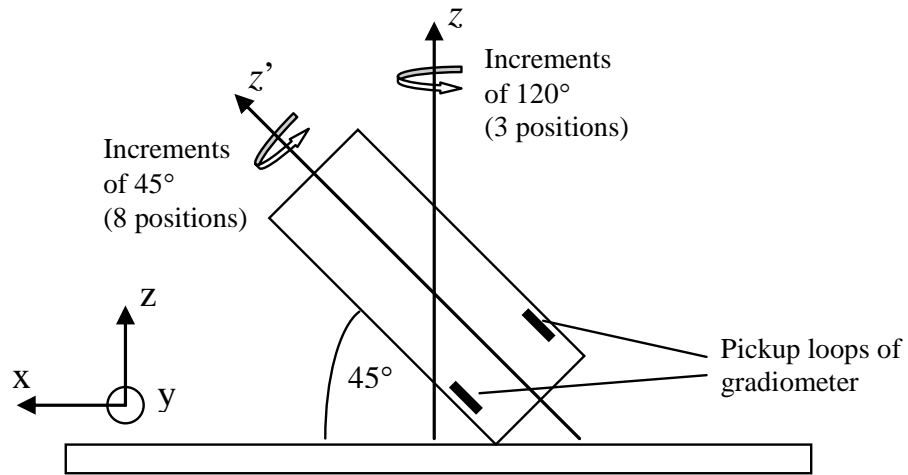


Figure 3-7. Schematic of SQUID gradiometer illustrating general operation.

3.6. Data Acquisition System

A 16 bit, 16-channel National Instruments (NI) PCMCIA acquisition card (DAQCard-6036E) was used to capture the data from all the various sensors used during the trials. This card was plugged into a laptop computer running custom software to monitor, capture and control the acquisition process. An overview of the acquisition and signal path is shown in Figure 3-8.

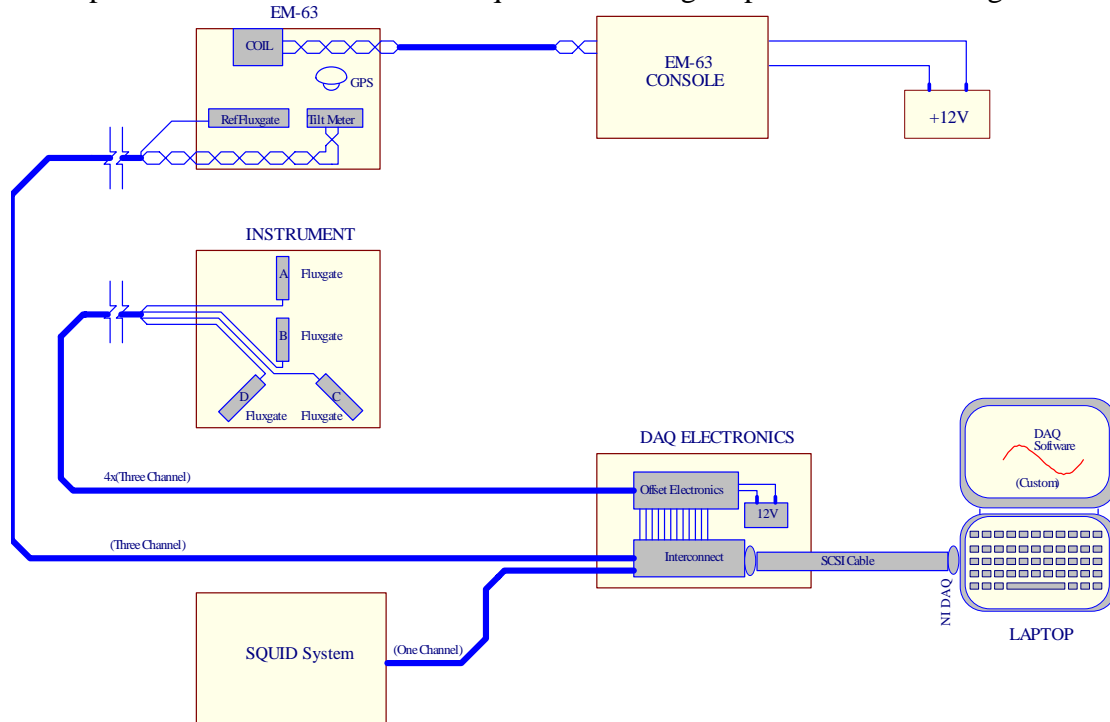


Figure 3-8. Overview of the signal path of the entire system.

Each channel had an individually selectable voltage range of either (+/-) 10 volt (V), 5 V, 500 mV, or 50 mV and the sampling rate was generally held at 1000 Hz on each channel. The NI card samples with a multiplexor, so corresponding samples on each of the channels were not synchronous and actually occurred at different times.

3.6.1. Instrument fluxgate offsets

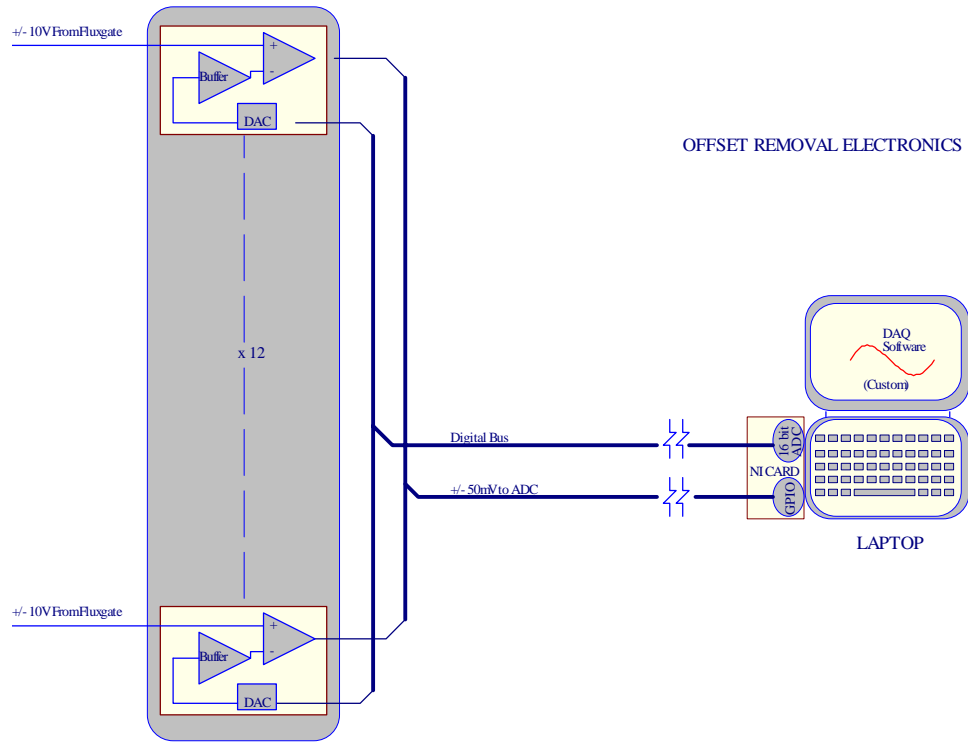


Figure 3-9. Block diagram of the offset removal electronics used in the acquisition system.

Fluxgate sensors are vector field magnetometers, which record the total magnetic field ‘intersected’ by the pick-up area of the sensor. The fluxgates used have a full scale deflection of $\pm 70 \mu\text{T}$ ($\pm 10 \text{ V}$). This means that during outdoor trials, the signal from these fluxgates is dominated by the environmental magnetic field produced by the Earth itself ($\sim 56 \mu\text{T}$). Sampling this full scale signal with a 16-bit ADC gives a quantization step of $\sim 2 \text{ nT}$. This corresponds to a quantization noise spectral density of $333 \text{ pT} / \sqrt{\text{Hz}}$, approximately two orders of magnitude above the noise performance of the fluxgates ($5 \text{ pT} / \sqrt{\text{Hz}}$) and is also greater than the expected size of the signals from the EM63 cart at large distances ($< 1.9 \text{ nT}$ at 30 m).

To overcome this potential problem, CSIRO custom-built electronics to remove a significant proportion of the Earth’s quasi-static field measured by the fluxgates. Figure 3-9 indicates how offset signals generated by digital-to-analogue converters were subtracted from the fluxgate input signals using a differential input operational amplifiers. The resultant signals could then be sampled with the ADC set at a much higher sensitivity (50 mV or 500 mV) thereby reducing the quantization step to either 108 pT or 10.8 pT, and the noise spectral densities to $1 \text{ pT} / \sqrt{\text{Hz}}$ and $10 \text{ fT} / \sqrt{\text{Hz}}$ respectively. The National Instruments datasheet for the DAQCard-6036E implies

noise spectral densities of 1.3 pT / $\sqrt{\text{Hz}}$ and 500 fT / $\sqrt{\text{Hz}}$ respectively, which means the quantization noise is in fact below that of the acquisition system in any case.

During signal sampling, the purpose written data capture software continuously monitored the sampled signals for signs of “clipping”. When detected, the offset DAC voltages were adjusted to move the sampled signals back into the mid-range of their respective ADCs. Prior to use, the full range of offsets produced by the DACs was carefully calibrated using a digital voltmeter. Recording the offset values used during sampling allows the fluxgate signals to be faithfully reproduced during post-processing.

For each trial, the ADC signal gains were pre-selected based on expected signal strength which is a function of the distance between cart and sensor.

3.6.2. Auxiliary sensors

The tilt and reference fluxgate signals could be sampled with sufficient accuracy using a 16 bit ADC. Therefore no offset-removal preconditioning was required for these signals. The final four channels of the NI Data Acquisition System (DAQ) are not offset-compensated.

Note: The SQUID sensor has a much smaller, randomly set offset that is a feature of its operation rather than due to any external signal. Removal of this offset could allow for an increase in the overall ADC sensitivity, however, as shall be shown, ADC sensitivity was not a limiting factor for the SQUID system.

3.6.3. Filtering

Unfortunately there is no anti-aliasing filter on the NI DAQ system.

The offset electronics connecting to the 12 instrument fluxgate channels incorporate an active, 2nd order, low-pass filter with a corner frequency of 880 Hz. This is not ideal, as the sampling rate was only 1000 Hz. Thus it can be expected that more white noise and interference are present in the signal due to aliasing from frequencies above 440 Hz.

The tilt-meters have internal bandwidths of 6 Hz, and the reference fluxgate has such a strong signal that any interference and noise aliasing from these channels is unimportant.

The SQUID system has a filtered bandwidth of 3 kilohertz (kHz). As this signal was sampled at 1000 Hz, the noise bandwidth was aliased / folded-back 6 times, and any consideration of the performance of the SQUID must keep this in mind.

4. Inversion techniques

Two inversion techniques were applied to the gradiometer and magnetometer measurements obtained from the instrument- Wilson's Inversion and Nara's Inversion. A non-linear least squares optimization technique was applied to the magnetometer data directly to refine the Wilson inversion.

4.1. Nara's method

Nara's method (Nara et al., 2006) is a simple linear equation that computes the position vector in the field of an ideal dipole using a single-point measurement of magnetic vector field, and its gradient tensor at that position. The advantage of Nara's method is that it provides an exact solution for the position. This compares favourably to the Wilson inversion, which provides a set of four ambiguous scaled solutions.

However, Nara's method requires the additional measurement of a B-field component, which may be more easily contaminated by external interference. Additionally, there is a 3x3 matrix inversion in the formula, which may introduce extreme variability into the solution due to the noise present in the gradient tensor estimate.

4.2. Wilson's method

Wilson's method (Wilson, 1985) computes the eigenvalues of the gradient tensor and generates a set of four possible solutions for the scaled magnetic moment and scaled position vector. With a priori knowledge of the dipole moment and its approximate orientation, the scaled quantities can be converted to actual measurements, and three out of the four computed solutions can be trivially discarded.

4.3. LSQ Optimization

The two methods discussed above are drawn from an ideal single-point measurement of the magnetic field or gradient field. Our instrument combines the output of 12 separate sensors to compute approximations to both of these quantities. These first-order approximations result in inaccuracy in the resulting inversions. However, these inversions can be used to estimate the position and dipole moment of the cart, and further optimization techniques can be applied by considering the original sensor measurements.

In this case, good a priori knowledge of the relative spatial locations of all four, 3-axis magnetometer measurements exists, and LSQ optimization can be made on the position vector and moment vector to fit these 12 independent measurements to the ideal dipole field.

By assuming the first-order inversion places the position and orientation of the dipole in a local minima of the solution space, MATLAB's LSQ optimization routines can fine-tune these parameters to within the ultimate sensor / environmental noise limitations.

MATLAB's LSQ optimization uses the dipole equation to generate a numerical approximation to the local gradient in the free parameters of the solution space, based on the summed power of the errors in the current estimated position.

5. Model

To develop an understanding of the performance that may be possible with the instrument in the field, and to provide a comparison for the eventual data that was gathered, a theoretical model of the instrument was developed in MATLAB. The inversion algorithms to process the modeled data were also implemented in MATLAB.

This model assisted in the development of the transformation matrices required to rotate fields measured in the instrument reference frame to a more useful global reference frame (as described in §3.2).

Developing this model involved constructing a relatively closely-matched geometric description of the instrument, applying the analytical description of the magnetic field due to a dipole to this geometry, adding representative levels of noise corresponding to the sensor of interest and thus generating a set of modeled signals that the instrument would be expected to generate due to these fields.

At that point, the different inversion techniques could be trialed on the simulated signals. This allowed comparison with idealized (single point gradient) signals to evaluate how the instrument geometry affected the performance of the inversions. Later it enabled evaluations of real sensor data by matching the model's parameters to that of the experimental runs and generating comparative data.

5.1. Limitations and assumptions of the model

The model makes the following assumptions about the geometry and characteristics of the instrument / system:

- The 3-axis vector magnetometers (fluxgates) are all aligned exactly with the instrument reference frame.
- The instrument reference frame is perfectly orthogonal.
- The 3-axis magnetometers make their 3-axis measurements at a single point
- The baselines for each pair (BA, BC, BD) of 3-axis magnetometers is identical and exact (0.60 m)
- The baselines are perfectly parallel with the instrument frame axes.
- The model evaluates the field produced by a perfect dipole source at each sensor in the absence of any other fields.
- The model does not consider the impact of any limitations of the measurement extraction techniques.
- The model considers additive white Gaussian noise (AWGN) in a fixed bandwidth with no other interference sources.
- This differs from the actual system in the corresponding ways:

- Can only use a coil-set calibration to correct for misalignment of the 3-axis fluxgates from the instrument reference frame.
- The instrument reference frame is limited by the wooden construction tolerances.
- The 3-axis fluxgates have three separate sensors, one for each axis, spaced 15 mm apart.
- The baselines for each pair of fluxgates vary and are in error due to measurement tolerances / sensor dimension.
- The baselines are off-axis and non-parallel to the instrument frame axes.
- The EM63 source is only approximated as a magnetic dipole, and this approximation becomes less valid in close proximity to the EM63.
- Soil type was not characterized and no attempt has been made to for compensate for conductance or susceptibility related effects.
- The instrument sensors require signal processing techniques to extract the field components from a pulsed magnetic source signal that varies in strength and involves timing estimation and averaging to produce results.
- The sensors of the instrument do not necessarily exhibit a flat noise profile, and there is considerable interference from the 50 Hz alternating current (AC) power systems, as well as low-frequency interference in the background fields (1/f noise.)

6. Calibration

The instrument was calibrated in a 2.5 x 2.5 x 2.5 m 3-axis ‘Rubens coil set’ (Rubens, 1945). This coil set resembles a cage with five coil windings per axis, and can be used to generate a very uniform field within a volume in the centre of the ‘Rubens Cage’.

By applying 3 orthogonal uniform fields to the instrument, the orientations of the 3-axis sensors within each fluxgate can be determined with respect to each other. By further assuming one of the fluxgates (‘B’ in this case) is aligned perfectly with the instrument’s axes, rotation of the magnetic field vector measurements from the other three fluxgates to this common reference frame can take place and the gradient can be determined. Furthermore, the gradient tensor, and all four vector measurements can be transformed to the more convenient ‘world’ reference frame, which is defined by the known geometry of the instrument frame and used in the inversion algorithms to determine the location of the dipole producing the vector field.

Errors with this calibration approach include the assumption of a known, ideal alignment between the instrument frame and the B fluxgate, the assumed perfect orthogonality and known geometry of the instrument frame, and the assumed perfect orthogonality of the coil set.

7. CSIRO Trial

A number of trials took place with the system, both in the lab and in the field. Each trial leading up to the final trial helped to develop the acquisition system and experimental techniques to improve the interpretation of the results.

The final trial was comprehensive, and forms the entire basis for the results presented in this report. For this final trial, the chosen test site was a nearby sports field (Fiddens Wharf oval). Compared to many sites located close to the CSIRO's Lindfield laboratory, this site has reduced interference from passing vehicles and power lines.

7.1. Setup

The purpose of this study was to provide an indication of the feasibility of using a magnetic gradiometer / magnetometer based instrument to detect, locate and track the position of an UXO detection cart, for distances varying between 1 and 50 metres. Figure 7-1 is an overview of the field trial setup.

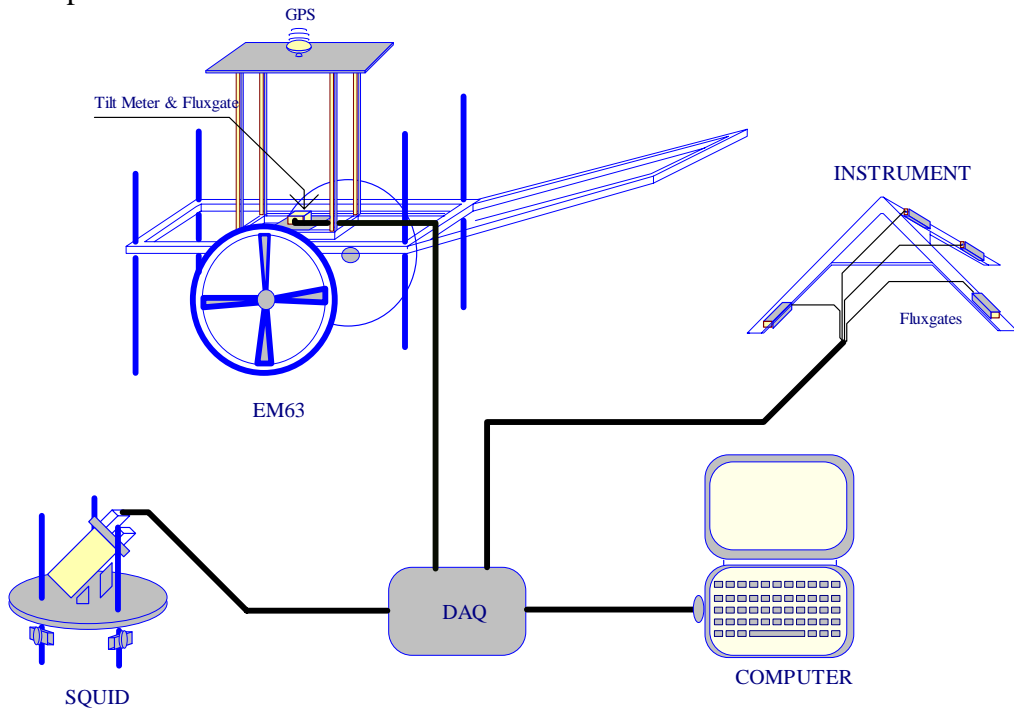


Figure 7-1. Overview of the system setup for the field trial.

For our field trials, we put together the sensor and acquisition system described earlier, and attempted to locate the position of the EM63 provided to us. The EM63 cart was augmented with a 2-axis tilt sensor, a 3-axis fluxgate (both mounted in the middle of the transmit coil), and a GPS receiver (mounted approximately 70 cm above the transmit coil). A plumb-bob was attached under the cart to provide a mechanism for referencing to cart to a position marker (a golf-tee).

Additionally, a SQUID-based gradiometer instrument was also setup to record the gradient field for a single position, to provide a comparison with a more sensitive sensor.

Ultimately what is required from the trial is an understanding of exactly where the EM63 was with respect to the instrument, and how this compares to the computed position using measurements and appropriate inversion techniques.

7.1.1. Trial geometry

Two approaches were combined in tandem to provide reliable positioning information for the EM63 during the trial:

- Tape-measured distances using a convenient local reference
- Real-time kinematics (RTK) enabled GPS receivers mounted on the EM63 and a separate surveying pole.

The field where the trial took place was marked with a soccer field layout, Figure 7-2. By utilizing the right-angle between the goal square and the playing field markings, positions were measured out in the layout shown below, typically with 1 m separation between adjacent positions. Care was taken to ensure line widths did not affect the accuracy of the measurements across the area, and it was generally believed that < 5 cm accuracy was achieved using a surveyors tape measure.

The GPS receivers were Magellan ProMark 500 units, reportedly capable of achieving ~ 1 mm (rms) accuracy with post-processed kinematic algorithms. One was attached to the EM63 cart, and a second was used as a local base station. At the conclusion of the trial, a 2 m surveyor's mast was used to survey all the marked positions used during the trial. Ultimately this final set of GPS measurements was used as a basis for considering the effectiveness of the instrument, as they were performed by a trained operator using a spirit level, whereas the GPS on the cart was possibly rotated away from the true position due to (varying) the tilt of the cart when stationary.

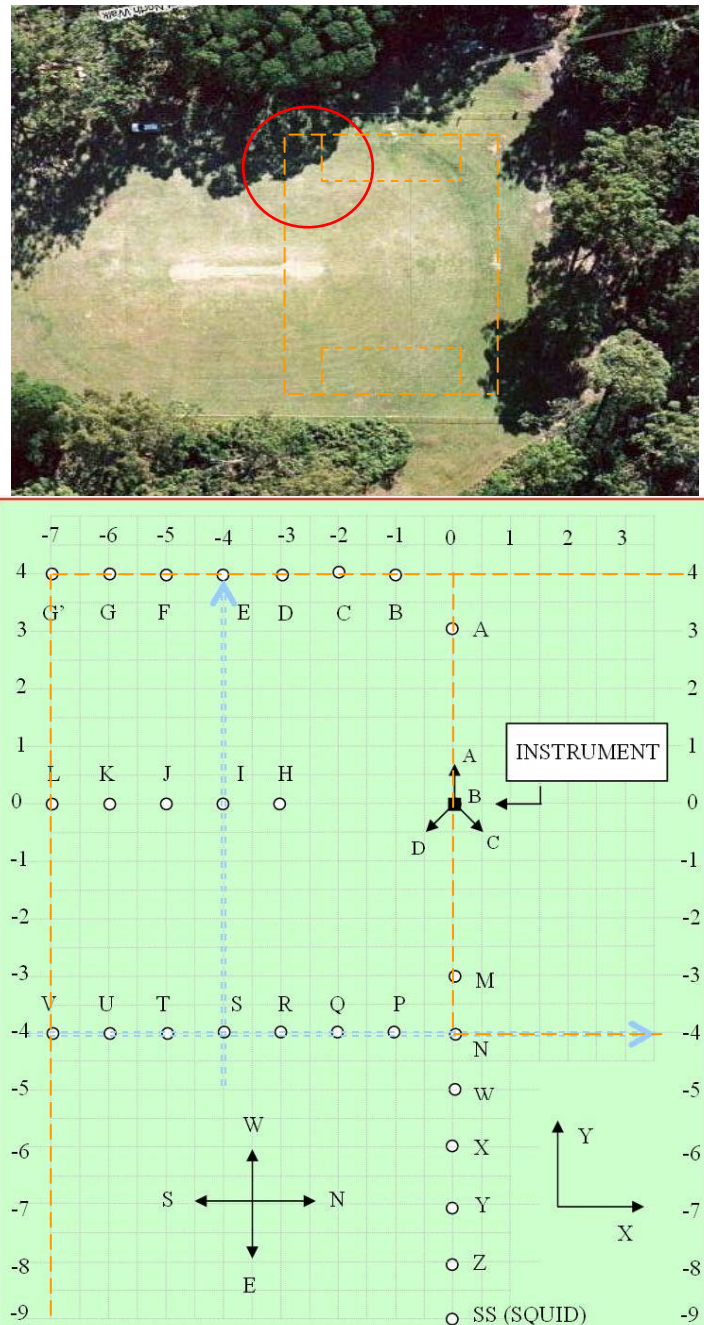


Figure 7-2. Layout of the experiment. The centre of the instrument was actually 160 mm further West than indicated due to the location of the plumb-bob. The photo is from Google Maps.

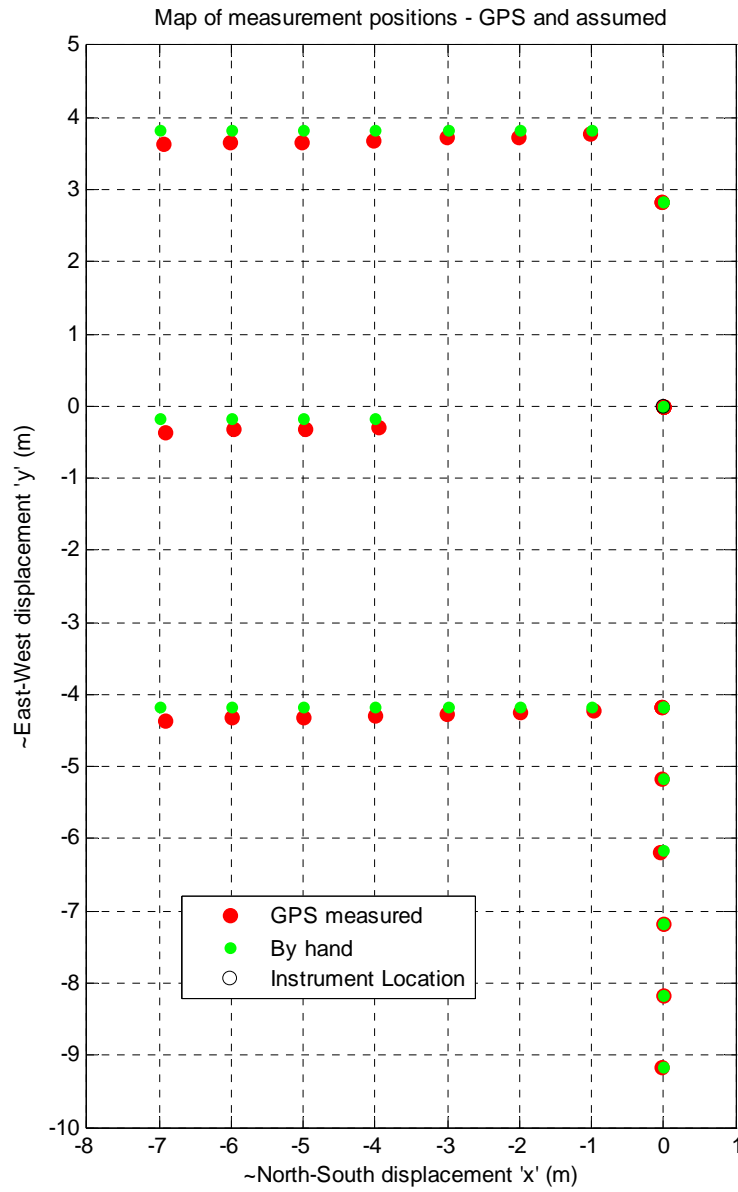


Figure 7-3. Plot of the different cart positions, comparing hand-measured and GPS measured.

The GPS measurements were rotated to align the line extending between position A and position SS with the vertical axis of the local reference frame (on which A and SS both lie). From this operation, it is evident in Figure 7-3 that the soccer field markings were not quite square, as the GPS measurements diverge linearly from the hand-measured positions towards the left (South) of the field.

7.1.2. Extraction of fluxgate measurements

The use of a reference fluxgate on the EM63 sampled quasi-synchronously with the 12 sensors on the instrument provided a convenient method to extract the start and end points of the transmit pulses generated by the EM63. The strength of the signal at this reference sensor was such that only relatively simple logic was necessary to identify the sharp rising and falling edges of the

transmit pulse. Using a reference sensor was necessary, as the EM63 system did not have a reliably constant pulse repetition rate, and the effort required to develop pulse detection code for use with much lower signal to noise ratio (SNR) present on the instrument sensors was too great for the resources available for this project.

To estimate the peak magnitude of the response of a sensor to a given transmit pulse, a 20 sample average was taken of the waveform from 22 samples before the falling edge of the pulse, and a second 20 sample average was taken 40 samples after the start of the first (or 18 samples after the falling edge). These periods correspond to the part of the transmit pulse that is relatively flat, and the off-time respectively. The difference between these two was used as the estimate of the peak magnitude of the pulse. A graphical representation of this process is illustrated as a finite impulse response discrete filter in Figure 7-4.

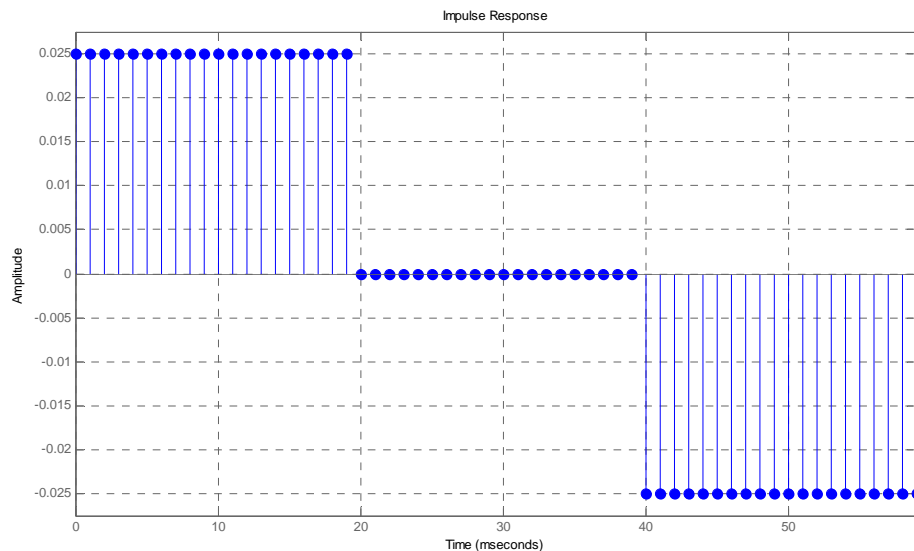


Figure 7-4. Impulse response of the measurement extraction technique / filter. The central portion of this response (where zero weighting is applied to the signal) covers the falling edge transition of the transmit pulse, which occurs usually around the 21-22 ms mark. Thus this filter describes the result of taking a 20 sample average of the pulse peak, and subtracting from that average a 20 sample average of the off-time.

This technique was chosen due to the fact that, at a sampling rate of 1000 Hz, a 20 sample average corresponds to one cycle of the ever-present 50 Hz magnetic interference from nearby mains power systems. Thus two 20-sample averages taken from two identical points in the 50 Hz waveform should cancel out the majority of this interference. That said, the timing of the acquisition system may drift from 1000 Hz and/or the mains interference may drift from 50 Hz, so that the filter “nulls” will not match the mains interference signal and thus some residual interference signal can be expected. The frequency response of the Finite Impulse Response (FIR) filter is shown in Figure 7-5.

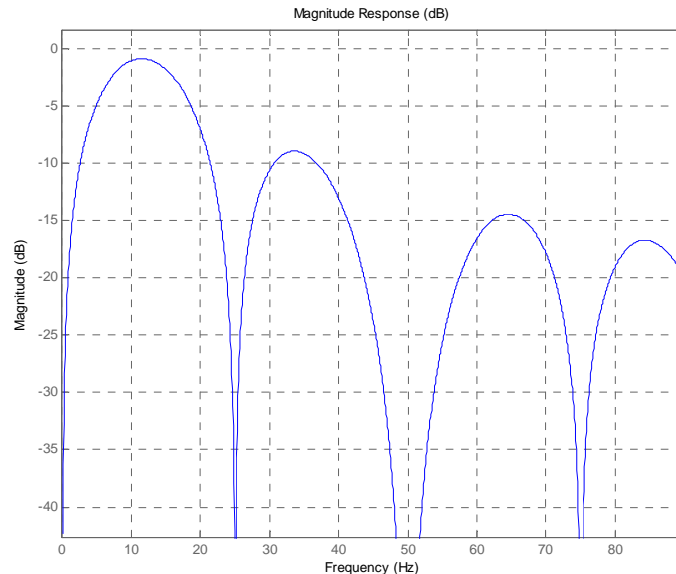


Figure 7-5. Frequency response of the extraction filter. Good cancellation of any 50 Hz interference is evident, as well as a good rejection of very low frequency noise. The bandwidth of this response is approximately 12 Hz, centred at 11.5 Hz.

Twelve channels of a 16-channel ADC were used to sample the gradiometer's fluxgate sensors, another two channels of the ADC were used to sample a tilt-meter and one channel was used to sample the signal from a 3-axis fluxgate mounted on the cart itself. The NI 16-channel acquisition system is not a true synchronous system – it multiplexes its ADC and thus samples each channel sequentially. When combining averages from different sensors to form gradiometers, the timing error / jitter between averages has not been taken into account. Given that the maximum jitter between samples averaged over 20 ms is 1 ms, the effect of timing mismatch is believed to be minor and has not been evaluated in any detail at this stage. Sample jitter was considered important when selecting the data to be averaged to generate estimates of the pulse peaks. To avoid including the Tx fall time, all sampling ended 2 samples before the end of the transmit pulse.

7.2. SQUID measurements

A SQUID gradiometer sensor was trialed briefly to provide some comparison with the fluxgate based gradiometer. The unused, 16th channel, of the NI ADC was used to sample the SQUID gradiometer's signal.

SQUID system measurements were averaged in an identical fashion to that of the fluxgates. Timing information from the reference channel was used to select the data to be averaged to generate pulse peak estimates.

In the case of the SQUID system, the gradient is built up from a series of 24 measurements taken with different rotations of the gradiometer and instrument (Schmidt et al., 2004). Three 'runs' were made for a single cart position with the SQUID system; one for each orientation of the SQUID instrument. Within each run, the gradiometer was left in each of its 8 positions for approximately 10 seconds to provide a suitable set of measurements for statistical information to

be derived. This process is evident in Figure 7-6. These periods of measurements are interrupted by SQUID resets during the rotation. Periods when the gradiometer was functioning correctly were identified, extracted from the overall record and averaged to generate a single voltage level for each of the 24 positions. A spreadsheet (developed as part of an earlier project) was used to transform these voltages into a gradient tensor, and this was fed into the Wilson inversion algorithm to determine position.

Standard deviation information was also taken from the 10 second periods, and used to estimate (with appropriate scaling factors) the gradient measurement variability of the SQUID system.

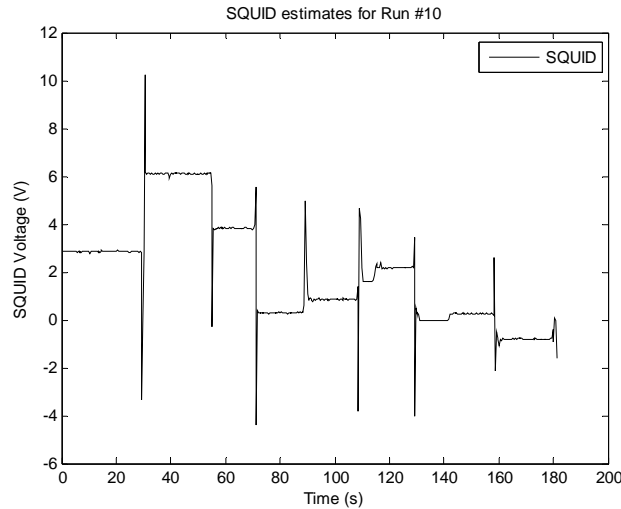


Figure 7-6. Extracted SQUID signal for Run #10, eight different sustained voltage levels can be identified (with resets in between).

7.2.1. Repeat of SQUID measurements

In the main field trial, the SQUID system was setup as indicated (at position SS –Figure 7-2) and three separate sets of measurements were taken. However, the conditions for monitoring these signals was not ideal, and it was discovered during post-processing that the SQUID signal had come out of lock and returned a clipped ± 10 V signal for large portions of the measurements.

Thus the SQUID measurements were repeated on a separate day. A single set of measurements were taken with the SQUID system approximately 5.2 m in front of the EM63 cart. No GPS system was available for positioning, and thus only a surveyor's tape-measure was used. Furthermore there are no clear reference marks on the SQUID system indicating its centre-line or orientation, as it was never designed for such precise positioning work.

Thus in evaluating the gradient tensor and accuracy of the inverse, as the orientation of the SQUID with respect to the cart was not accurately known, only the magnitude of the resulting position vector could be evaluated with any certainty.

For comparison with the fluxgate instrument, the standard deviation (spread) of the SQUID gradiometer's gradient estimates is of most interest.

7.3. Measurement bandwidth and rate

The EM63 produces ~ 3 pulse sequences per second, with each sequence consisting of three 40 ms transmit pulses (see Figure 3-3). Thus the maximum measurement rate possible is approximately 9 measurements per second.

However each measurement consists of the difference between two 20 sample averages, sampled at 1000 Hz. This corresponds to an approximately 12 Hz measurement bandwidth centred at 11.5 Hz when considering the impact of noise, as illustrated in Figure 7-5.

For the purposes of analysis, only one pulse out of every sequence was considered. This is because, as shown in Figure 3-4, each pulse varies in magnitude, and even with compensation (see §7.4), this introduces artifacts and clustering into the results. It is also easier to draw first order statistics from a dataset consisting of only one of the three pulses.

7.4. The magnetic moment of the EM63

As noted in §3.4, the peak amplitude of the pulse generated by the EM63 is neither constant across the three pulses in each group, nor constant over time. There is a short-term variability in the strength of the pulse as well as a long-term decline in the peak magnitude, presumably due to a decaying voltage on the lead-acid batteries powering the EM63 system. This variation was estimated as a mean, standard deviation and percentage standard deviation for each run. Generally it was found that the standard deviation in the pulse amplitude for any given pulse train amounted to less than 1% (typically 0.1%) of the absolute value. Over the course of the trial, however, the peak magnitude degraded by $\sim 15\%$.

For the Wilson inversion in particular, knowledge of the value of the magnetic moment representing the field produced by the EM63 primary coil is required to produce absolute position and orientation information. This moment is further used as a constraint on the LSQ optimization process.

An estimate of the dipole moment was made from two individual runs with the EM63 stationary, using the average values of the magnetometers during each run. This moment was divided by the corresponding average magnitude measured on the reference fluxgate channel to produce a scaling term. This scaling term was used to estimate the magnetic moment present for each pulse in all the data runs from the reference fluxgate measurement.

It would appear from these estimates, see Table 7-1, that the magnetic moment of the EM63 varies (trends down) as the sensor is moved away from the source. This indicates that the EM63 is not an ideal dipole, and that higher order components of the field exist closer to the source.

Table 7-1. Positions, fields and estimated dipole moment from fluxgates at two positions at two times during the field trial.

Run #3		Final Position			Field		Estimated
	(A)	X	Y	Z	Y	Z	Moment
	A	0	2.3616	-0.3565	1022.92	3352.51	-489.45
	B	0	2.7984	-0.0476	275.71	2078.33	-456.05
	C	-0.4	3.045	-0.3703	-289.73	1494.91	-462.00
	D	0.43	3.0646	-0.3929	-296.45	1484.87	-473.26

Run #29		Final Position			Field		Estimated
	(N)	X	Y	Z	Y	Z	Moment
	A	0	-4.6354	-0.3565	92.74	408.9	-418
	B	0	-4.1986	-0.0476	9.11	569.11	-421
	C	-0.4	-3.952	-0.3703	169.84	650.72	-424
	D	0.43	-3.9324	-0.3929	188.14	656.54	-425

7.5. Modeling of EM63 source

A model of the field produced by the EM63 was achieved using the Biot-Savart law and the known geometry of the cart. The component of the field, based on this model, was calculated at several positions in line with the vertical axis of the cart and compared to measurements from a brief experiment. For each position, the theoretical dipole moment was calculated based on the component and the distance from the centre of the EM63 coil. As is clear in Figure 7-7, the fitted dipole moment matches the same profile for both the modelled and measured field values, with the exception of the closest measurement. This indicates both that the EM63 is certainly not ideally modelled as a point-source dipole, but that it appears possible to create a more accurate model based on the Biot-Savart law.

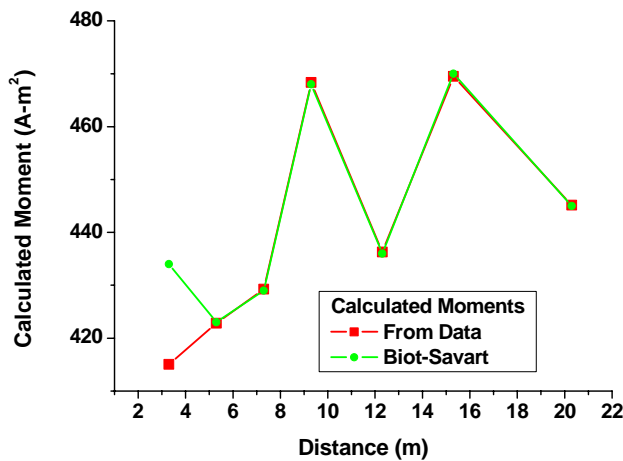


Figure 7-7. Calculated moments from on-axis measurements of the field produced by the EM63, compared with theoretical predictions using the Biot-Savart law.

No attempt in this study was made to incorporate the Biot-Savart law into the inversion / optimization routines, but it would be an important avenue of further work.

7.6. Presentation of results

Ultimately, it is the real-world positioning performance that is of interest in this study. This is presented both graphically, and as the deviation of the average of all the estimates for each run from the measured position – the accuracy, and as the variability of each single estimate of the position – the standard deviation. For reference, the modeled instrument results are presented as a single graphical figure. This model was configured with similar characteristics to the actual experiment programmed in, such as standard deviation of the field measurements (integrated as AWGN), baseline of the instrument, and assumed / measured position of the source. Specific modeled results are shown for a single run, where pertinent.

A few runs were selected to demonstrate some of the results, and a full suite of results is listed in Appendix A. For each run, a plot of the assumed location, GPS measured location, Wilson inversion and LSQ optimized inversion is shown, with the inversion data shown as a scatter plot of a series of measurements from the instrument.

7.7. Sensor measurement statistics

It is important to evaluate the raw performance of the fluxgate sensors in the field, with and without a source of excitation.

7.7.1. No source

To estimate the performance of the fluxgates without a source, a run (#1) of data was taken with the EM63 source turned off. Figure 7-8 shows the x -component of the A fluxgate. The blue trace is the raw data, with the direct current (DC) component removed, during this 40 second run. A

large disturbance is visible towards the end of the series, possibly due to a scientist moving near the instrument. The red trace indicates the output of the fluxgate after applying the same extraction technique to that which is used to evaluate the fluxgate measurements of the pulses. That is, two 20 sample sequences are averaged and subtracted from one another to form a new signal.

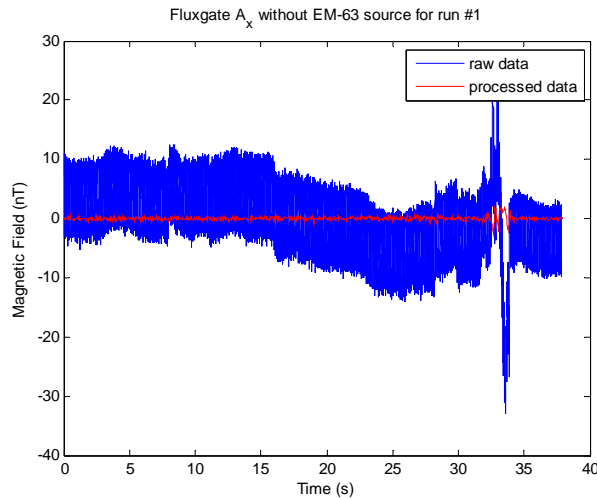


Figure 7-8. Run #1, the x-axis of the A fluxgate with the EM63 deactivated. The blue trace is the raw data with the DC offset removed; the red is the processed data-stream.

The standard deviation was calculated for both of these sequences for the first 15 seconds of the data. This indicates the best performance that might be expected from the later source-driven measurements.

Raw fluxgate standard deviation: **3.3 nT** (at 1000 Hz)

Processed fluxgate standard deviation: **0.29 nT** (at 25 Hz)

The raw standard deviation corresponds closely to the standard deviation of a modelled fluxgate data with white noise power of $100 \text{ pT} / \sqrt{\text{Hz}}$, a factor of 20 greater than the specified noise power of these sensors and above the quantization noise of the ADC.

The processed standard deviation corresponds closely to a fluxgate with noise power of $50 \text{ pT} / \sqrt{\text{Hz}}$, which is still 10 times greater than that specified.

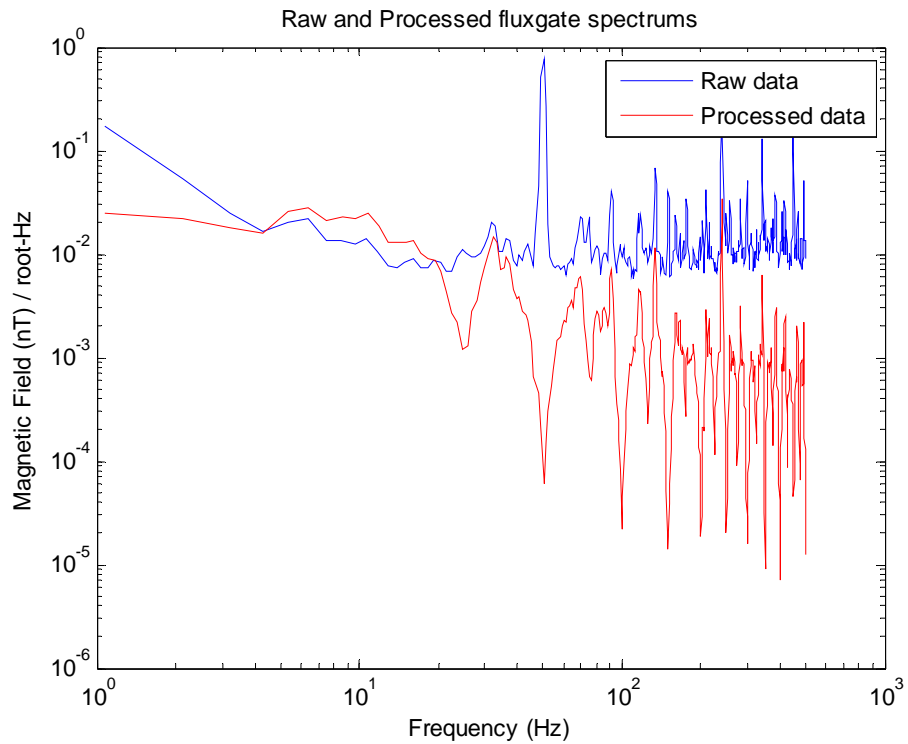


Figure 7-9. This plots the raw and processed noise / interference spectra of the A fluxgate during Run #1, with the EM63 deactivated. Note the low frequency (1/f) ramp and 50 Hz spike in the blue plot, which has been successfully attenuated in the processed signal.

The noise spectrum of the raw fluxgate data (with DC removed) is shown in Figure 7-9. This graph indicates that the noise floor of the fluxgate sits around $6-10 \text{ pT} / \sqrt{\text{Hz}}$, which is close to the manufacturer's specification ($5 \text{ pT} / \sqrt{\text{Hz}}$), but that the fluxgate suffers from significant interference at 50 Hz, as well as some low-frequency noise (drift).

The raw gradiometer performance was also examined in a similar way, with the axis signals of the A and B fluxgates subtracted from one another and divided by their baseline to form a gradient signal. This signal was also subsequently processed to produce an averaged / differenced signal. The raw / processed signals, as well as the spectrum of the raw signal are shown in Figure 7-10.

The standard deviation of these gradiometer signals was also evaluated:

Raw Fluxgate gradiometer standard deviation: **20 nT / m** (at 1000 Hz)

Processed Fluxgate gradiometer standard deviation: **0.71 nT / m** (at 25 Hz)

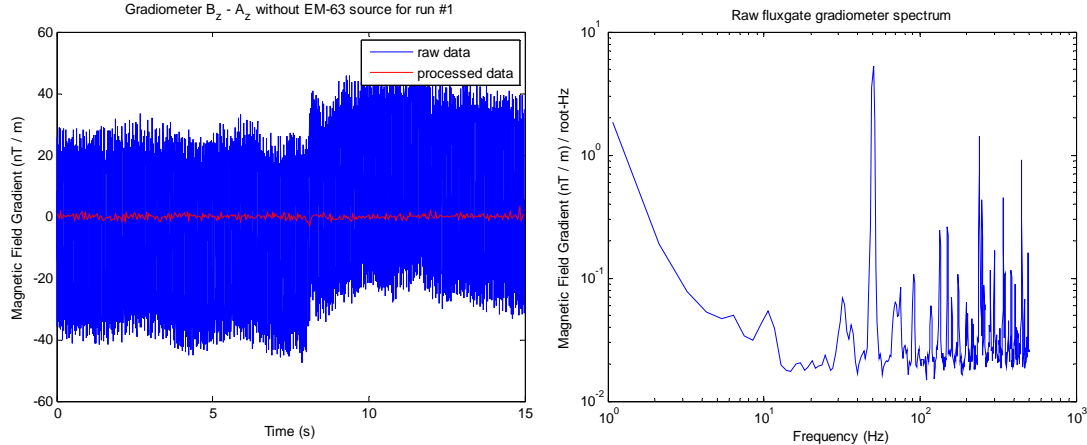


Figure 7-10. Raw gradient signal for one of the gradiometer baselines on the fluxgates. It's associated spectrum is shown on the right.

The raw spectrum illustrates remaining low-frequency noise and 50 Hz components. The extraction process is applied to the magnetometer signal, before forming the gradient tensor, so this spectrum is not necessarily representative of the final gradient measurement noise.

The extraction technique is implicitly a filter, as described in §7.1.2, with a frequency response characterized as a band-pass filter at 11.5 Hz with a bandwidth of 12 Hz. The effect on the raw signal in the frequency domain is illustrated in Figure 7-9.

7.7.2. With source

With the EM63 turned on, the estimated fluxgate measurements for each transmit pulse is calculated and then 2 in 3 are discarded to accommodate the variation between pulse magnitudes (as seen in §3.4). This series of estimates is then evaluated for a mean and standard deviation.

Figure 7-11 demonstrates some low-frequency change in the estimates over the course of a run. The cause of this is unknown, but may relate to the 50 Hz interference or long-term cyclical jitter in the timing / estimation code.

Generally the standard deviation of the fluxgate estimates was between 0.7 and 1.0 nT (Figure 7-12), which matches closely to the simulated statistics from above. Any further variation may have more to do with the nature of the source than the fluxgate itself.

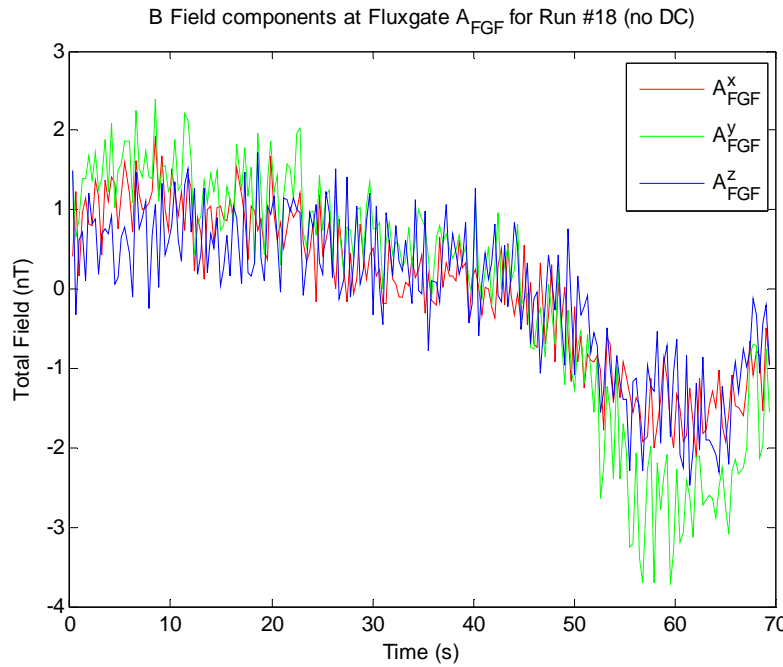


Figure 7-11. Illustration of the slow variability of the estimated / extracted peak amplitude of the measured pulse.

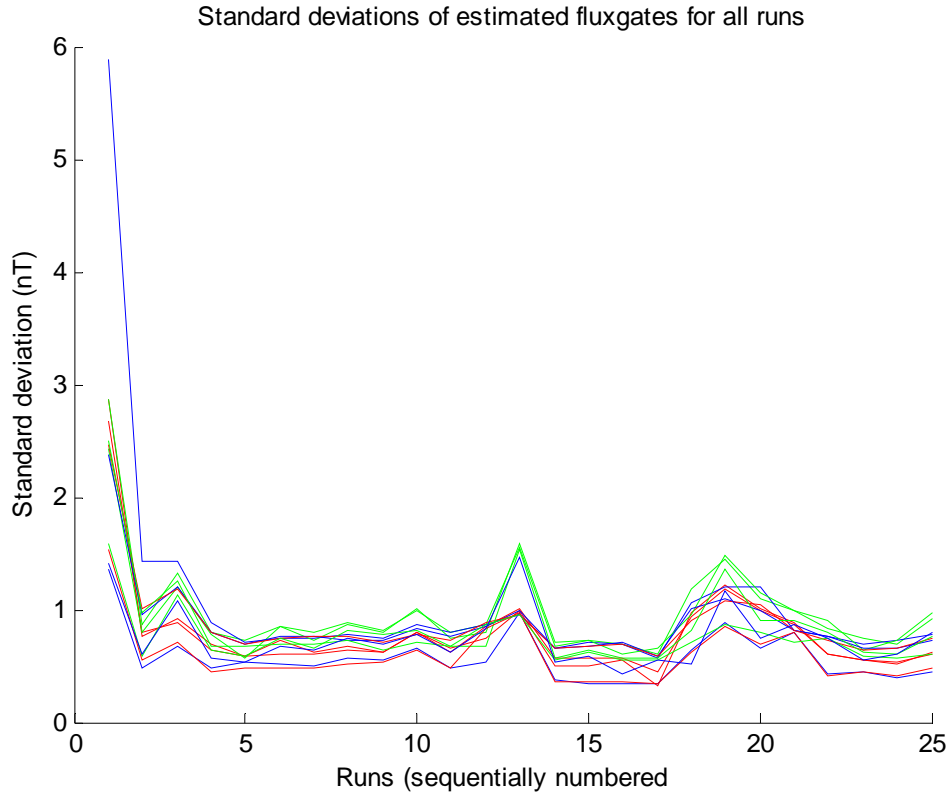


Figure 7-12. Standard deviations of all 12 fluxgate sensors for all runs from the field trial. Generally they range between 0.5 and 0.8 nT, with a few outliers.

7.7.3. SQUID measurement statistics

The SQUID signal, in terms of its sensitivity to the magnetic field is depicted in Figure 7-13. This illustrates less low-frequency drift, as the SQUID is intrinsically a gradiometer in that instrument.

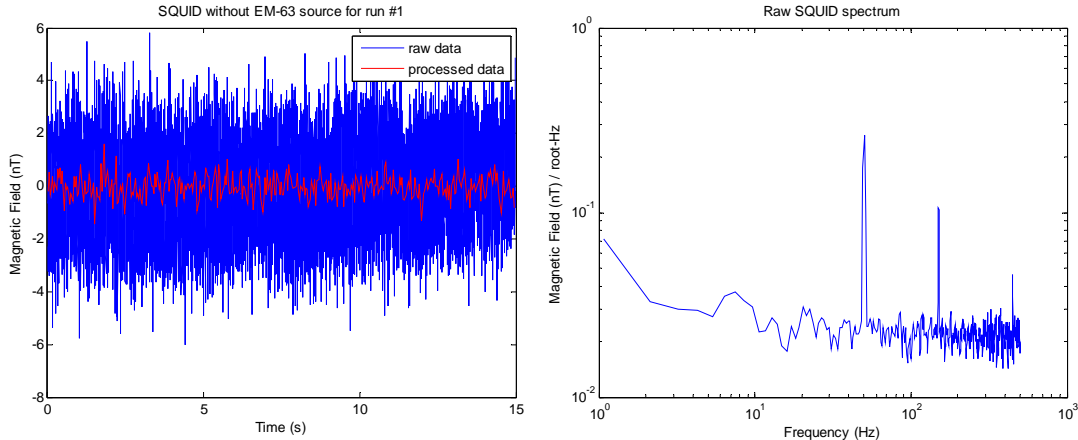


Figure 7-13. The raw / processed SQUID signals, and raw spectrum, without the EM63 source.

However the processed data from the SQUID signal does show more variability than the fluxgate sensor, the standard deviations are:

Raw SQUID standard deviation: **1.6 nT** (at 1000 Hz)

Processed SQUID standard deviation: **0.43 nT** (at 25 Hz)

However, sensitivity to the magnetic field is not the primary design goal of this instrument, and it is therefore important to consider the variability of its appropriately scaled gradiometer version of the signal. The spectrum of this signal is shown in Figure 7-14.

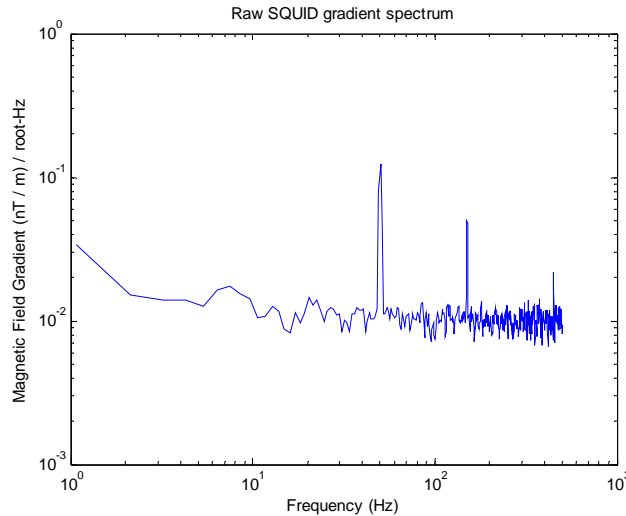


Figure 7-14. Spectrum of the raw SQUID gradiometer signal.

In this spectrum, again the low-frequency drift is less evident than in the fluxgate case. The standard deviations of the raw / processed SQUID gradiometer signals are:

Raw SQUID gradiometer standard deviation: **0.74 / m** (at 1000 Hz)

Processed SQUID gradiometer standard deviation: **0.20 nT / m** (at 25 Hz)

This result indicates that the existing SQUID-based gradiometer may be up to a minimum of three times better at estimating the gradient than a fluxgate based instrument. It is important to note that this SQUID gradiometer has the potential for even greater sensitivity. On the day in question, it was biased using a d.c. current. Results from the GETMAG trials (Schmidt et al., 2004), show that an order of magnitude improvement in noise performance is possible by both heating the SQUID after moving and using a.c. bias reversal.

For the one trial undertaken, while the EM63 was transmitting, the raw SQUID signal's standard deviation did not match the noise estimates above; typically the standard deviations were ~ 1.5 nT / m. This appears twice as bad as the fluxgate gradiometer noise. The reasons for this are unclear at this stage, but may be related to measurement extraction artifacts.

7.8. SQUID Results

As mentioned before, the SQUID data was not taken from a well-defined reference frame / position, having been positioned about 5.29 m from the EM63 and oriented approximately by eye.

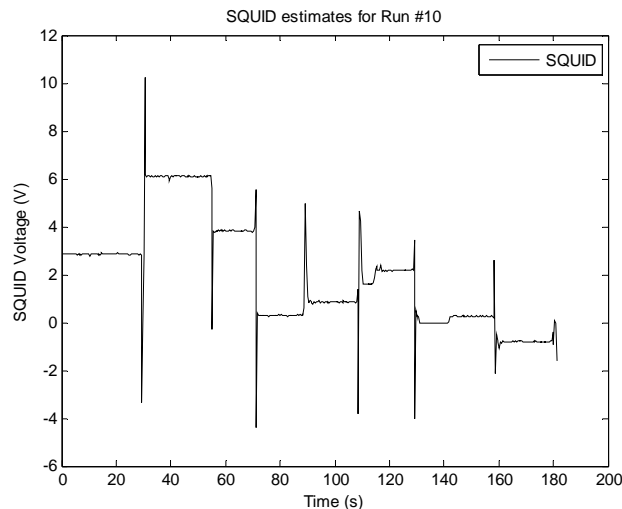


Figure 7-15. Extracted SQUID signal for Run #10, eight different sustained voltage levels can be identified (with resets in between).

The extracted gradient tensor is given below, in nT / m.

22.61	-6.13	-184.34
-6.13	-4.99	-26.97
-184.34	-26.97	-17.62

Using an estimated magnetic moment of 460 Am^2 for the EM63, the Wilson inversion algorithm placed the cart at [5.13, 0.71, -0.10] m from the SQUID instrument. The distance this represents is 5.19 m, relatively close to the actual position of the cart.

As SQUID sensors offer the advantage of shorter baselines and enhanced sensitivity compared to the fluxgate-based system trialed in this feasibility study, further work is required to ascertain if these potential benefits can be realized.

7.9. Nara's method results

The Nara inversion method worked to provide a rough estimate of the position of the cart. However it was not very accurate when compared to the Wilson inversion. This is due to the nature of the method, as it involves a matrix inversion, which in many cases introduces a large variability into the solution. The condition number was generally relatively well-behaved for most of the runs up to about 6 m (Figure 7-17), which might indicate it was simply the effect the noisy measurements had on the inversion, rather than the condition of the tensor itself. An example of the output is provided in Figure 7-16.

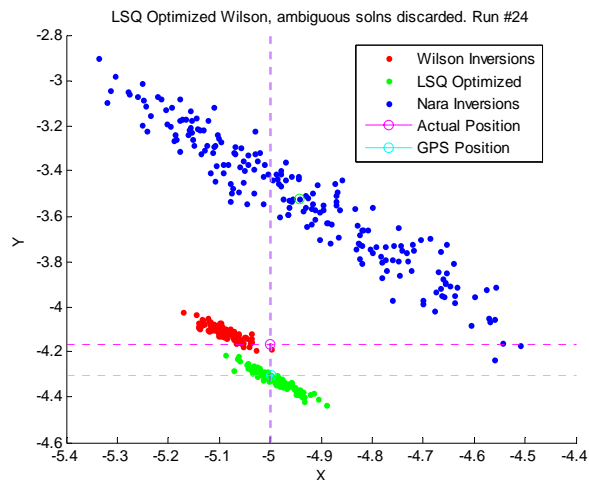


Figure 7-16. Illustration of the Nara inversions. They are generally less accurate and suffer from a greater spread than the Wilson and Wilson+LSQ inversions.

Some indication of the performance of the Nara inversion across all the runs is shown in Appendix A section 3, wide variability is indicated with the standard deviation bars, and the general inaccuracy is evident.

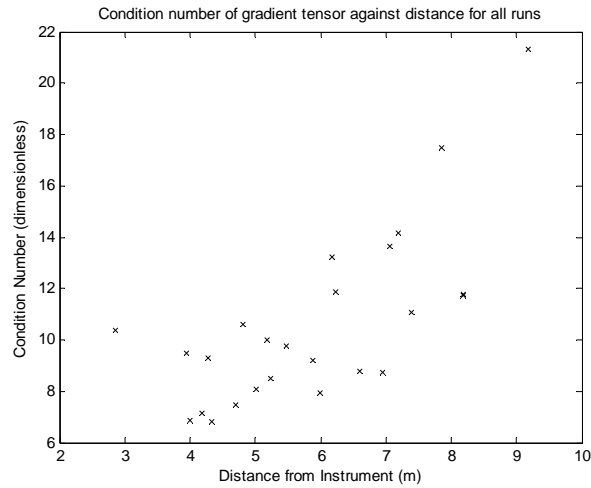


Figure 7-17. Average condition number of the gradient tensor against distance for each run.

7.10. Wilson inversion

All the Wilson and LSQ inversions are contained in Appendix A which includes a large map summarizing all the inversions as well as individual detail plots.

Generally, the Wilson inversion worked well to locate the dipole, with the 3 ambiguous solutions easily rejected for all of the measurements in the trial (Figure 7-18).

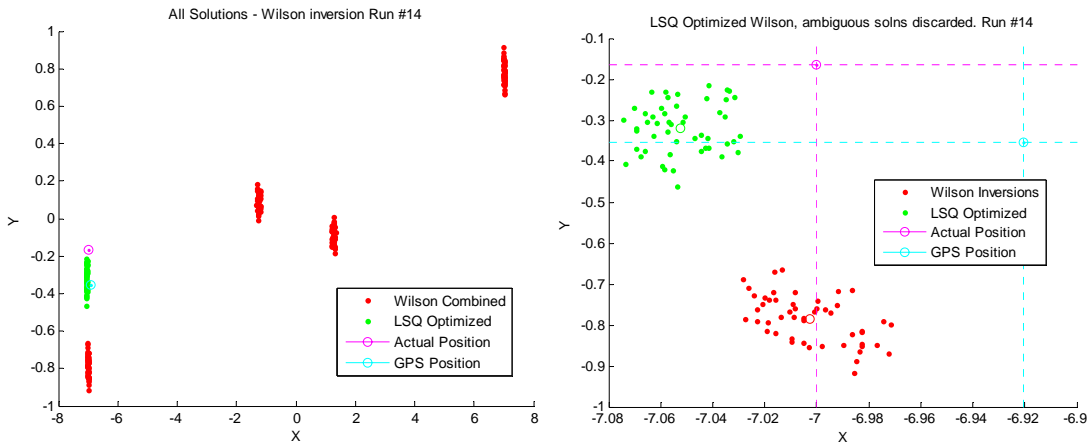


Figure 7-18. Two plots of run #14 illustrating the ambiguous solutions (left), and the automatic rejection working (right). (Note: the scales of each axis are not the same.)

There was a clear accuracy error, mirrored in the modelled data, when using the Wilson method (§10). This is attributed to the assumption of a quasi-static gradient field near the instrument. That is, the gradient is assumed to be the same at all sensors (spread over three 60 cm baselines in three dimensions) in calculating a single gradient tensor for the inversion. This is not the case, primarily due to the presence of higher order gradient terms in the ideal dipole equation, and secondly due to the EM63 not being an ideal dipole source.

Conceptually, the estimated gradient tensor only exists at a single point in the gradient field of the dipole, and this estimated gradient would reasonably occur in or near the instrument itself, but not necessarily at the origin of the instrument. Thus with an instrument with baselines of 60 cm subtending a three dimensional space, it might be reasonable to assume the true location of the estimated gradient could lie anywhere within this volume, immediately bringing up an error on the order of the baseline in the corresponding Wilson inversion. Indeed this seems to be the case in some of the runs.

7.11. Wilson inversion with LSQ

When the LSQ optimization was applied to the Wilson solution, an improved estimate of the cart position emerges. This is due to the optimization fitting the individual magnetometer measurements with the ideal dipole field. In this case there is still a quasi-static assumption in place, but it concerns the uniformity of the magnetic vector field around each individual fluxgate device. In this case there are three orthogonal vector sensors located within 15 mm of one another, so the assumption that the B field is constant over this space is somewhat less of a problem (given the desired performance characteristics of the instrument).

The modeled data indicates that the LSQ optimized Wilson inversions should converge on the true position of the cart.

7.12. Accuracy and spread in Wilson inversions

Accuracy refers to the expected value of the solution compared to the real position of the cart. In the case of these experiments, the expected value is the mean value of possibly several hundred measurements of the cart's position whilst it is stationary.

Spread, or standard deviation, refers to the variation between single measurements of the position of the cart whilst it is stationary.

7.12.1. Standard deviation – Spread

For each position, the standard deviation of the set of Wilson and LSQ inversions was calculated. This indicates the spread of the solution, and represents the positioning error for a single pulse measurement. It is not an indication of the accuracy of the solution (that is, whether many of them would converge on the true position).

Figure 7-19 compares runs 42 and 14. In these two runs, the EM63 was at an 'edge' of the field. The cyan lines indicate the standard deviation of the x and y components of the inversion solutions. It is clear from these graphs that the spread of the solutions is not symmetric in both dimensions, and that the component parallel to the direction from the EM63 to the instrument has a smaller spread than the other component. That is, the solutions are more precise in the distance dimension than the angular / tangential dimension.

For example in run 42 (left), the dipole is directly 'below' the instrument (from a plan-view) at $\sim[0, -9.16]$, thus the radial direction is parallel to the y-axis and the y-component has a much

smaller standard deviation than the x -component. The opposite is true for run 14 (right), where the EM63 is to the left of the instrument. This asymmetry is evident in both the Wilson inversion, and the LSQ optimized solutions.

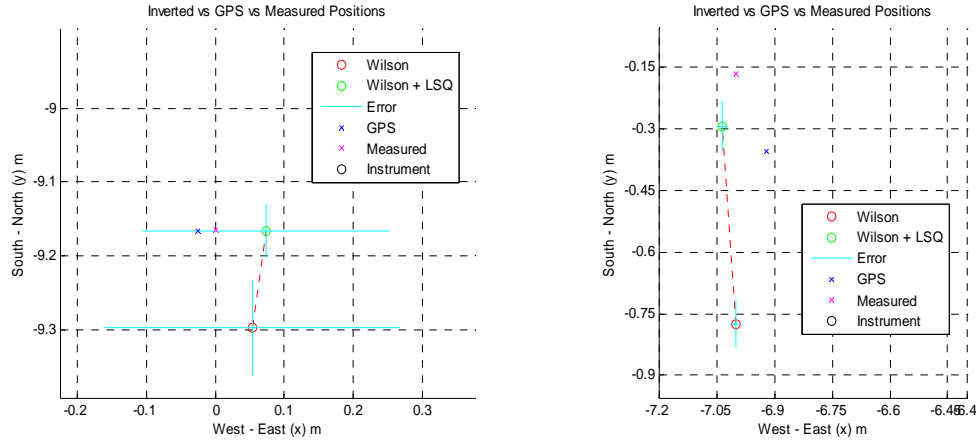


Figure 7-19. Runs 42 (left) and 14 (right) illustrating the non-symmetric spread (cyan bars) in the components of the solutions, depending on the position of the source.

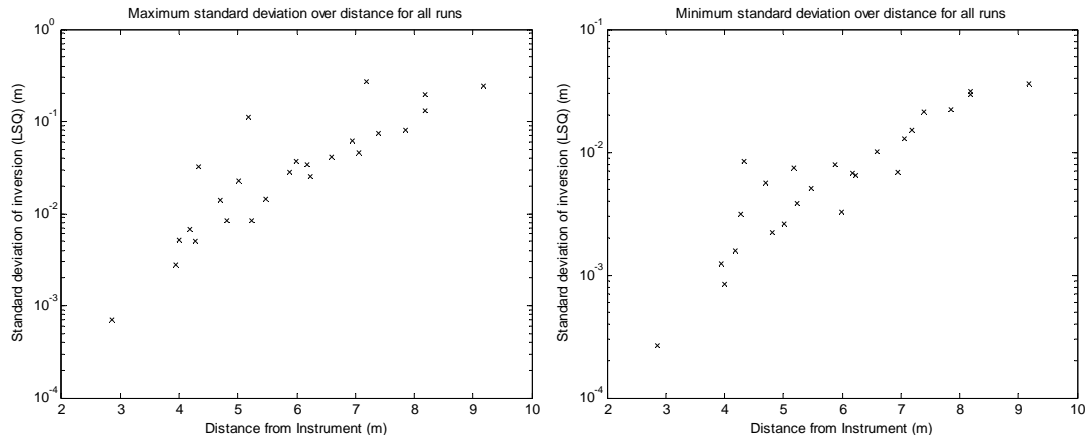


Figure 7-20. These two graphs plot the maximum or minimum standard deviation found (out of all three components of the solution) in all the runs, against the known distance of the EM63 from the instrument.

Figure 7-20 plots the best and worst case spreads against the distance of the EM63 for all the runs made in the field trial.

7.12.2. Accuracy – expected value

The Wilson and Nara methods show significant, reproducible inaccuracy. These inaccuracies are predictable (from the model of the system) and thus fairly well understood to be a result of the failure of the quasi-static gradient assumption (§7.10).

The Wilson technique optimized with the LSQ algorithm improves the accuracy of the Wilson technique significantly. There is predicted to be no deviation between the true position and the expected value position of the LSQ optimized results, according to the model. However, whilst many positions did indeed come remarkably close to this prediction, there were occasionally

significant remaining inaccuracies (of up to 150 mm). The reasons for these inconsistencies are unknown, however it is suspected that deviations in the EM63 source from the ideal dipole model, especially in close, are one significant reason. Other possibilities are ground half-space effects, bias in the field estimation techniques, or geometry calibration issues (especially at the larger distances).

7.13. Comparisons between data and model

The relative position of the EM63 and the instrument were recorded with a high-performance GPS system. These positions were input into the MATLAB model of the instrument along with the noise power required to generate the standard deviations typically found in the measured data. Then plots similar to those from the real data were generated from the model for comparison.

Generally, the model and data agreed with each other, especially regarding the position of the standard Wilson inversion solution. This is particularly evident when considering the two overall summary plots in §2 and §3. The positional error of the red circle (indicating the Wilson inversion solution) correlates strongly between both sets of data. The main difference in the modelled case is the reliable convergence of the LSQ optimized solution to the GPS position, whereas the real data suggest inaccuracies of up to 200 mm are possible.

While the noise in the model was chosen to reproduce the standard deviation of the fluxgate measurements, the error in the inverted positions in the model appear somewhat larger than those in the data. This would suggest that the measurements in the data are drifting due to a low frequency drift or cyclic 50 Hz effects, resulting in a non-Gaussian distribution and larger statistical standard deviation.

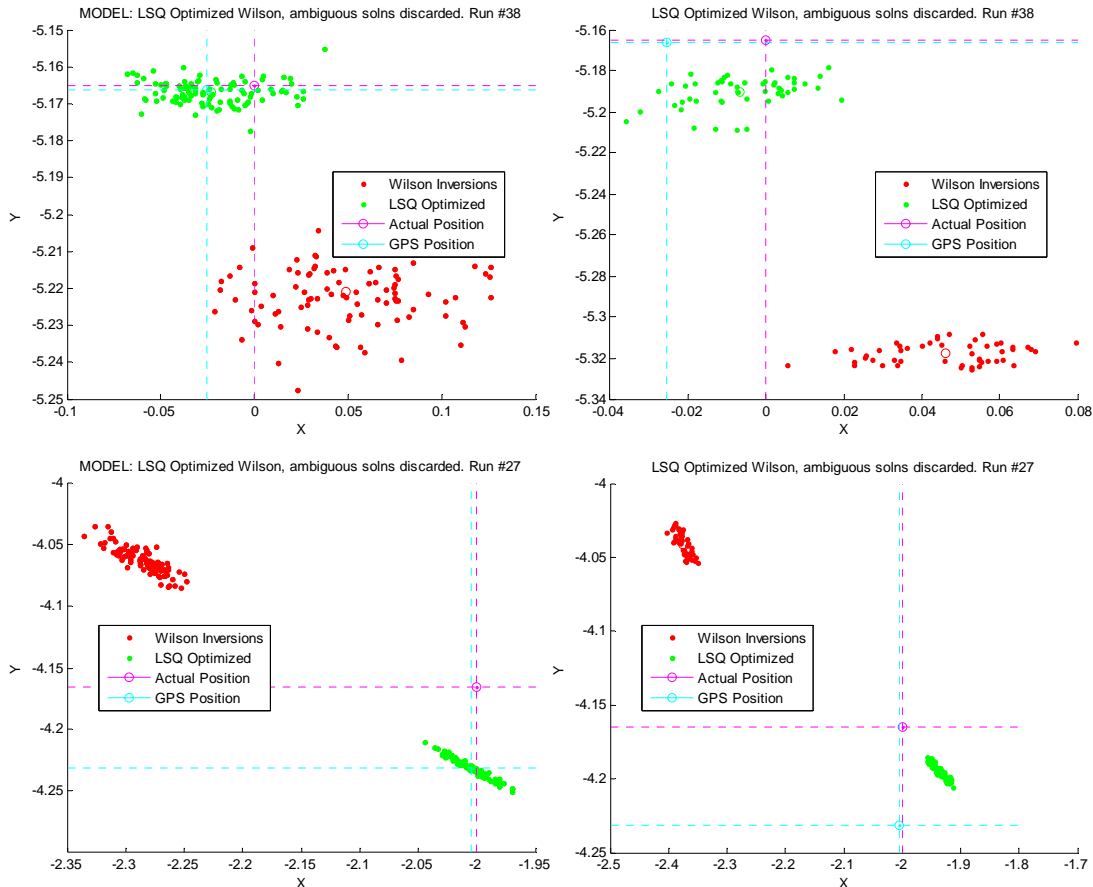


Figure 7-21. Two examples of the model correlating closely with the data. Modelled geometry on the left, actual data on the right.

7.14. Motion results

Two runs were made with the EM63 cart in motion. For each run the operator was asked to walk the cart in a straight line across two or more reference points on the field at about 0.5 m / s. Even though the GPS system was operating during this time, the plots below only show the straight line between the reference marks. Thus any deviation from this line may actually be due to wobble in the operator's path during the walk. The characteristic inaccuracy of the pure Wilson inversion is evident (red plot), while the LSQ optimized solutions converge quite well on the path taken. See Figure 7-22 and Figure 7-23 for details.

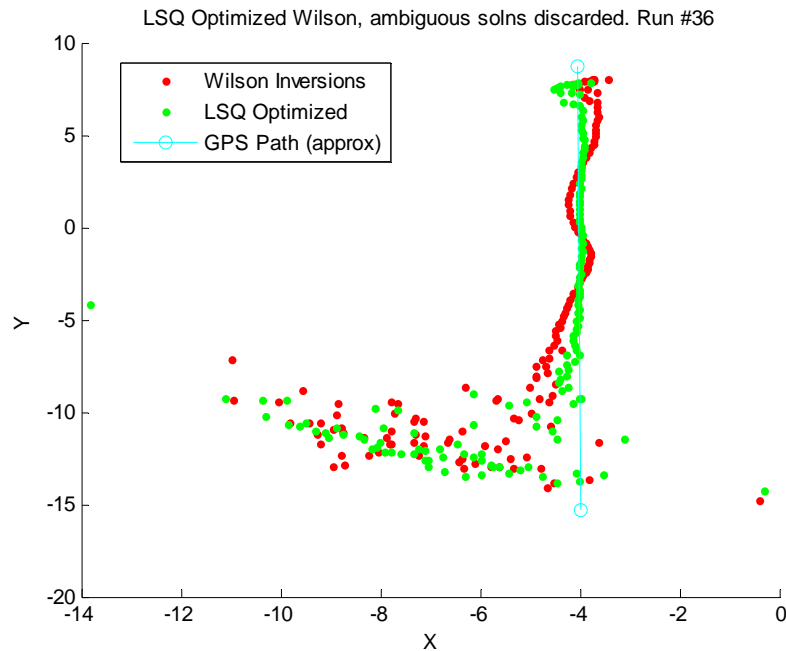


Figure 7-22. Run #36. Cart was walked West across reference marks S-I-E. The cyan line is an extrapolation between points S and E, as measured by the GPS system.

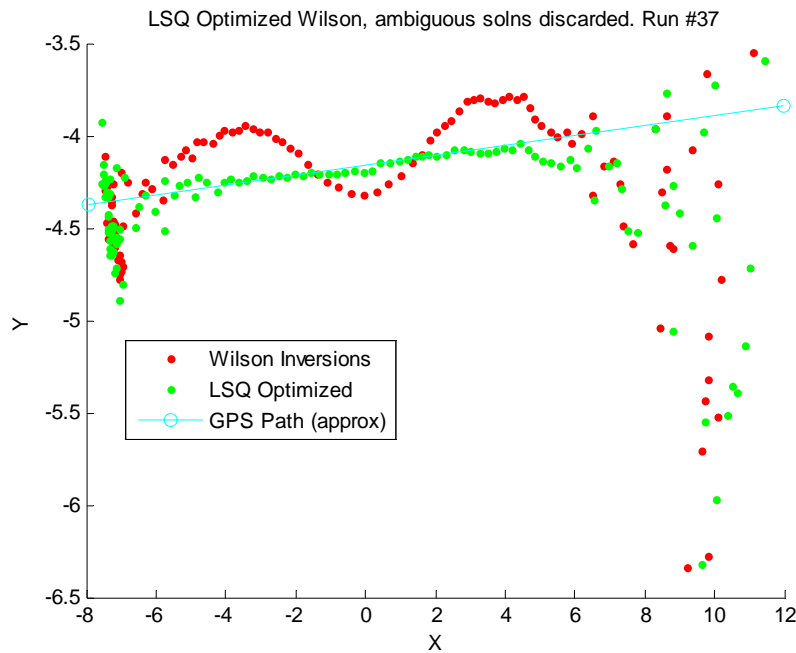


Figure 7-23. Run #37. Cart was walked North across reference marks V and N. The cyan line is an extrapolation between points V and N, as measured by the GPS system.

7.15. Tilt Results

A single run was made with the cart stationary at position S (-4, -4), but being tilted forward and backwards (pitch) by the operator. The Wilson inversion routine was modified to choose the correct solution based on the approximately known position (as opposed to the known moment in other runs) – as assumptions about the direction of the moment could not be made accurately due to the severe tilts induced in the cart.

The tilt angle was calculated from the orientation of the LSQ optimized solution for the moment, and compared to the tilt-meter signals present on the EM63.

Figure 7-24 compares the two measurements of the tilt. There is a broad agreement in the shapes of the two signals in the pitch direction, but they differ in magnitude. There is some uncertainty which measurement is correct, as observers of the action estimated a tilt of approximately 20° in each direction at the time.

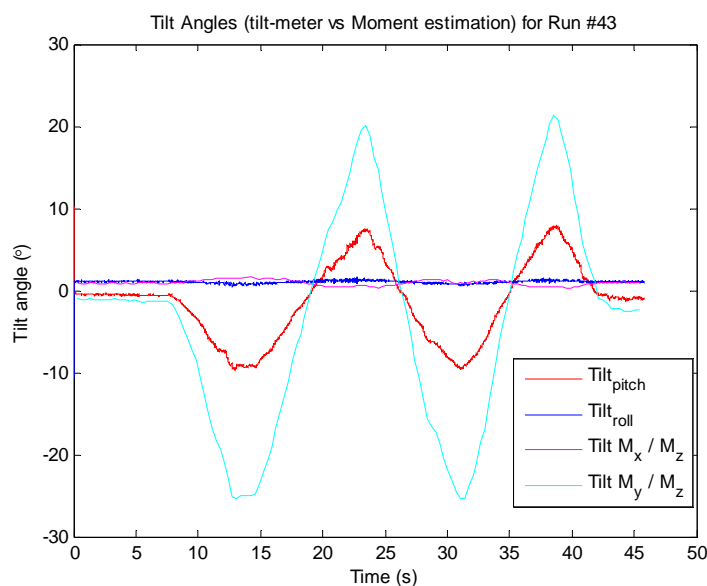


Figure 7-24. Tilt-meter vs calculated tilt from moment. While the shapes agree, the magnitude of the tilts do not.

If the tilt-meter signal is scaled to match the approximate magnitude of the calculated tilt from the field measurements (Figure 7-25), broad agreement is evident. This suggests that it is possible some scaling problem occurred with the tilt-meter sensor, either in software or during the acquisition phase.

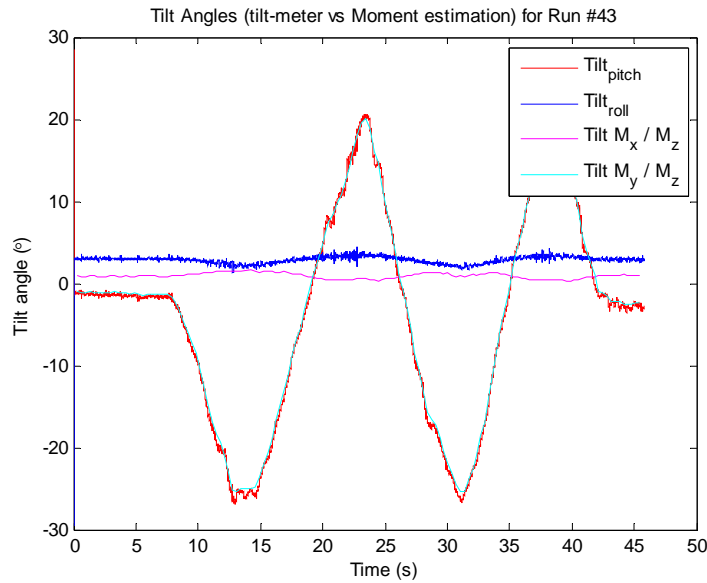


Figure 7-25. Tilt-meter signal scaled to match calculated tilt.

8. Effect of secondary fields on localization

8.1. Concept

One issue that we have neglected up to this point is the influence of the conductivity and susceptibility of the ground on the localization accuracy. We are also interested in determining whether there is an advantage of B-field (fluxgates, SQUIDS) versus dB/dt (coils) sensors for transmitter localization, due to their different responses to conductivity and susceptibility. For the calculations, we model the transmitter as a vertically oriented magnetic dipole and assume that the ground is represented by a half-space with uniform conductivity and susceptibility. We could model any vector component of the B- or dB/dt field at any arbitrary height, but for simplicities sake assume the transmitter and receiver are at the same height above the half space and consider only the z-component of the field. We use the transmitter waveform of the EM63 (Figure 8-1), which comprises an exponentially increasing ramp-up (time-constant 4.3 ms), followed by a rapid linear ramp-off (0.1 ms). The B-field of the primary field will be a maximum towards the end of the ramp-up, and we assume that the B-field is monitored from 25 to 33 ms after pulse turn-on. The dB/dt field will be a maximum during the linear ramp-down, and we assume that the dB/dt field will be monitored from 0.05 to 0.1 ms after the start of the ramp-down.

Within North America soil conductivity generally lies in the range of 0.5 to 30 mS/m (FCC, 2009). As far as we are aware there is no comprehensive database of soil susceptibility within the United States. Van Dam and Velbel (2009) show measurements over a wide-range of soils (most with basaltic parent material) which indicates that susceptibility ranges from 10^{-6} SI to 0.1 SI. The larger susceptibilities were generally encountered at Hawaiian sites. Within the continental USA, susceptibility values generally fell within the range of 0.0001 to 0.01 SI. Due to the bias towards basaltic parent materials, these values probably lie within the high-range of what would typically be encountered.

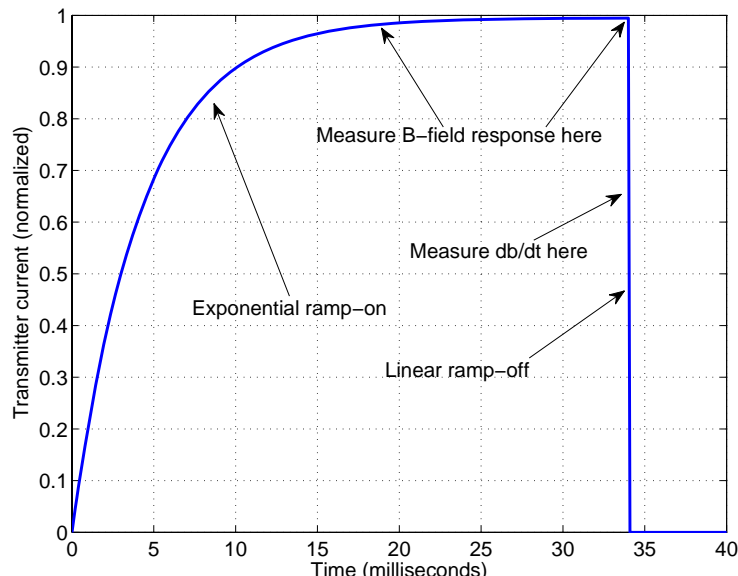


Figure 8-1. Transmitter waveform for the EM63 showing where B-field and dB/dt measurements would be made.

8.2. B-field response from a conductive/susceptible half-space

According to Ward and Hohmann (1987), for a sinusoidal primary field of angular frequency ω , the magnetic field Hz at a measurement point $\mathbf{x}=(x,y,z)$ due to a directed magnetic dipole source located at $(0,0,h)$ over a half-space is,

$$H_z(\mathbf{x}, \omega, \sigma, \chi) = \frac{1}{4\pi} \int_0^{\infty} \left(e^{-\lambda|z+h|} + \frac{\lambda + \lambda\chi - u_1}{\lambda + \lambda\chi + u_1} e^{\lambda(z-h)} \right) \lambda^2 J_0(\lambda r) d\lambda \quad (8-1)$$

where σ and χ are the half-space conductivities and susceptibilities, $u_1 = \sqrt{\lambda^2 + i\mu_0(1+\chi)\sigma\omega}$ and we have made a quasi-static approximation. The Hankel transform in Equation (8-1) is computed using the digital filtering routine of Anderson (1982). The secondary field generated from the half-space will be

$$H_{sz}(\mathbf{x}, \omega, \sigma, \chi) = H_z(\mathbf{x}, \omega, \sigma, \chi) - H_z(\mathbf{x}, \omega, 0, 0) \quad (8-2)$$

where $H_z(\mathbf{x}, \omega, 0, 0)$ is the free-space response. The time-domain secondary field response, $B_s(t)$, is obtained by convolving Equation (8-2) with the transmitter waveform. Details of the calculations are provided in Appendix B.

For the exponential ramp-on, Figure 8-2 shows the component of the secondary field response (as a proportion of the peak primary field response) for different half-space conductivities and susceptibilities at two lateral distances from the transmitter. For a non-conducting earth, the secondary field response increases in direct proportion with the increasing primary field (secondary and primary fields in phase) and reaches a maximum of

$$B_s = H_{sz}(\mathbf{x}, 0, 0, \chi) \left[1 - \exp\left(-\frac{t_{\max}}{\tau}\right) \right] \approx H_{sz}(\mathbf{x}, 0, 0, \chi) \quad (8-3)$$

where t_{\max} is the on-time of the exponential ramp and τ is the time-constant of the transmitter loop. The ratio of secondary to primary fields will be

$$\frac{B_s}{B_p} = \frac{H_{sz}(\mathbf{x}, 0, 0, \chi)}{H_z(\mathbf{x}, 0, 0, 0)} \quad (8-4)$$

The amplitude of $H_{sz}(\mathbf{x}, 0, 0, \chi)$ increases as a function of the half-space susceptibility, and consequently so does the contribution of the secondary field compared to the primary field.

For non-zero conductivities the changing primary magnetic field induces eddy currents and the primary and secondary fields are no longer in phase. As time goes on, the primary field starts to reach a steady state value and the eddy currents diffuse and decay as a function of time. At small distances from the transmitter (e.g. 4 m, Figure 8-2a), the eddy currents induced in even very highly conducting soil (1 S/m) have mostly decayed by 25 ms and the secondary field is approximately the same as that from a non-conducting earth. Thus, from the perspective of transmitter localization, it is the susceptibility and not the conductivity that is important. At larger distances from the transmitter (e.g. 32 m, Figure 8-2b), the half-space conductivity begins to become important. This is caused by the propagation of circular current filaments (commonly referred to as “smoke-rings”) that radiate away from the point directly beneath the transmitter.

For a circular loop on a half-space of conductivity σ , Nabighian (1979) showed that the current loop will be at a radius a at t seconds after a step off:

$$t = \frac{\mu_0 \sigma a^2}{2} \quad (8-5)$$

At low-conductivities the eddy currents diffuse rapidly away from the transmitter and, when the range is < 50 m, do not contribute appreciably to the B-field response of the half-space at times exceeding $1 \mu\text{s}$ (Figure 8-3). As the conductivity increases the eddy currents diffuse more slowly and persist, at ranges < 50 m, for times on the order of 1 ms.

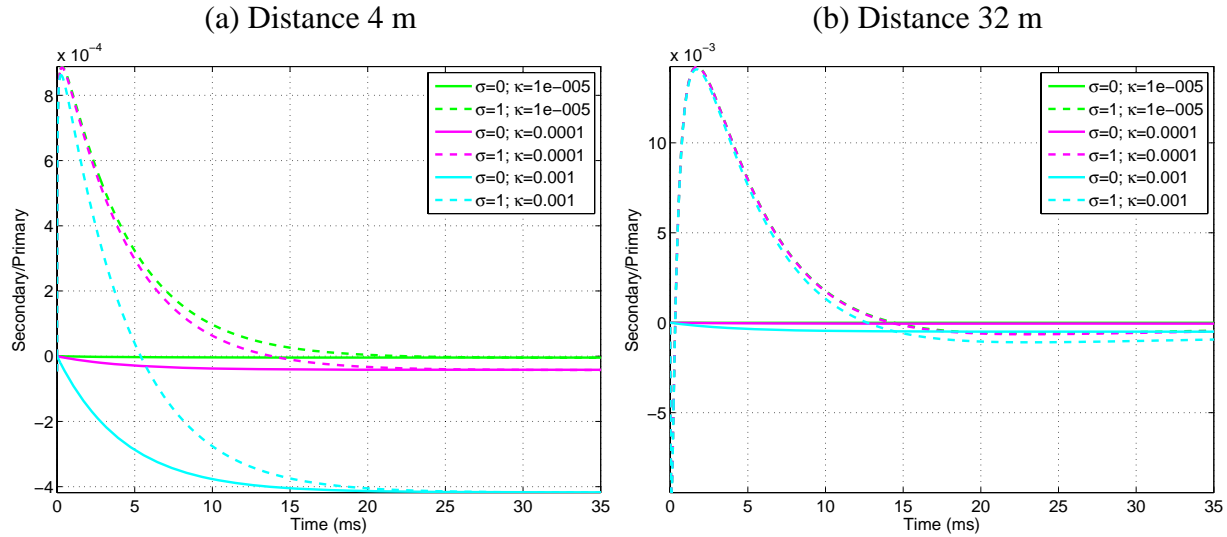


Figure 8-2. B-field response from a half-space of different conductivities/susceptibilities at (a) 4 m from the dipole source; and (b) 32 m distance. The conductivities are given in S/m and the volume susceptibilities in SI.

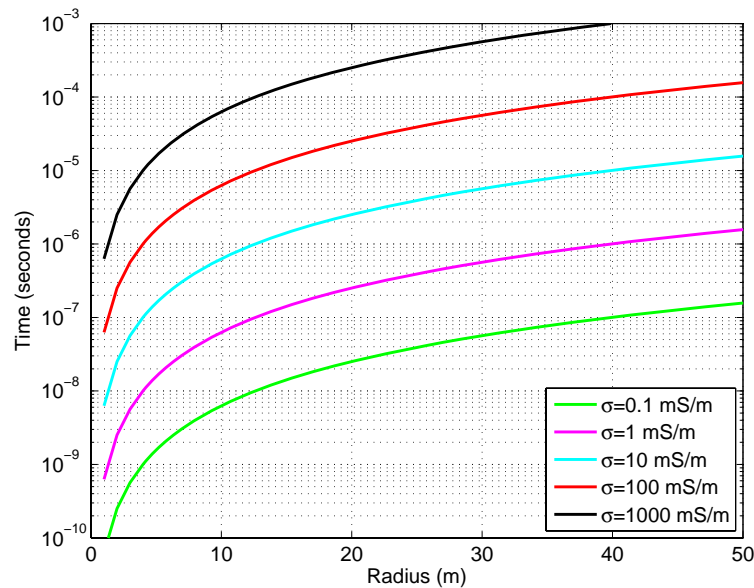


Figure 8-3. Time-evolution of smoke-ring radius for half-spaces of different conductivities.

8.3. dB/dt response from a conductive/susceptible half-space

Figure 8-4 shows the secondary B-field and dB/dt response associated with the linear ramp-off from the EM63 waveform. The computations were made for a non-conducting half-space (0 conductivity) with susceptibility of 0.001 SI. As the earth is non-conducting, no-eddy currents are induced and the secondary field changes in phase with the primary field. The dB_s/dt response during the step-off is constant and given by the expression,

$$\frac{dB_s}{dt} = \frac{H_{sz}(\mathbf{x}, 0, 0, \chi)}{\Delta t} \quad (8-6)$$

where Δt is the time-required for the step-off (100 microseconds for the EM63). The ratio of secondary to primary fields will be:

$$\frac{dB_s / dt}{dB_p / dt} = \frac{H_{sz}(\mathbf{x}, 0, 0, \chi) / \Delta t}{H_z(\mathbf{x}, 0, 0, 0) / \Delta t} = \frac{H_{sz}(\mathbf{x}, 0, 0, \chi)}{H_z(\mathbf{x}, 0, 0, 0)} \quad (8-7)$$

Note that this expression is exactly the same as that for the B-field response given in Equation (8-4). Thus, for a non-conducting earth the ratio of secondary to primary fields is the same for B-field and dB/dt sensors.

The half-space response for the linear ramp is more complicated when the earth is conductive (Figure 8-5) as the secondary field is no longer completely in phase with the primary field due to the generation and diffusion of eddy-currents. For conductivities less than about 10 mS/m, the dB/dt response from 50 microseconds onwards converges to a value close to that of a non-conducting half-space. At larger conductivities, conductive effects continue to be important and the secondary field response is significantly larger than that from an equivalent non-conducting earth. As the distance from the transmitter increases, the eddy currents persist for longer and there is a larger difference in the secondary field compared to that from a non-conducting earth.

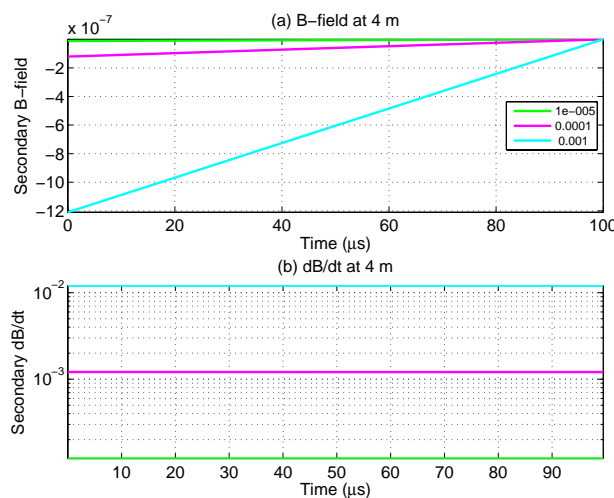


Figure 8-4. B-field (a) dB/dt (b) response from a non-conducting half-space of different susceptibilities (SI units) at 4 meters from the dipole source.

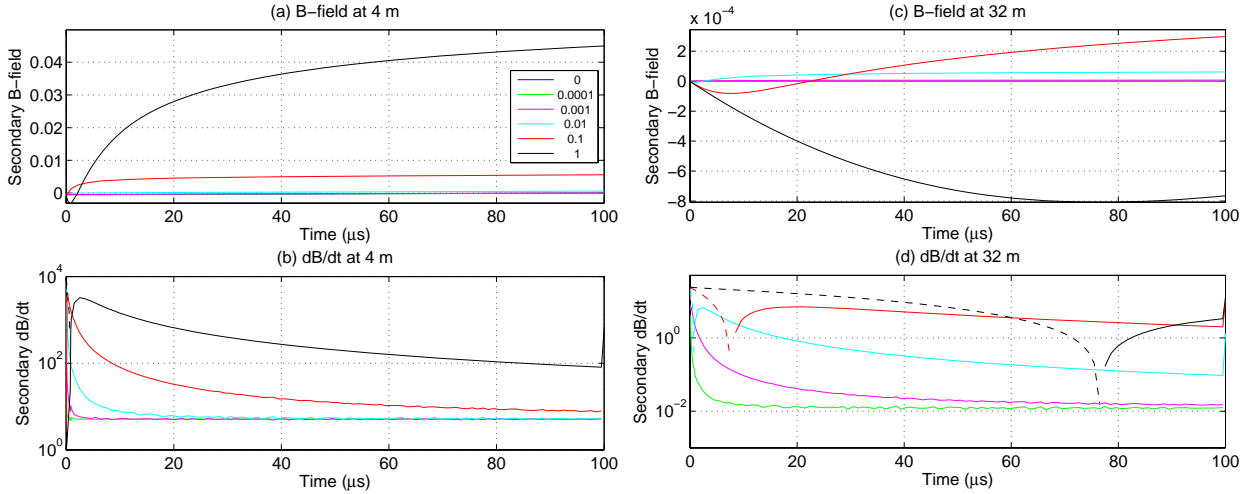


Figure 8-5. B-field (a and c) and dB/dt (b and d) response from a half-space of different conductivities and a susceptibility of 0.001 SI at 4 (a and b) and 32 (c and d) meters from the dipole source. The conductivities are given in S/m.

8.4. Localization error from the half-space

In Figure 8-6 we provide estimates of the localization error for a B-field sensor at different ranges caused by half-spaces of different conductivity and susceptibility. To obtain the estimates we first computed, at each range value, the change in the component of the primary field caused by moving the sensors 1 cm horizontally away from the dipole source: Δb_z . The location error was then estimated by dividing the component of the secondary field by Δb_z . The location error increases log-linearly with the susceptibility and also increases as a function of the range. Conductivity of up to 1 S/m has very little impact on the location error, except at large ranges and low-susceptibilities. The location error only rises above 1 cm at susceptibilities exceeding 0.002 SI at large ranges and 0.01 SI at shorter ranges. These values are higher than the susceptibilities expected to be encountered in soils in the continental USA.

In Figure 8-6b, we show the impact of secondary field gradients on the localization error. We assume the gradient is calculated as the change in component of the magnetic field in the range direction (that is, in the direction directly away from the transmitter). Depending on the range, localization errors are reduced by about 25 to 35% when using the gradient. Most of this decrease can be attributed to the greater relative change of the primary field that is required to change the gradient estimate by 1 cm, compared to the change required by the field value itself (4th power of distance compared to 3rd power of distance).

Figure 8-7 compares the localization error of B-field and dB/dt sensors. At 4 m from the transmitter (Figure 8-7a), the location error of the dB/dt sensor only differs significantly from that of the b-field sensor at small susceptibilities and conductivities of about 100 mS/m or greater. At 32 m from the transmitter (Figure 8-7b), there is an appreciable difference in location errors for soils with conductivities on the order of 10 mS/m. This is a common value of conductivity to encounter within the continental United States (e.g. FCC, 2009). Figure 8-4c shows that, for this conductivity, the range has to be at least 16 m before there is an appreciable difference relative to a non-conducting half-space.

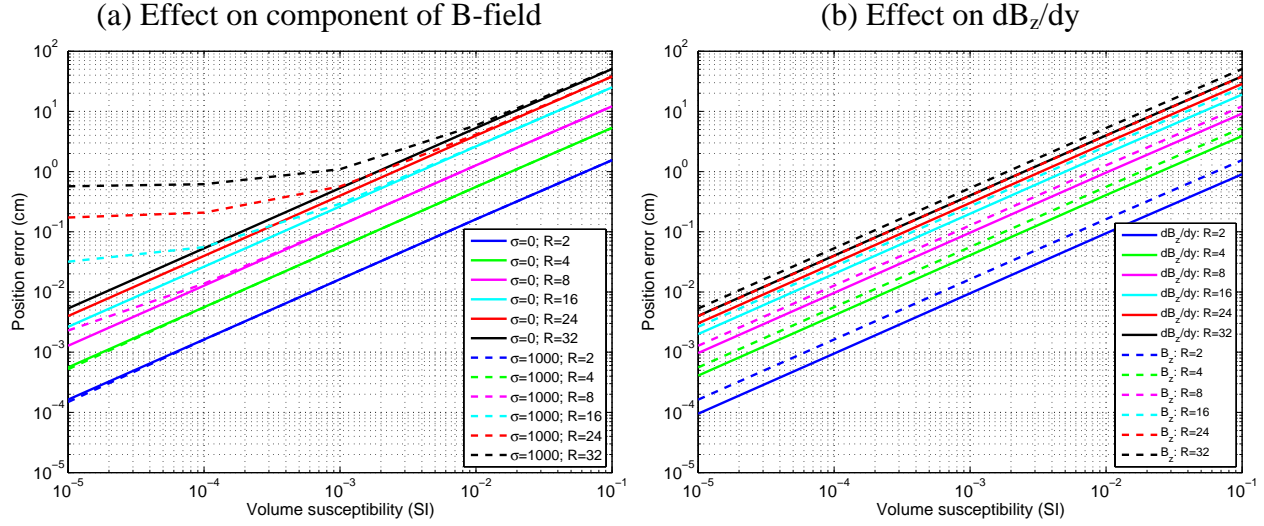


Figure 8-6. (a) Effect of conductivity (in S/m) and permeability on localization of the transmitter using the value of the B-field; (b) impact on localization error when using the horizontal gradient of the directed B-field (conductivity = 0 S/m).

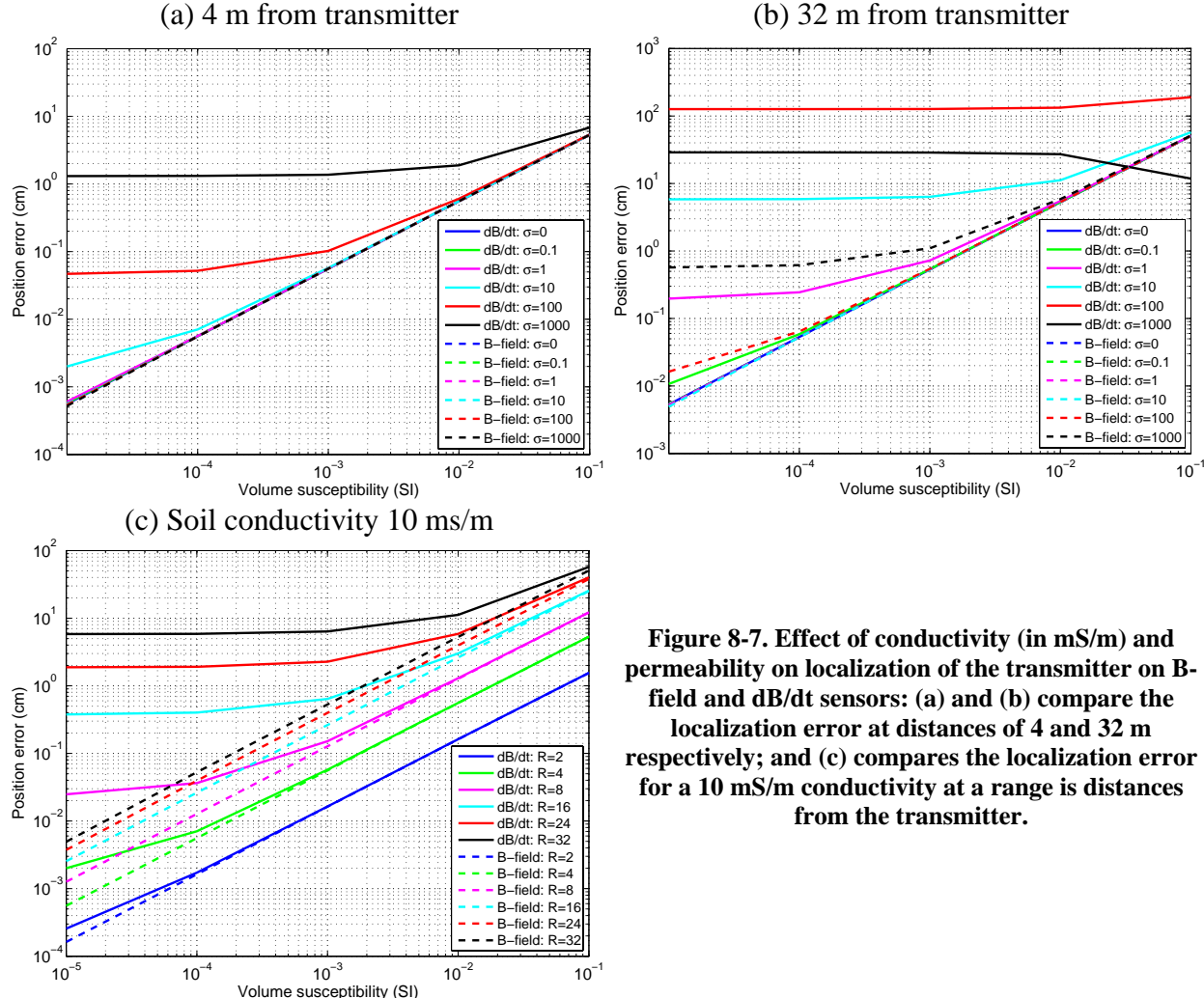


Figure 8-7. Effect of conductivity (in mS/m) and permeability on localization of the transmitter on B-field and dB/dt sensors: (a) and (b) compare the localization error at distances of 4 and 32 m respectively; and (c) compares the localization error for a 10 mS/m conductivity at a range of distances from the transmitter.

8.5. Generalization to other waveforms

The results presented above apply to a transmitter with equivalent transmitter waveform to an EM63. To generalize to transmitters with different loop time-constants and transmitter on-times, we recognize that if $B_s(t, \sigma, \chi, \tau_1)$ is the secondary field response at time t for time-constant τ_1 , then the secondary field response for a different time-constant, τ_2 can be obtained as:

$$B_s\left(\frac{t\tau_2}{\tau_1}, \frac{\tau_2\sigma}{\tau_1}, \chi, \tau_2\right) = B_s(t, \sigma, \chi, \tau_1) \quad (8-8)$$

This expression can be derived by simple algebraic manipulation of the equation for the inverse Fourier transformation of the convolution of the impulse response function with the transfer function of the transmitter. Equation (8-8) allows us to calculate localization errors for a single exponential time constant (such as for $\tau=1$ ms in Figure 8-8) and infer the error for a different exponential time-constant. For instance, the secondary field (and hence localization error) for $\tau=1$ ms, $\sigma=10$ mS/m at $t=3$ ms is identical to the secondary field for $\tau=5$ ms, $\sigma=50$ ms/m and $t=15$ ms.

Figure 8-8 shows the estimated localization error as a function of time, after current turn-on for a transmitter loop time-constant of 1 ms. The figure demonstrates that conductivity will only be a significant source of error when $\sigma/\tau > 100$ Sm $^{-1}$ t $^{-1}$ and the range is larger than about 15 m. At lower conductivities and/or ranges the localization error after about four time constants is almost identical to that for a non-conducting half-space. In fact, the response from the conductive half-space can be smaller than that of the non-conducting half-space for times less than 4 loop time-constants. This occurs because the initial eddy current response is in opposition to the induced magnetization.

The same scaling argument as Equation (8-8) applies for the linear step-off and a dB/dt sensor. For instance, the localization error for $\Delta t=100$ μ s (EM63 waveform) and conductivity of 10 mS/m, will be the same for $\Delta t=10$ μ s (MetalMapper waveform) and a conductivity of 1 mS/m. Figure 8-9 shows the estimated localization error for a half-space of susceptibility 0.01 SI as a function of time, after the start of the ramp-down for a linear turn-off of 100 μ s. Propagation of the eddy current smoke ring past the sensor location causes the zero crossings in the curves for (i) range 32 m and $\sigma/\Delta t=1,000$ Sm $^{-1}$ t $^{-1}$; and (ii) range 16 m and $\sigma/\Delta t=10,000$ Sm $^{-1}$ t $^{-1}$. Note that the zero crossing for range 32 m and $\sigma/\Delta t=10,000$ Sm $^{-1}$ t $^{-1}$ occurs after the end of the ramp-down. Figure 8-9b compares the localization error at $t=\Delta t$ for different conductivities as a function of range. The effect of conductivity increases with range and starts to become important whenever $\sigma/\Delta t > 100$ Sm $^{-1}$ t $^{-1}$.

8.6. Application to the Geonics EM61

The Geonics EM61 is one of the most widely used instruments in the UXO remediation community. The transmitter waveform for the 1 m by 0.5 m standard EM61 Mk II model is similar to the EM63, with a transmitter time-constant of 3.46 ms (compared to 4.3 ms for the EM63) and a linear ramp turn-off time of 114 μ s (compared to 100 μ s for the EM63). The EM61 transmit pulse is much shorter than that of the EM63 being on for only 3.3 ms (compared to 34 ms for the EM63). In terms of B-field application this means that we are within the regime of $t \sim \tau$ in Figure 8-8. Close inspection of that figure reveals the potential for significant conductivity

effects at closer range ($R=16$ m and $\sigma/\tau > 1000 \text{ Sm}^{-1}\text{t}^{-1}$) and at lower conductivities ($R=32$ m and $\sigma/\tau > 100 \text{ Sm}^{-1}\text{t}^{-1}$) than would occur with the EM63 ($t \sim 8\tau$). Bear in mind, that these conductivities are atypically high for North American soils and would not often be encountered. In terms of dB/dt application the soil response generated by the EM61 and EM63 sensors will have an almost identical localization error. This means that a B-field sensing technique will retain its advantage over dB/dt sensors in conductive soil environments.

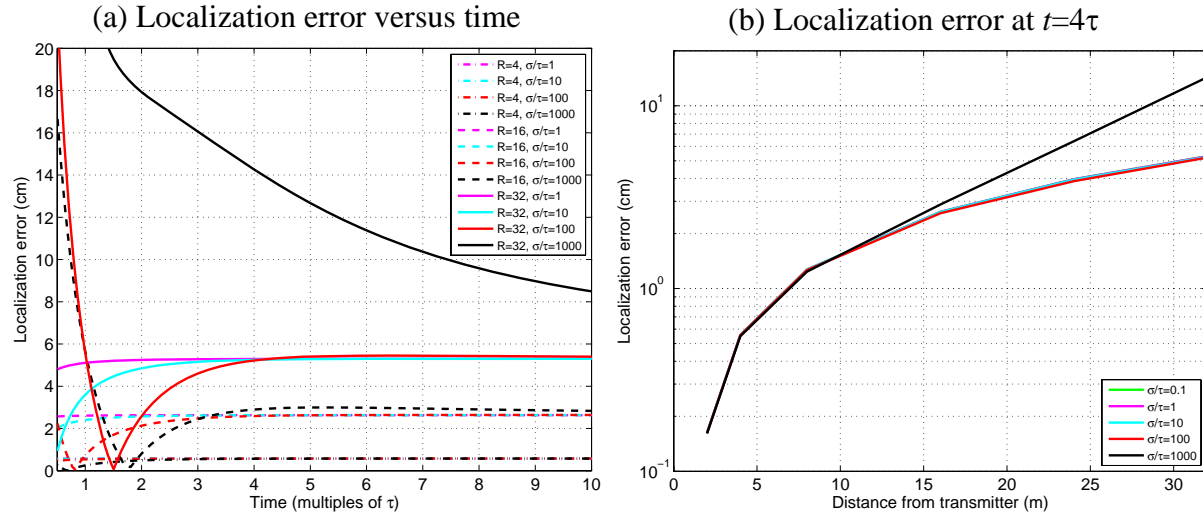


Figure 8-8. For a B-field sensor, the estimated localization error as a function of time (a) after current initiation for an exponential turn-on at three different distances (4, 16 and 32 m) for a half-space with susceptibility $\chi=0.01 \text{ SI}$. The results are given in terms of σ/τ which has units of $\text{Sm}^{-1}\text{t}^{-1}$. In (b) the localization error as a function of range at a time of $t=4\tau$ is shown for different conductivities.

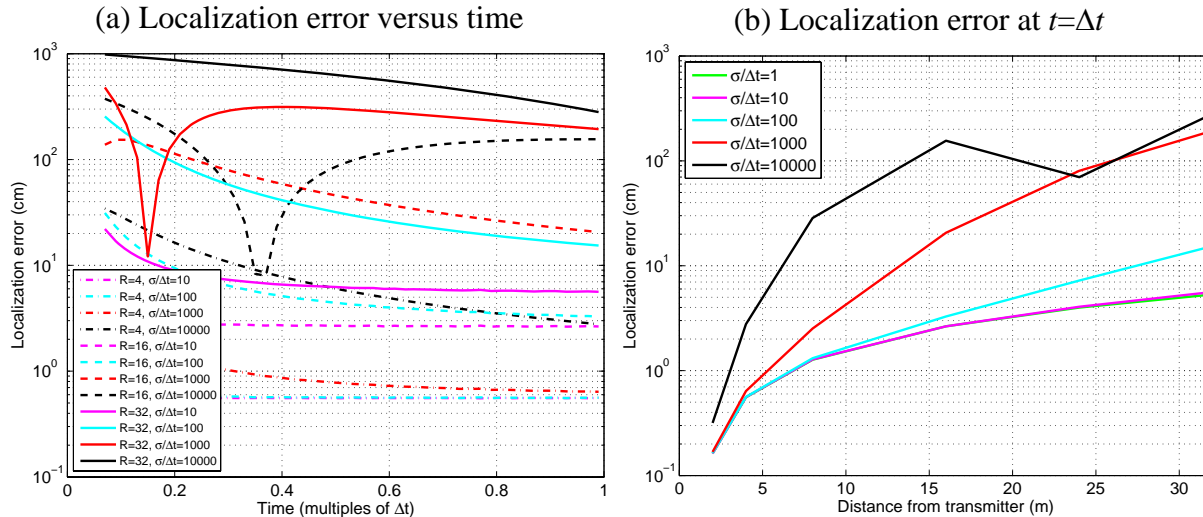


Figure 8-9. For a dB/dt sensor, the estimated localization error as a function of time after the start of the linear ramp-off at three different distances (4, 16 and 32 m) for a half-space with susceptibility $\chi=0.01 \text{ SI}$. The results are given in terms of $\sigma/\Delta t$ which has units of $\text{Sm}^{-1}\text{t}^{-1}$. In (b) the localization error as a function of range at a time of $t=\Delta t$ is shown for different conductivities.

8.7. Preliminary look at application in the marine environment

One potential application area for the B-field sensing concept explored in this project would be for location of electromagnetic induction sensors in the marine environment. For towed sensors, current techniques for positioning marine sensors rely on extrapolation from surface measurements (through measurements of sensor depth, cable tow angles etc) or on acoustic positioning techniques. Location errors with these systems are range dependant and often exceed 30 cm or more at ranges of 10 m or less. To apply the active positioning techniques developed here we would need to account for the large conductivity of sea-water (nominally 4 S/m). As an initial feasibility test, we assume that the gradiometer is immersed in sea-water (for instance it could be rigidly attached to the rear of the tow-vessel) and that the transmitter is at a depth of 5 m below the surface. With this configuration, we can approximate the magnetic field response from the transmitter using the step-on response of a vertical magnetic dipole, m , in a whole space with conductivity 4 S/m, which is an expression given as Equation 2.56 in Ward and Hohmann (1987),

$$\mathbf{B} = \frac{m\mu_0}{4\pi r^3} \left[\frac{Az}{r^2} \mathbf{x} - B \hat{\mathbf{z}} \right] \quad (8.9)$$

where

$$A = \left(\frac{4}{\pi^{1/2}} \theta^3 r^3 + \frac{6}{\pi^{1/2}} \theta r \right) \exp(-\theta^2 r^2) + 3 \operatorname{erfc}(\theta r) \quad (8.10)$$

and

$$B = \left(\frac{4}{\pi^{1/2}} \theta^3 r^3 + \frac{3}{\pi^{1/2}} \theta r \right) \exp(-\theta^2 r^2) + \operatorname{erfc}(\theta r) \quad (8.11)$$

with

$$\theta = \sqrt{\frac{\mu_0 \sigma}{4t}} \quad (8.12)$$

In Figure 8-10 we plot the ratio of the B_y and B_z magnetic fields in sea-water compared to free-space (where they would be constant with time) for different lateral offsets in the y -direction. The transmitter turns on at time $t=0$, and due to the high conductivity of the sea-water, the magnetic field does not reach the receiver until sometime later. This delay time is on the order of 1 μ s when the receiver is directly over the dipole and rises to 0.2 ms at 40 meters lateral distance (Figure 8-10d). The B_y field monotonically increases with time and eventually reaches approximately the same value as it would in free-space. The B_y field reaches 99.9% of the free-space value after 0.03 ms directly over the transmitter, after 4 ms at 20 m lateral distance and after 20 ms at 40 m lateral distance. The ratio of sea-water and free-space B_z fields has a more complex relationship as a function of time, partly because the free-space field has a zero crossing at about 7 m lateral distance from the transmitter (Figure 8-10c). The propagating smoke-rings generated by the rapid turn-on of the transmitter cause the B_z field in seawater to exceed the free-space values for part of the time-range.

We can draw the following conclusions from this initial feasibility analysis:

- 1) Coil based sensors (dB/dt) are unsuitable because of the strong effects of conductivity in the $100 \mu\text{s}$ time-range.
- 2) B-field sensors could be used for positioning of transmitters with EM63 characteristics without undue influence from the sea-water at ranges up to 30-40 meters. While the magnetic field response is a relatively complex function of range and time, the field reaches an equivalent free-space value at times less than 10 ms at distances up to 20 m and within 30-40 ms at distances up to 40 ms.
- 3) B-field sensors may be applicable for positioning transmitters with shorter on-times (such as the EM61), although the sea-water conductivity would need to be included in the analysis at ranges exceeding 10 meters.

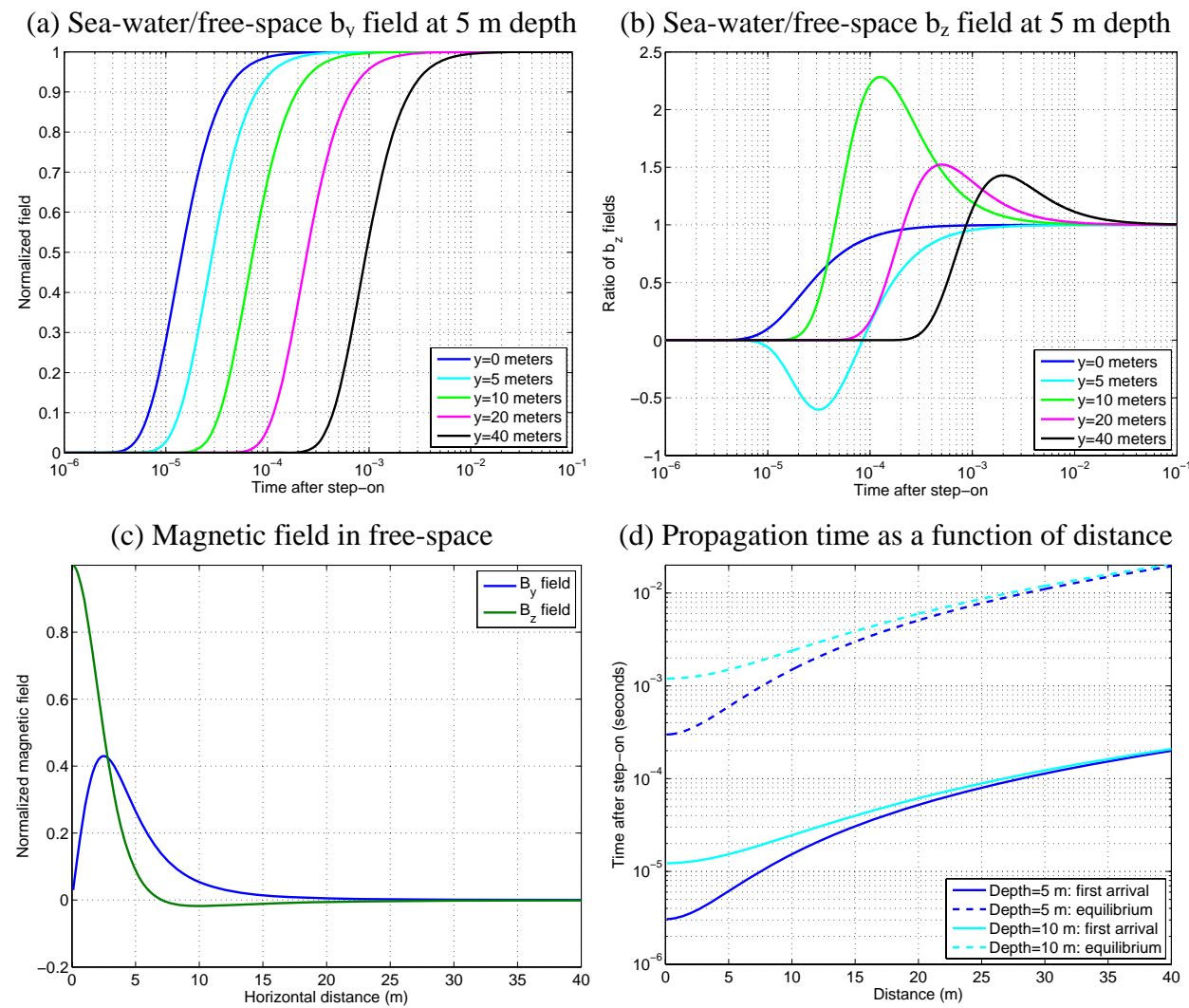


Figure 8-10. The ratio of the B_y (a) and B_z (b) fields in sea-water (4 S/m conductivity) versus free-space as a function of time following the step turn-on of a directed magnetic dipole 5 meters below the receiver at different lateral offsets (in the y -direction). (c) The spatial profile along the y -direction of the magnetic field in free-space (note that $B_x=0$). The time-taken (d) for the sea-water/free-space ratio of B_y to reach 0.1 and 99.9%, for directed magnetic dipoles at 5 and 10 m below the receiver.

8.8. Localization error caused by ferrous objects

One issue that we have thus far neglected is the effect of large ferrous objects on the localization procedure. We envision that the gradiometer would be positioned away from any large ferrous anomalies, so that objects near the transmitter will cause the most concern. The largest secondary field will be generated when the object is directly below the transmitter and oriented vertically. We consider only the B-field response and assume that the transmitter on-time is sufficiently long so that we can use a magnetostatic assumption. Because we want to model situations where the object is very close to the transmitter we cannot assume that the field is dipolar and instead need to use the Biot-Savart law. Assuming the loop is a square of side dimension l and carries a current of I amperes, then the vertical field along the center line of the loop at a distance z will be

$$B_z = \frac{\mu_0 I}{2\pi} \frac{l^2}{(l^2/4 + z^2) \sqrt{l^2/2 + z^2}} \quad (8.13)$$

We model the ferrous object as a prolate spheroid of radius r and length re where e is the aspect ratio of the spheroid (e.g. Billings, 2004). We further assume that the spheroid is aligned either vertically or horizontally (so that the inducing field is along a principal axis). Then the induced magnetic dipole will be

$$m_{in} = \frac{4}{3\mu_0\pi} r^3 e \bar{\chi} B_z \quad (8.14)$$

where $\bar{\chi}$ is the effective susceptibility along the axis aligned with the field. After substituting the expression for B_z from the transmitter and simplifying (assuming $l=1\text{m}$ as for the EM63) we find

$$m_{in} = \frac{2e\bar{\chi}I}{3} \frac{r^3}{(1/4 + z^2) \sqrt{1/2 + z^2}} \quad (8.15)$$

from which it follows that

$$\frac{m_{in}}{m} = \frac{2e\bar{\chi}}{3} \frac{r^3}{(1/4 + z^2) \sqrt{1/2 + z^2}} \quad (8.16)$$

If we assume an aspect ratio of $e=3.25$ this results in $\bar{\chi} \approx 10$ along the spheroid axis and $\bar{\chi} \approx 2.2$ perpendicular to the axis. For a 155 mm projectile we have $r=0.155/2=0.0775$ meters so that at 0.5 m below the transmitter the ratio of moments is 2.2% for the vertical orientation and 0.5% for horizontal orientation. At 1 meter below the transmitter the ratio of moments drops to 0.6% for vertical orientation and 0.2% for horizontal excitation.

We now need to estimate what impact the dipole moment induced within the spheroid has on the total magnetic field recorded by the B-field sensor. As the sensor distance from the transmitter increases the distance and bearing from the sensor to the transmitter and object will approach the same values. Thus the ratio of fields will approach the same value as the ratio of moments,

$$\frac{B_{sz}}{B_{pz}} \sim \frac{m_{in}}{m} \quad (8.19)$$

Where B_{pz} and B_{sz} are the primary and secondary fields in the direction. The localization error at a lateral distance of y meters is

$$\Delta y = \frac{B_{sz}}{B_{pz}} \frac{y}{3} \sim \frac{m_{in}}{m} \frac{y}{3} = \frac{2e\bar{\chi}}{3} \frac{r^3}{\sqrt{1/4 + z^2} \sqrt{1/2 + z^2}} \frac{y}{3} \quad (8.18)$$

Figure 8-11 plots this estimated localization error as a function of lateral distance for a 155 mm projectile and an 81 mm mortar. Results are shown for two vertical distances beneath the transmitter (0.5 and 1 m) and for vertical and horizontal orientation. In the worst case scenario (directly passing over a vertical 155 mm projectile) the location error is 4 cm at 5 m and grows to 15 cm at 20 m lateral distance. For horizontal orientation of the 155 mm projectile the location error is significantly smaller: 0.9 cm at 5 m offset and 2.5 cm at 20 m offset. If the projectile is in a vertical orientation but twice as far beneath the transmitter (1 m instead of 0.5 m) the location error reduces to 1 cm at 5 m lateral offset and 4 cm at 20 m offset. The error decreases to 0.3 cm at 5 m offset and 1 cm at 20 m offset when the 155 mm projectile is in a horizontal orientation. The location errors are a factor of

$$\left(\frac{155}{81}\right)^3 = 7$$

times smaller for the 81 mm mortar and are never worse than 2 cm at 20 m lateral offset.

(a) Localization error from a 155 mm projectile (b) Localization error from a 81 mm mortar

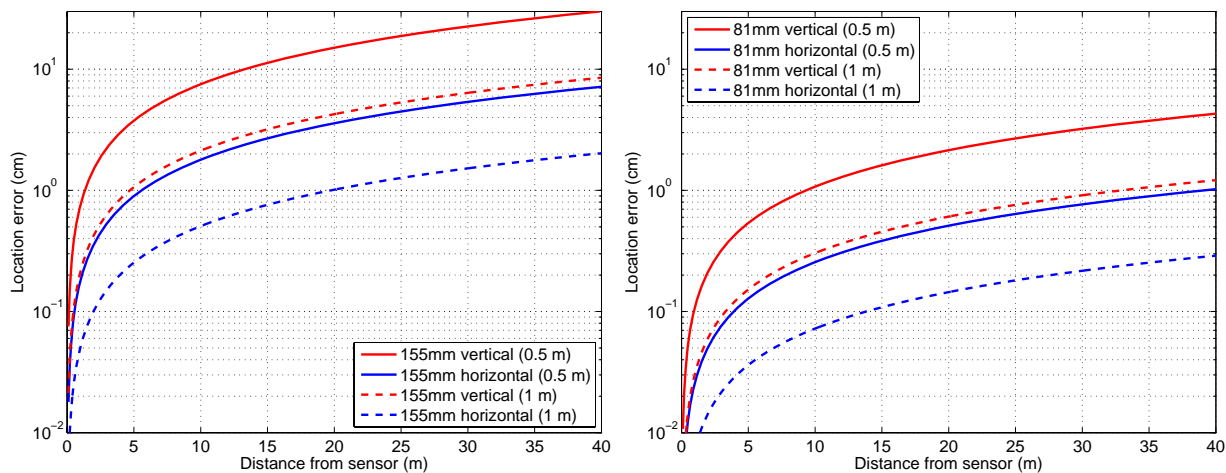


Figure 8-11. Estimated worst-case localization errors for (a) a 155 mm projectile and (b) a 81 mm mortar located 0.5 or 1.0 m directly below the transmitter.

9. Conclusions

9.1. Concept

The feasibility of using a suite of magnetometers / gradiometers to provide some form of useful location information on the position of an active dipole / magnetic source has been demonstrated. Even using first-order gradients estimates, location within half a metre at up to 9 metres distance has been shown to be possible.

LSQ optimization improves the accuracy of the system further, however it is fairly clear that some systemic inaccuracy remains, as the positions of the cart were typically known to within 10-20 mm from the GPS system, whereas the positional errors sometimes extend to 250 mm. Two motion trials indicate that moving the cart does not cause any significant problems in locating it, at least at walking pace. The tilt trial indicates that it is certainly also feasible to estimate the tilt of the system, although the accuracy of this estimate is not known in any quantified way currently.

9.2. Accuracy of modelled system

Compared to a model of the geometry of the system, and assuming a dipole source, the data shows remarkably good correlation for the standard Wilson inversion, as similar offsets to the true position are noted in both sets of data (c.f. §2 to §4). However the model shows the LSQ optimized inversions converging to the true location of the cart, and while the LSQ optimized solutions were more accurate than the Wilson inversions, some inaccuracy remained.

This suggests that some aspects of the system the model does not consider may be important, such as the true nature of the magnetic source and the effects of the ground half-space on the transmit pulse. It may also suggest that there are some inadequacies with the acquisition / estimation hardware and software that introduce bias into the inversions.

Attempts to improve the validity of the model by incorporating these effects would provide further confidence in using it to evaluate different sensor configurations and algorithms without the explicit need to build and test these configurations in the field.

9.3. Ideal dipole assumption of the source

It has been demonstrated that modeling the field source as an ideal dipole is useful for locating the cart to within 200 mm of the true position (and often much closer). It is clear however that the field produced by such a distributed source diverges from this ideal dipole field, especially in proximity to the cart (see §7.5).

9.4. SQUID gradiometer

The SQUID system did not produce a good estimate of the B-field, thereby excluding the use of both Nara's method and any kind of LSQ optimization. With the Wilson inversion, however, it placed the cart 5.19 m away from the sensor, which is within 10 cm of the true position. This

accuracy compares favourably to the fluxgate instrument using the Wilson inversion. This is probably due to the shorter base line (50 mm vs. 600 mm) and the fact that all estimates are made within the same small volume on the SQUID system, whereas the fluxgate system extends 600 mm baselines from a single point in 3 different directions.

The SQUID system's noise performance was compromised by the lack of an anti-aliasing filter on the sampling system, resulting in the folding back of up to 3 kHz of noise in the signal.

9.5. Effect of soil conductivity and susceptibility

For a B-field sensor, conductivity effects are only significant (> 1 cm location error) whenever:

- $\sigma/\tau > 1000 \text{ Sm}^{-1}\text{t}^{-1}$ and the range is greater than 15 m (e.g. $\sigma=1000 \text{ mS/m}$ and $\tau=1 \text{ ms}$).

For a dB/dt sensor conductivity effects are important whenever:

- $\sigma/\Delta t > 100 \text{ Sm}^{-1}\text{t}^{-1}$ at ranges of 15 m or more (e.g. $\sigma=1 \text{ mS/m}$ and $\Delta t=10 \mu\text{s}$)
- $\sigma/\Delta t > 1000 \text{ Sm}^{-1}\text{t}^{-1}$ at ranges of 5 m or more (e.g. $\sigma=10 \text{ mS/m}$ and $\Delta t=10 \mu\text{s}$);
- $\sigma/\Delta t > 10000 \text{ Sm}^{-1}\text{t}^{-1}$ at any range (e.g. $\sigma=100 \text{ mS/m}$ and $\Delta t=10 \mu\text{s}$).

Soil susceptibility strongly affects the localization error and has the same impact on B-field and dB/dt sensors. Errors of 1 cm or greater are caused whenever:

- >0.02 SI at ranges of 4 m or more;
- >0.008 SI at ranges of 8 m or more;
- >0.004 SI at ranges of 16 m or more;
- >0.002 SI at ranges of 32 m or more.

A ten-fold increase in the susceptibility will cause a 10 fold increase in the localization error at a given range. For example a susceptibility of 0.04 SI will cause a 10 cm location error at 16 m distance.

We conclude that the relative immunity of the B-field localization technique to conductivity makes it a better choice for this application than a dB/dt sensor.

9.6. Potential application in the marine environment

For underwater positioning in the marine environment the conductivity of the seawater (4 S/m) can impact the localization accuracy. Using a whole-space model we found that:

- 1) Coil based sensors (dB/dt) are unsuitable because of the strong effects of conductivity in the 100 μs time-range.
- 2) B-field sensors could be used for positioning of transmitters with EM63 characteristics without undue influence from the sea-water at ranges up to 30-40 meters.

- 3) B-field sensors may be applicable for positioning transmitters with shorter on-times (such as the EM61), although the sea-water conductivity would need to be included in the analysis at ranges exceeding 10 meters.

9.7. Effect of large ferrous objects

We studied the effect of the secondary field from a large ferrous object on the localization accuracy. For a worst case scenario of a vertical 155 mm projectile located 50 cm directly below the transmitter, we found that the localization error was 4 cm at 5 meters lateral offset and 15 cm at 20 meters lateral offset. For horizontal orientation, or when the projectile was 1 m below the transmitter, the location error was always smaller than 1 cm at 5 meters and 4 cm at 20 meters. For an 81 mm mortar at 0.5 m below the transmitter, the location error was 0.5 cm at 5 meters and 2 cm at 20 meters.

We would not expect to encounter too many vertical 155 mm projectiles (or larger items) just 50 cm below the transmitter. Thus, while large ferrous objects have the potential to distort the localization results, in practice we don't anticipate that they will be a significant source of error in the localization procedure.

10. Future work recommendations

10.1. Improve EM63 / source model

Understanding the field produced by the EM63 cart is essential for accurate location inversion. The ideal dipole model is useful, but a better model of the source would allow the inversion routines to work better.

Further work would investigate more appropriate / accurate models for the field produced by the cart, based on fundamental laws (Biot-Savart Law, Amperes Current Law, etc) and test these models with experimentation. Finally, these refined models would need to be incorporated into the inversion algorithms and the performance of the system re-evaluated.

10.2. Iterative higher-order gradient estimation

It has been observed that using a single estimate of the first-order gradient results in systematic inaccuracies in the inversion. The main reason for this is the presence of higher-order gradients across the volume of the instrument, and these are not considered in estimating a single-value for the first-order gradient.

By applying iterative techniques to the first solution of the Wilson (or other) inversion, estimates of the second and higher order gradients may be made for that position and incorporated into a new estimation calculation for the first-order gradient.

Such a technique may result in fewer sensors being required in a useful instrument. Further work would investigate the validity of this concept, and test the accuracy gains (if any).

10.3. Different geometries and multiple instruments

A dimensional asymmetry has been shown to exist in the standard deviation of the positional information, dependent on the location of the cart.

Further work would quantify how this asymmetry varies around the instrument, and investigate any accuracy gains possible by judicious placement of the instrument with respect to the working area of the cart.

Additionally, it may be plausible to combine the results from two instruments, one placed along each edge of a working area (to form an 'L' shape), to enhance the precision of the positioning solutions by combining the best estimates of each dimension from the two instruments.

Further work in this area would investigate the gains achievable by multiple instruments, consider the extra costs involved, and develop any operational techniques required to ensure the instruments can be calibrated with respect to one another in the field.

10.4. Total field sensors

All of the inversion techniques demonstrated to date have involved 3-axis vector magnetometers, in which each individual sensor is sensitive to magnetic field in one direction only and requires

careful calibration with respect to the other 2 sensors to ensure the field measurements represent the orthogonal components of the vector field.

Further work would investigate the plausibility of using total field magnetometers in the form of total field gradiometry, or as an augmentation to vector-field magnetometry / gradiometry to provide useful positioning information with these sensors. Recent advances in total-field sensors sponsored by SERDP have the potential to significantly reduce the size, power consumption and cost of these sensors.

10.5. SQUID sensors

It has been shown that although the fluxgate-based instrument performance was limited by external interference and noise and not the intrinsic performance of the fluxgate, the smaller baseline and better noise profile of a SQUID gradiometer may be able to out-perform the fluxgate system significantly.

Even without this advantage, the noise, interference and estimation issues (which would impact both the SQUID and fluxgate systems), may have other solutions, which would enable both systems to improve their accuracy. In this situation, a SQUID-based system may be able to extend the useful range of the system further as it has a far lower intrinsic noise floor.

Further work would design and model a SQUID-based gradiometer / magnetometer for this problem. Evaluation of the output of these models would influence a decision to build a real SQUID system for further testing.

10.6. Acquisition systems

The acquisition system was a multiplexed 16 kHz 16 bit 16-channel ADC from National Instruments. Each channel was consequently sampled at 1 kHz, and each channel was sampled in order, 1/16000th of a second after the previous. The estimation of the fields concerned involved processing a reference fluxgate for timing information and using this information to perform averages on a non-uniform transmit pulse signal in the presence of significant 50 Hz interference. The quantization step in the ADC was 10.6 pT for the ± 50 mV input range. The precise impact of these technical characteristics of the system on the final estimate of the field measured by the fluxgates is unknown, and may have contributed to bias and noise above what the fluxgate sensor itself may have been capable of.

Further work would consider and estimate the impact these characteristics of the acquisition system have on the estimation of the fields at each sensor. Evaluation of the impacts may invoke a decision to design and implement a higher precision, higher sample rate and possibly synchronous acquisition system to capture the sensor signals.

10.7. Signal processing

In this trial, simple 20-sample averages taken during and after the transmit pulse were used to provide an estimate of the field produced by the source. This technique was used primarily to remove the 50 Hz interference from the signal. Very little time was spent looking at the true performance of this estimation method, other than noting it produced fairly good results for this trial.

Further work may investigate more sophisticated signal processing, filtering and estimation techniques that reduce the variability and the bias in the estimates of the field. This would improve the accuracy and precision of the position.

10.8. Potential application for underwater positioning

We conducted a preliminary feasibility analysis of using B-fields to locate an electromagnetic induction coil operating in the marine environment. The modeling indicated that the conductive effects will dissipate within 10 ms after pulse initiation at ranges up to 20 m and within 30-40 ms at ranges up to 40 m. Positioning of transmitters with equivalent characteristics to the EM63 thus appears to be feasible.

Further work would involve a more rigorous numerical evaluation of the feasibility and some preliminary measurements in a controlled setting. The ability to scale conductivity and the time-characteristics of the transmitter waveform would allow these tests to be down in a laboratory setting in a water tank.

11. References

Anderson, W.L., 1982. Fast Hankel transforms using related and lagged convolutions, *ACM Transactions on Mathematical Software*: 8, 344–368.

Bell, T., 2005, Geo-location Requirements for UXO Discrimination: Paper prepared for UXO Location Workshop, Annapolis, May 2005.

Billings, S. D., 2004. Discrimination and classification of buried unexploded ordnance using magnetometry: *IEEE Trans. Geosci. Remote Sens.*, 42, 1241–1251.

Bracewell, R., 1986. The Fourier Transform & Its Applications, 2nd edition: McGraw Hill.

Federal Communications Commission, 2009, M3 Map of Effective Ground Conductivity in the USA, <http://www.fcc.gov/mb/audio/m3/index.html>

Nabighian, M., 1979. Quasi-static transient response of a conducting half-space— An approximate representation: *Geophysics*, 44, 1700-1705.

Nara T., Suzuki S. and Ando S., 2006. A Closed-Form Formula for Magnetic Dipole Localization by Measurement of Its Magnetic Field and Spatial Gradients: *IEEE Trans. Magn.* 42, 3291-3293.

O'Neill, K., 2006, Presentation at the 2006 SERDP Symposium, November, Washington DC.

Rubens, S.M., 1945. Cube-surface coil for producing a uniform magnetic field: *Rev. Sci. Instr.*, 9, 243.

Schmidt, P., Clark, D., Leslie, K.E., Bick, M., Tilbrook, D.L. and Foley, C.P., 2004. GETMAG: a SQUID magnetic tensor gradiometer for mineral and oil exploration: *Exploration Geophysics*, 35, 297-305.

Smith, J. T., H. F. Morrison and A. Becker, 2004a. Parametric Forms and the Inductive Response of a Permeable Conducting Sphere: *J. Environmental and Engineering Geophysics*, 9, 213-216.

Smith, J. T., H. F. Morrison and A. Becker, 2004b. Resolution Depths for Some Transmitter-Receiver Configurations: *IEEE Trans. Geosc. & Rem. Sen.*, 42, 1215-1221.

Van Dam, R. L and Velbel, M. A., 2009, Relationships Between Magnetic Properties and Weathering Indices of Basaltic Rocks: *Eos Trans. AGU*, 90 (22), Jt. Assem. Suppl., Abstract. GP34A-02.

Ward, S.H., & G.W. Hohmann, 1987, Electromagnetic Theory for Geophysical Applications, in Electromagnetic Methods in Applied Geophysics: vol. 1, M.N. Nabighian (ed.), 131–311, Society of Exploration Geophysicists, Tulsa, Oklahoma.

Wilson, H., 1985. Analysis of the magnetic gradient tensor: Defence Research Establishment Pacific: Canada Technical Memorandum, 85-13, 47.

APPENDIX A: DATA

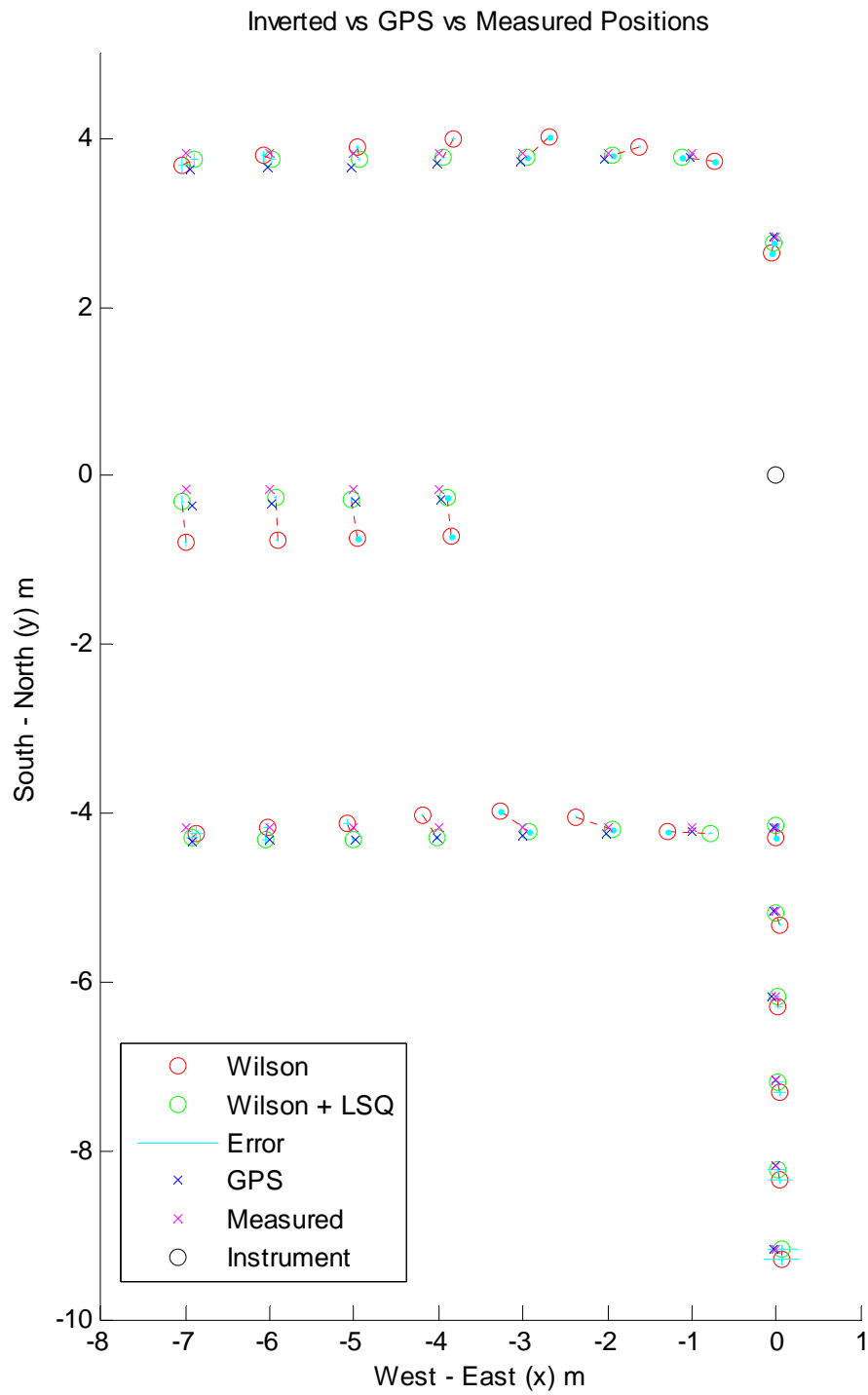
1. Summary of the numbered runs

Run #	Position		Notes
	Code	Value	
1	A	[-0.02, 2.83, 0.39]	Background test
2	A	[-0.02, 2.83, 0.39]	Test
3	A	[-0.02, 2.83, 0.39]	
4	O	[0.0, 3.83, 0.39]	
5	B	[-1.04, 3.79, 0.35]	
6	C	[-2.03, 3.75, 0.39]	
7	D	[-3.02, 3.73, 0.39]	
8	E	[-4.03, 3.70, 0.40]	ADC out of range, clipped, discarded.
9	E	[-4.03, 3.70, 0.40]	ADC out of range, clipped, discarded.
10	E	[-4.03, 3.70, 0.40]	
11	F	[-5.02, 3.67, 0.40]	
12	G	[-6.02, 3.65, 0.39]	
13	G'	[-6.95, 3.64, 0.34]	
14	L	[-6.92, -0.35, 0.47]	
15	K	[-5.97, -0.32, 0.46]	
16	J	[-4.98, -0.31, 0.43]	
17	I	[-3.97, -0.28, 0.44]	
18	V	[-6.92, -4.35, 0.36]	
19	V	[-6.92, -4.35, 0.36]	SQUID test
20	V	[-6.92, -4.35, 0.36]	SQUID 0°
21	V	[-6.92, -4.35, 0.36]	SQUID 120°
22	V	[-6.92, -4.35, 0.36]	SQUID 240°
23	V	[-6.92, -4.35, 0.36]	
24	T	[-5.00, -4.30, 0.36]	
25	S	[-4.01, -4.28, 0.40]	
26	R	[-3.01, -4.27, 0.39]	
27	Q	[-2.01, -4.23, 0.39]	
28	P	[-0.99, -4.20, 0.40]	
29	N	[-0.03, -4.16, 0.42]	
30	N	[-0.03, -4.16, 0.42]	SQUID 0°
31	N	[-0.03, -4.16, 0.42]	SQUID 120°
32	N	[-0.03, -4.16, 0.42]	SQUID 240°
33	N	[-0.03, -4.16, 0.42]	SQUID 0° - repeat at higher gain
34	N	[-0.03, -4.16, 0.42]	SQUID 120° - repeat at higher gain
35	N	[-0.03, -4.16, 0.42]	SQUID 240° - repeat at higher gain
36	West	Along S	West walk at ~0.5 m/s
37	North	Along N	North walk at ~0.5 m/s
38	W	[-0.03, -5.17, 0.40]	
39	X	[-0.05, -6.17, 0.42]	
40	Y	[-0.02, -7.17, 0.41]	

41	Z	[-0.02, -8.17, 0.39]	
42	SS	[-0.02, -9.7, 0.39]	
43	N	[-0.03, -4.16, 0.42]	EM63 was tilted back and forth 20°

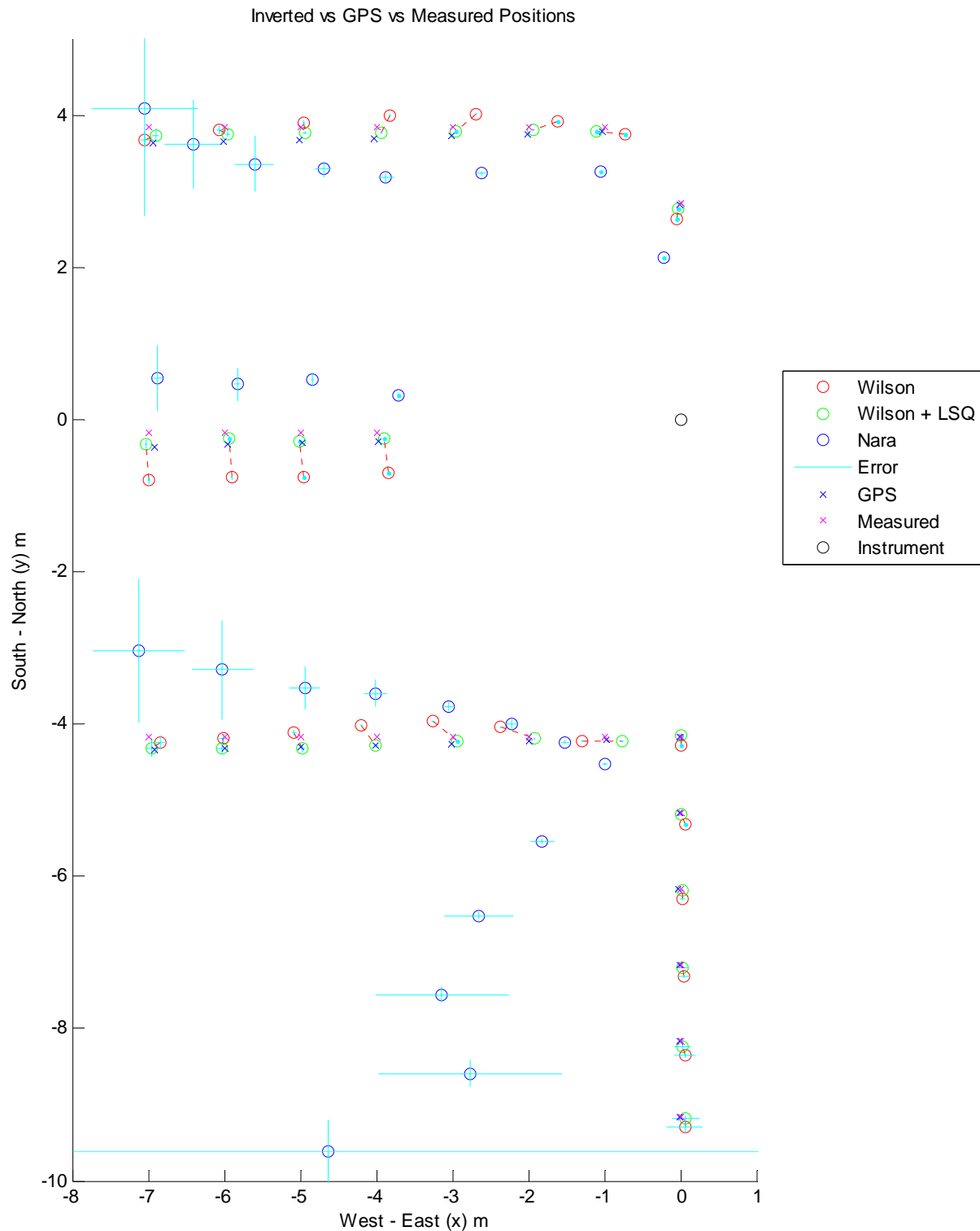
2. Overall results from field trial

This plot contains the entire suite of inversions (Wilson, and Wilson+LSQ) from all the measured positions during the field trial.



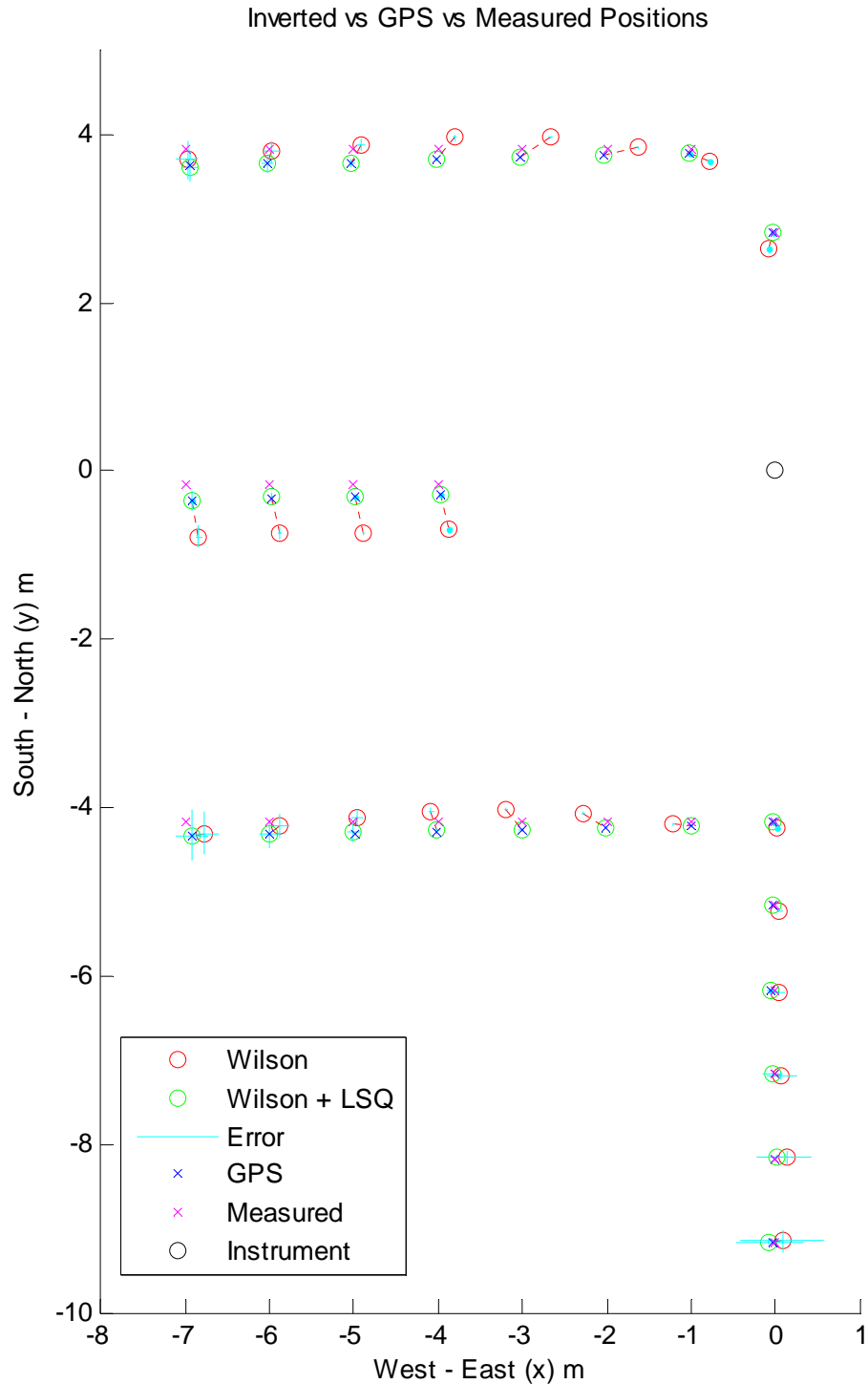
3. Overall results from field trial (with Nara)

This plot includes the Nara inversion mean positions and standard deviation bars.

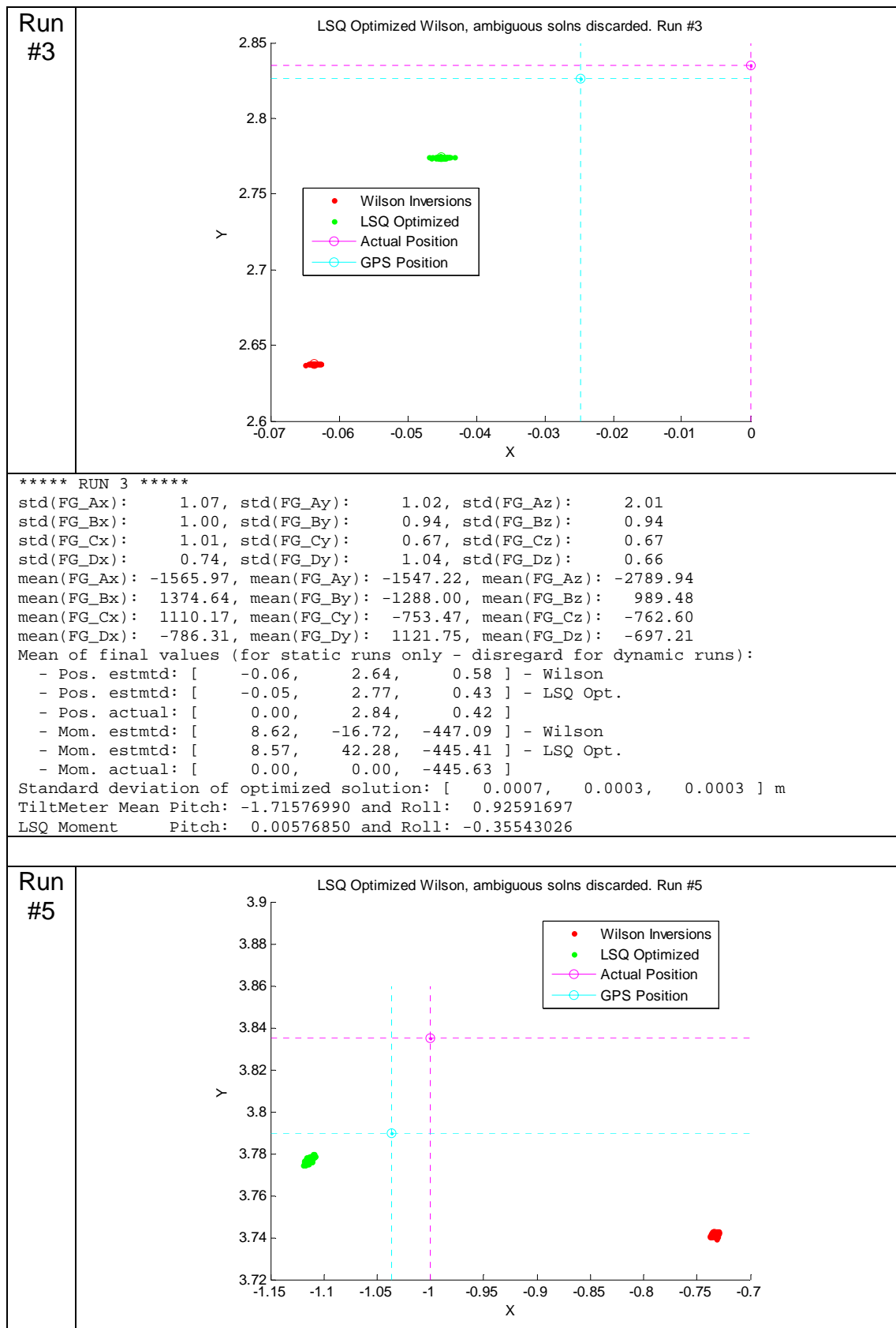


4. Overall results from Model

This plot contains the modelled geometries from the field trial. For each position, the GPS location was assumed to be the true position of the dipole – hence the LSQ optimized Wilson solutions all converge on the GPS position (unlike the real data).

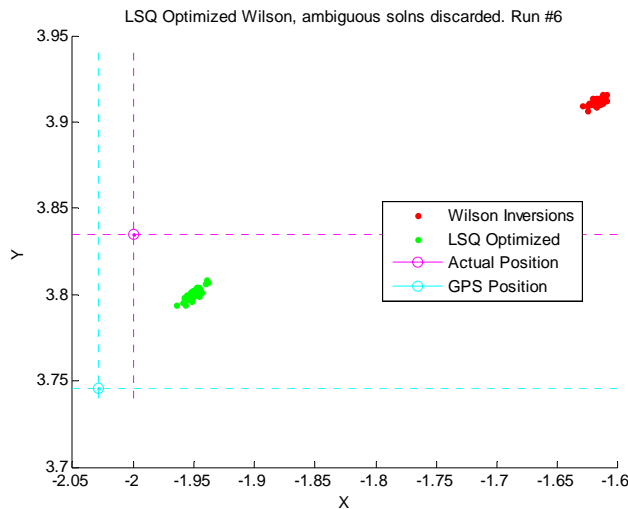


5. Individual Run Results

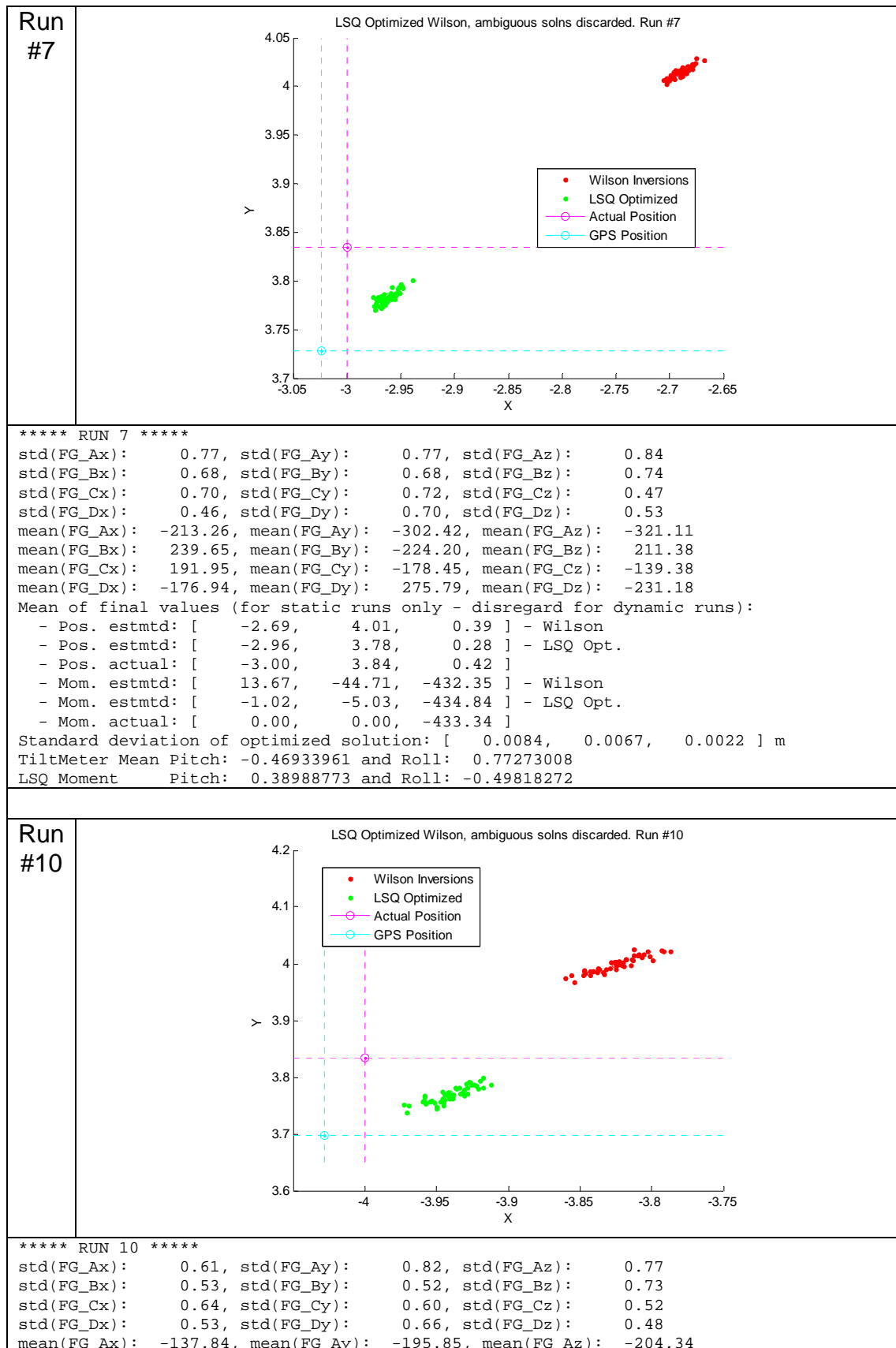


```
***** RUN 5 *****
std(FG_Ax): 0.47, std(FG_Ay): 0.57, std(FG_Az): 0.62
std(FG_Bx): 0.43, std(FG_By): 0.60, std(FG_Bz): 0.53
std(FG_Cx): 0.57, std(FG_Cy): 0.43, std(FG_Cz): 0.37
std(FG_Dx): 0.31, std(FG_Dy): 0.56, std(FG_Dz): 0.42
mean(FG_Ax): -386.47, mean(FG_Ay): -595.70, mean(FG_Az): -770.83
mean(FG_Bx): 403.88, mean(FG_By): -456.13, mean(FG_Bz): 403.44
mean(FG_Cx): 391.42, mean(FG_Cy): -326.69, mean(FG_Cz): -230.77
mean(FG_Dx): -254.46, mean(FG_Dy): 487.84, mean(FG_Dz): -333.79
Mean of final values (for static runs only - disregard for dynamic runs):
- Pos. estmted: [ -0.73, 3.74, 0.52 ] - Wilson
- Pos. estmted: [ -1.11, 3.78, 0.16 ] - LSQ Opt.
- Pos. actual: [ -1.00, 3.84, 0.42 ]
- Mom. estmted: [ -23.19, -42.29, -437.37 ] - Wilson
- Mom. estmted: [ -8.19, -40.40, -438.09 ] - LSQ Opt.
- Mom. actual: [ 0.00, 0.00, -438.44 ]
Standard deviation of optimized solution: [ 0.0028, 0.0014, 0.0012 ] m
TiltMeter Mean Pitch: -1.08757549 and Roll: 1.09065730
LSQ Moment Pitch: 0.14509987 and Roll: -0.49207047
```

Run
#6



```
***** RUN 6 *****
std(FG_Ax): 0.62, std(FG_Ay): 0.72, std(FG_Az): 0.96
std(FG_Bx): 0.71, std(FG_By): 0.57, std(FG_Bz): 0.68
std(FG_Cx): 0.68, std(FG_Cy): 0.57, std(FG_Cz): 0.45
std(FG_Dx): 0.51, std(FG_Dy): 0.77, std(FG_Dz): 0.57
mean(FG_Ax): -301.81, mean(FG_Ay): -431.28, mean(FG_Az): -536.10
mean(FG_Bx): 333.41, mean(FG_By): -317.37, mean(FG_Bz): 314.59
mean(FG_Cx): 292.35, mean(FG_Cy): -238.31, mean(FG_Cz): -185.68
mean(FG_Dx): -231.47, mean(FG_Dy): 394.73, mean(FG_Dz): -282.00
Mean of final values (for static runs only - disregard for dynamic runs):
- Pos. estmted: [ -1.62, 3.91, 0.46 ] - Wilson
- Pos. estmted: [ -1.95, 3.80, 0.37 ] - LSQ Opt.
- Pos. actual: [ -2.00, 3.84, 0.42 ]
- Mom. estmted: [ 8.98, -45.16, -434.18 ] - Wilson
- Mom. estmted: [ 0.17, 4.49, -436.59 ] - LSQ Opt.
- Mom. actual: [ 0.00, 0.00, -434.95 ]
Standard deviation of optimized solution: [ 0.0051, 0.0031, 0.0035 ] m
TiltMeter Mean Pitch: 0.05301905 and Roll: 0.79242825
LSQ Moment Pitch: 0.25623902 and Roll: -0.49931217
```

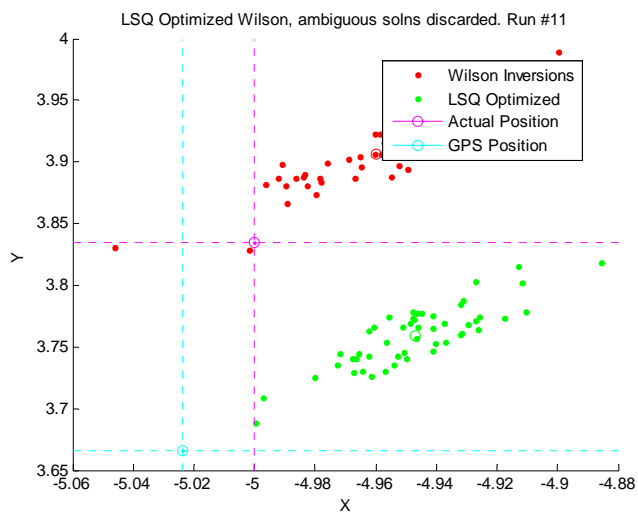


```

mean(FG_Bx): 158.69, mean(FG_By): -148.31, mean(FG_Bz): 150.14
mean(FG_Cx): 133.58, mean(FG_Cy): -124.24, mean(FG_Cz): -95.96
mean(FG_Dx): -124.81, mean(FG_Dy): 192.93, mean(FG_Dz): -164.93
Mean of final values (for static runs only - disregard for dynamic runs):
- Pos. estmtd: [ -3.82, 4.00, 0.33 ] - Wilson
- Pos. estmtd: [ -3.94, 3.77, 0.35 ] - LSQ Opt.
- Pos. actual: [ -4.00, 3.84, 0.42 ]
- Mom. estmtd: [ 34.14, -41.41, -429.38 ] - Wilson
- Mom. estmtd: [ 0.20, 4.26, -432.72 ] - LSQ Opt.
- Mom. actual: [ 0.00, 0.00, -431.17 ]
Standard deviation of optimized solution: [ 0.0145, 0.0143, 0.0051 ] m
TiltMeter Mean Pitch: -0.09530153 and Roll: 0.79107408
LSQ Moment Pitch: 0.52177980 and Roll: -0.49898412

```

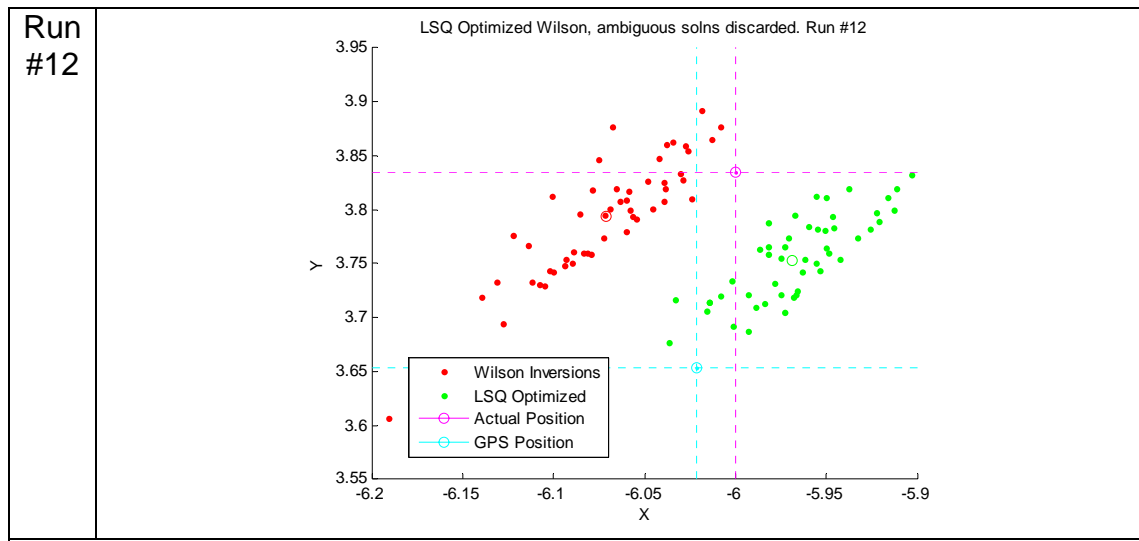
Run
#11



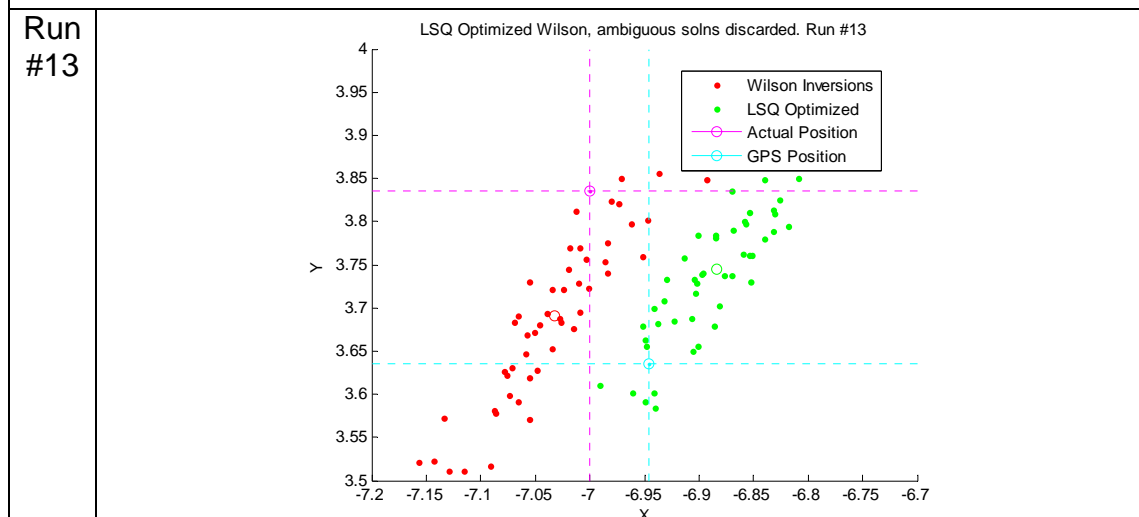
```

***** RUN 11 *****
std(FG_Ax): 0.63, std(FG_Ay): 0.71, std(FG_Az): 0.67
std(FG_Bx): 0.62, std(FG_By): 0.71, std(FG_Bz): 0.72
std(FG_Cx): 0.66, std(FG_Cy): 0.58, std(FG_Cz): 0.47
std(FG_Dx): 0.47, std(FG_Dy): 0.70, std(FG_Dz): 0.55
mean(FG_Ax): -97.55, mean(FG_Ay): -126.97, mean(FG_Az): -125.67
mean(FG_Bx): 110.25, mean(FG_By): -99.07, mean(FG_Bz): 98.97
mean(FG_Cx): 88.21, mean(FG_Cy): -86.57, mean(FG_Cz): -71.26
mean(FG_Dx): -92.48, mean(FG_Dy): 125.80, mean(FG_Dz): -116.09
Mean of final values (for static runs only - disregard for dynamic runs):
- Pos. estmtd: [ -4.96, 3.91, 0.31 ] - Wilson
- Pos. estmtd: [ -4.95, 3.76, 0.29 ] - LSQ Opt.
- Pos. actual: [ -5.00, 3.84, 0.42 ]
- Mom. estmtd: [ 34.42, -29.23, -429.75 ] - Wilson
- Mom. estmtd: [ -0.22, 1.64, -432.15 ] - LSQ Opt.
- Mom. actual: [ 0.00, 0.00, -430.25 ]
Standard deviation of optimized solution: [ 0.0214, 0.0252, 0.0065 ] m
TiltMeter Mean Pitch: -0.38435683 and Roll: 0.77219476
LSQ Moment Pitch: 0.65588787 and Roll: -0.49844664

```



```
***** RUN 12 *****
std(FG_Ax):      0.68, std(FG_Ay):      0.74, std(FG_Az):      0.76
std(FG_Bx):      0.61, std(FG_By):      0.63, std(FG_Bz):      0.74
std(FG_Cx):      0.76, std(FG_Cy):      0.63, std(FG_Cz):      0.56
std(FG_Dx):      0.55, std(FG_Dy):      0.62, std(FG_Dz):      0.55
mean(FG_Ax):     -67.62, mean(FG_Ay):     -83.05, mean(FG_Az):     -82.05
mean(FG_Bx):      75.92, mean(FG_By):     -66.32, mean(FG_Bz):      68.38
mean(FG_Cx):      61.06, mean(FG_Cy):     -59.99, mean(FG_Cz):     -51.72
mean(FG_Dx):     -66.68, mean(FG_Dy):      84.94, mean(FG_Dz):     -79.41
Mean of final values (for static runs only - disregard for dynamic runs):
- Pos. estmted: [      -6.07,      3.79,      0.27 ] - Wilson
- Pos. estmted: [     -5.97,      3.75,      0.29 ] - LSQ Opt.
- Pos. actual:   [     -6.00,      3.84,      0.42 ]
- Mom. estmted: [     38.42,     -19.21,     -429.42 ] - Wilson
- Mom. estmted: [     -0.34,      5.83,     -431.65 ] - LSQ Opt.
- Mom. actual:   [      0.00,      0.00,     -429.78 ]
Standard deviation of optimized solution: [      0.0352,      0.0455,      0.0127
TiltMeter Mean Pitch: -0.39379282 and Roll:  0.69820285
LSQ Moment      Pitch:  0.79211339 and Roll: -0.49800533
```



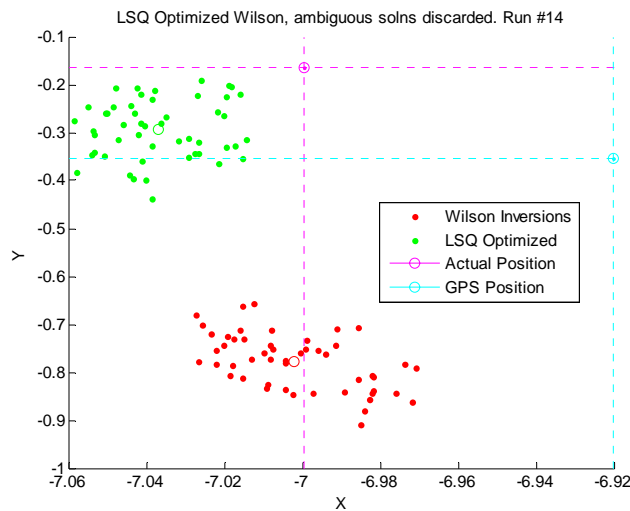
```
***** RUN 13 *****  
std(FG_Ax): 0.52, std(FG_Ay): 0.61, std(FG_Az): 0.59  
std(FG_Bx): 0.55, std(FG_By): 0.58, std(FG_Bz): 0.62  
std(FG_Cx): 0.56, std(FG_Cy): 0.55, std(FG_Cz): 0.41  
std(FG_Dx): 0.34, std(FG_Dy): 0.63, std(FG_Dz): 0.48  
mean(FG_Ax): -50.48, mean(FG_Ay): -57.58, mean(FG_Az): -58.53
```

```

mean(FG_Bx):      56.15, mean(FG_By):     -46.58, mean(FG_Bz):      50.47
mean(FG_Cx):      45.21, mean(FG_Cy):     -43.24, mean(FG_Cz):     -40.06
mean(FG_Dx):     -51.26, mean(FG_Dy):     61.25, mean(FG_Dz):     -56.42
Mean of final values (for static runs only - disregard for dynamic runs):
- Pos. estmtd: [    -7.03,      3.69,      0.25 ] - Wilson
- Pos. estmtd: [    -6.88,      3.74,      0.27 ] - LSQ Opt.
- Pos. actual: [    -7.00,      3.84,      0.42 ]
- Mom. estmtd: [    38.00,     -6.10,   -429.77 ] - Wilson
- Mom. estmtd: [    -0.62,     12.83,   -431.54 ] - LSQ Opt.
- Mom. actual: [     0.00,      0.00,   -430.17 ]
Standard deviation of optimized solution: [    0.0482,     0.0809,     0.0222 ] m
TiltMeter Mean Pitch: -0.38731520 and Roll:  0.39351838
LSQ Moment      Pitch:  0.91357959 and Roll: -0.49695624

```

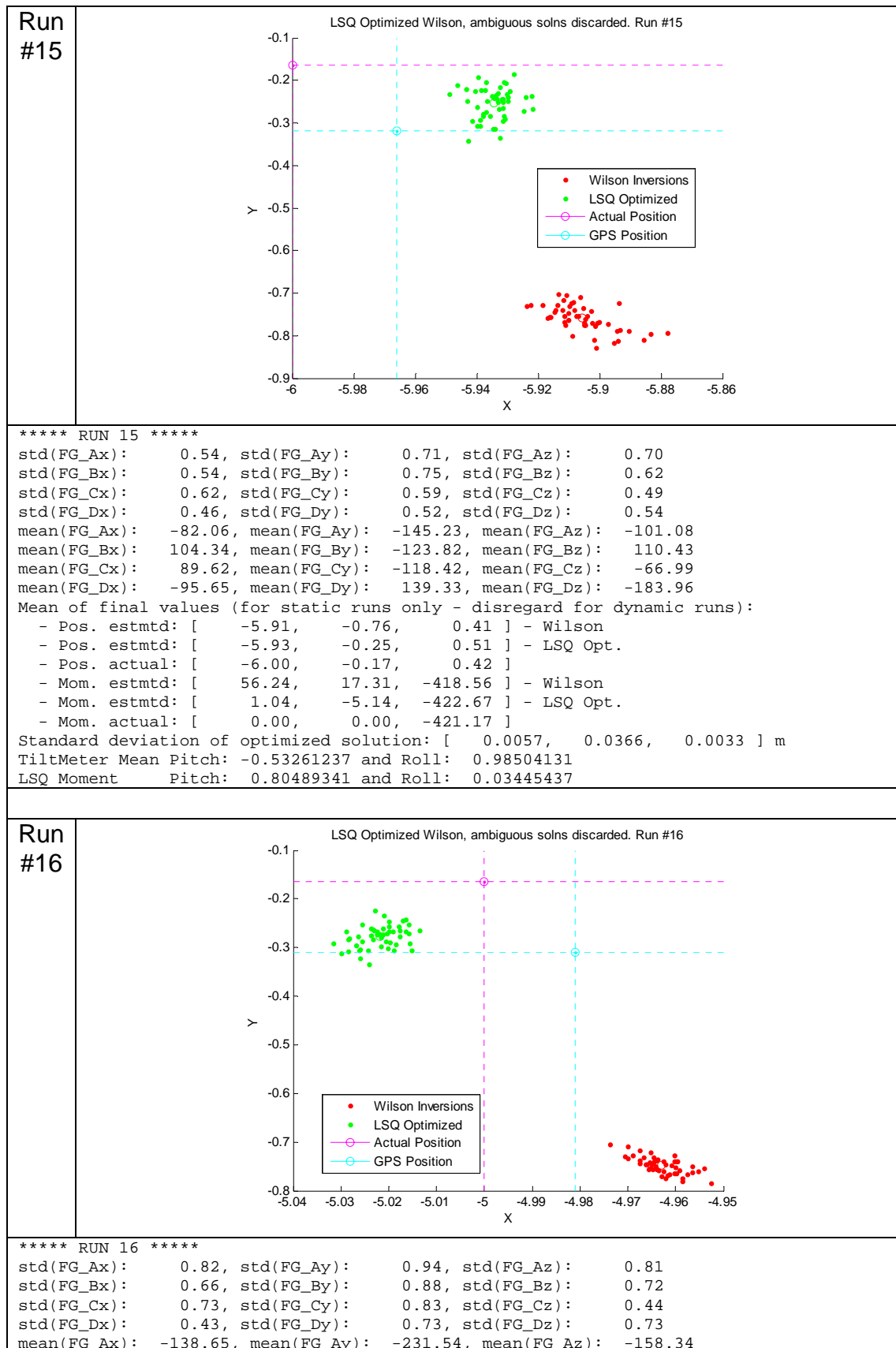
Run
#14



```

***** RUN 14 *****
std(FG_Ax):      0.57, std(FG_Ay):      0.65, std(FG_Az):      0.77
std(FG_Bx):      0.55, std(FG_By):      0.60, std(FG_Bz):      0.77
std(FG_Cx):      0.69, std(FG_Cy):      0.56, std(FG_Cz):      0.48
std(FG_Dx):      0.49, std(FG_Dy):      0.59, std(FG_Dz):      0.45
mean(FG_Ax):     -50.91, mean(FG_Ay):    -85.33, mean(FG_Az):    -63.76
mean(FG_Bx):      62.49, mean(FG_By):    -73.31, mean(FG_Bz):     68.24
mean(FG_Cx):      57.12, mean(FG_Cy):    -70.99, mean(FG_Cz):    -43.10
mean(FG_Dx):     -59.09, mean(FG_Dy):     83.24, mean(FG_Dz):   -102.97
Mean of final values (for static runs only - disregard for dynamic runs):
- Pos. estmtd: [    -7.00,     -0.78,      0.35 ] - Wilson
- Pos. estmtd: [    -7.04,     -0.29,      0.52 ] - LSQ Opt.
- Pos. actual: [    -7.00,     -0.17,      0.42 ]
- Mom. estmtd: [    53.82,     19.71,   -418.76 ] - Wilson
- Mom. estmtd: [     0.45,      2.11,   -422.72 ] - LSQ Opt.
- Mom. actual: [     0.00,      0.00,   -425.98 ]
Standard deviation of optimized solution: [    0.0129,     0.0611,     0.0069 ] m
TiltMeter Mean Pitch: -0.48660240 and Roll:  1.34943151
LSQ Moment      Pitch:  0.95487770 and Roll:  0.03977960

```

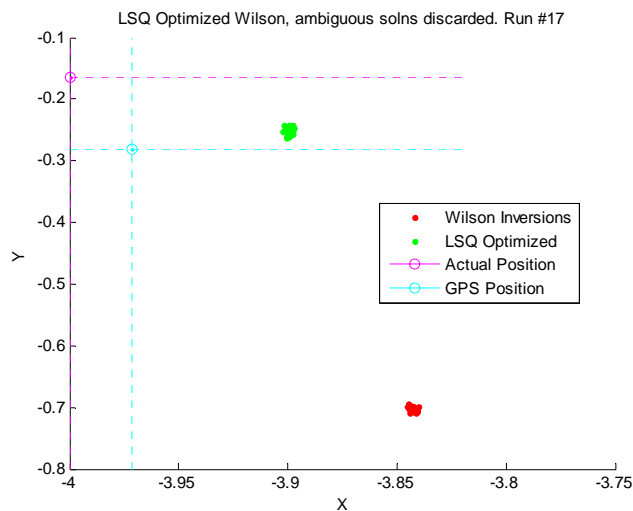


```

mean(FG_Bx): 181.06, mean(FG_By): -192.21, mean(FG_Bz): 175.80
mean(FG_Cx): 136.95, mean(FG_Cy): -184.13, mean(FG_Cz): -109.29
mean(FG_Dx): -165.71, mean(FG_Dy): 229.99, mean(FG_Dz): -313.69
Mean of final values (for static runs only - disregard for dynamic runs):
- Pos. estmtd: [ -4.96, -0.75, 0.43 ] - Wilson
- Pos. estmtd: [ -5.02, -0.28, 0.41 ] - LSQ Opt.
- Pos. actual: [ -5.00, -0.17, 0.42 ]
- Mom. estmtd: [ 52.39, 12.02, -412.71 ] - Wilson
- Mom. estmtd: [ 1.98, -11.24, -416.05 ] - LSQ Opt.
- Mom. actual: [ 0.00, 0.00, -417.53 ]
Standard deviation of optimized solution: [ 0.0043, 0.0228, 0.0026 ] m
TiltMeter Mean Pitch: -0.15312371 and Roll: 0.61573996
LSQ Moment Pitch: 0.69161815 and Roll: 0.03823905

```

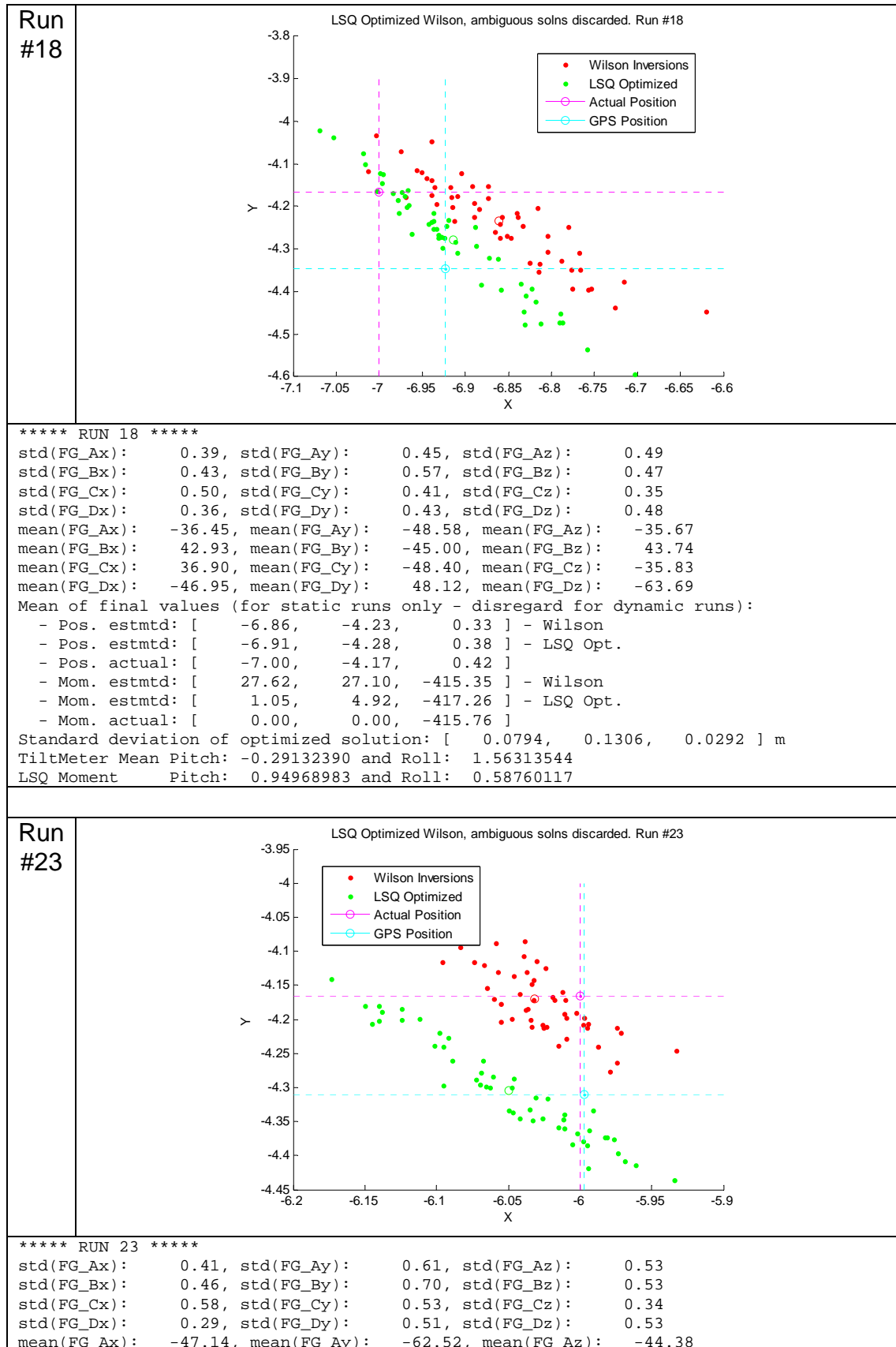
Run
#17



```

***** RUN 17 *****
std(FG_Ax): 0.66, std(FG_Ay): 0.81, std(FG_Az): 0.78
std(FG_Bx): 0.70, std(FG_By): 0.80, std(FG_Bz): 0.86
std(FG_Cx): 0.85, std(FG_Cy): 0.70, std(FG_Cz): 0.48
std(FG_Dx): 0.74, std(FG_Dy): 0.68, std(FG_Dz): 0.60
mean(FG_Ax): -250.56, mean(FG_Ay): -515.68, mean(FG_Az): -321.46
mean(FG_Bx): 365.64, mean(FG_By): -418.77, mean(FG_Bz): 379.98
mean(FG_Cx): 277.41, mean(FG_Cy): -385.36, mean(FG_Cz): -186.47
mean(FG_Dx): -297.38, mean(FG_Dy): 530.18, mean(FG_Dz): -765.80
Mean of final values (for static runs only - disregard for dynamic runs):
- Pos. estmtd: [ -3.84, -0.70, 0.48 ] - Wilson
- Pos. estmtd: [ -3.90, -0.25, 0.44 ] - LSQ Opt.
- Pos. actual: [ -4.00, -0.17, 0.42 ]
- Mom. estmtd: [ 58.62, 28.20, -413.52 ] - Wilson
- Mom. estmtd: [ 0.95, -4.68, -418.58 ] - LSQ Opt.
- Mom. actual: [ 0.00, 0.00, -417.06 ]
Standard deviation of optimized solution: [ 0.0010, 0.0052, 0.0008 ] m
TiltMeter Mean Pitch: -0.35533584 and Roll: 0.90688022
LSQ Moment Pitch: 0.53393381 and Roll: 0.03461899

```

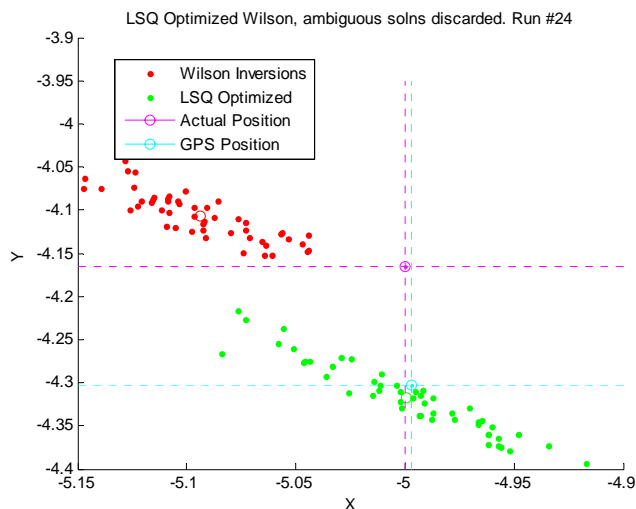


```

mean(FG_Bx):      56.35, mean(FG_By):     -58.34, mean(FG_Bz):      56.68
mean(FG_Cx):      46.93, mean(FG_Cy):     -63.73, mean(FG_Cz):     -46.90
mean(FG_Dx):     -63.10, mean(FG_Dy):     61.85, mean(FG_Dz):     -85.76
Mean of final values (for static runs only - disregard for dynamic runs):
- Pos. estmtd: [   -6.03,     -4.17,      0.36 ] - Wilson
- Pos. estmtd: [   -6.05,     -4.30,      0.39 ] - LSQ Opt.
- Pos. actual: [   -6.00,     -4.17,      0.42 ]
- Mom. estmtd: [   28.50,     25.84,   -413.30 ] - Wilson
- Mom. estmtd: [    0.63,      2.92,   -415.11 ] - LSQ Opt.
- Mom. actual: [    0.00,      0.00,   -418.49 ]
Standard deviation of optimized solution: [    0.0578,     0.0748,     0.0214 ] m
TiltMeter Mean Pitch: -0.28729316 and Roll:  1.50858561
LSQ Moment      Pitch:  0.83464587 and Roll:  0.59394028

```

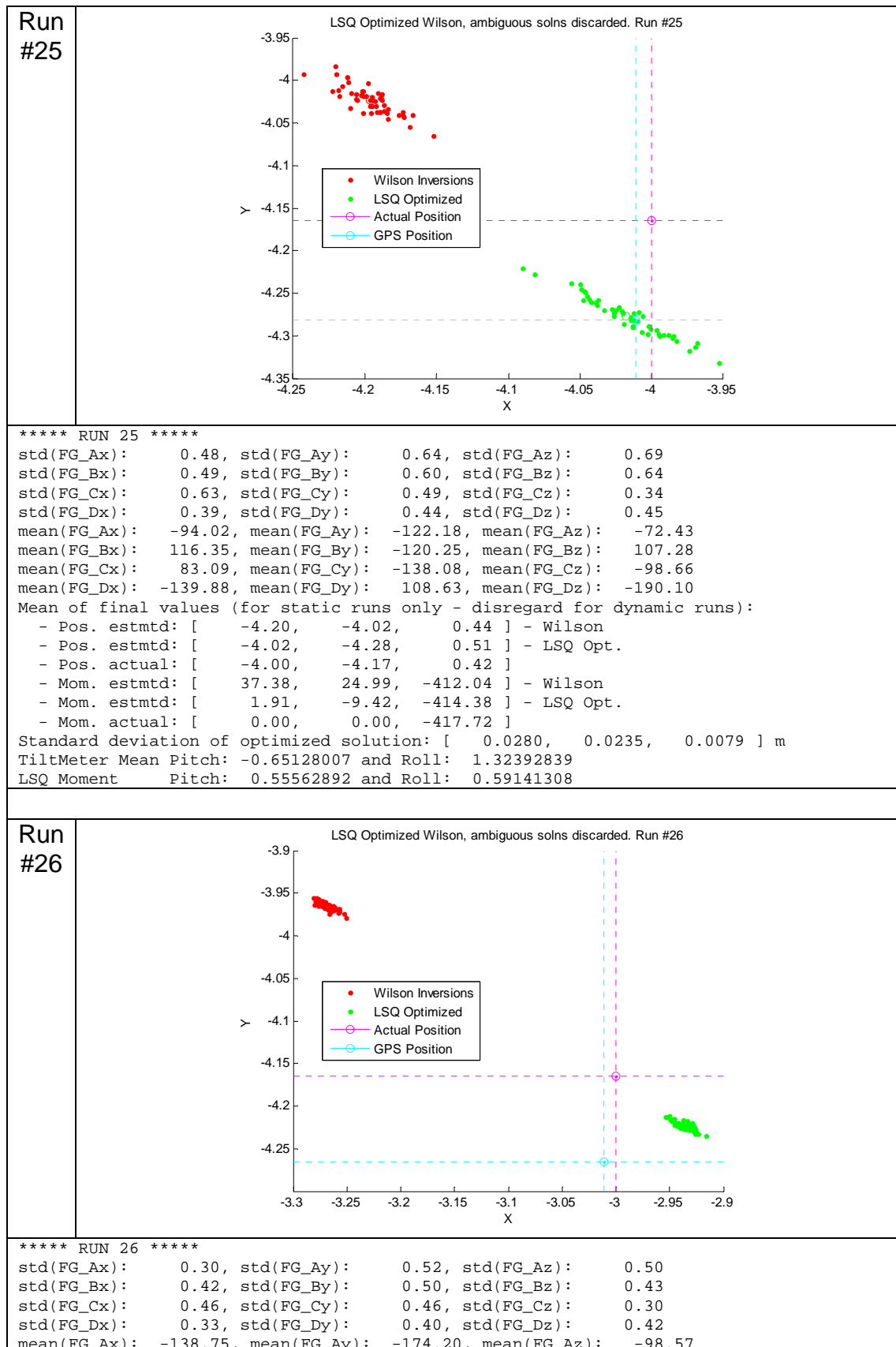
Run
#24



```

***** RUN 24 *****
std(FG_Ax):      0.49, std(FG_Ay):      0.73, std(FG_Az):      0.69
std(FG_Bx):      0.52, std(FG_By):      0.65, std(FG_Bz):      0.65
std(FG_Cx):      0.65, std(FG_Cy):      0.55, std(FG_Cz):      0.35
std(FG_Dx):      0.37, std(FG_Dy):      0.48, std(FG_Dz):      0.54
mean(FG_Ax):     -65.30, mean(FG_Ay):    -91.88, mean(FG_Az):     -51.57
mean(FG_Bx):      79.38, mean(FG_By):    -89.49, mean(FG_Bz):      71.85
mean(FG_Cx):      57.20, mean(FG_Cy):    -98.51, mean(FG_Cz):     -65.16
mean(FG_Dx):     -91.21, mean(FG_Dy):     74.85, mean(FG_Dz):    -134.20
Mean of final values (for static runs only - disregard for dynamic runs):
- Pos. estmtd: [   -5.09,     -4.11,      0.44 ] - Wilson
- Pos. estmtd: [   -5.00,     -4.32,      0.61 ] - LSQ Opt.
- Pos. actual: [   -5.00,     -4.17,      0.42 ]
- Mom. estmtd: [   42.71,     24.64,   -412.20 ] - Wilson
- Mom. estmtd: [    1.87,     -9.24,   -415.05 ] - LSQ Opt.
- Mom. actual: [    0.00,      0.00,   -418.42 ]
Standard deviation of optimized solution: [    0.0385,     0.0414,     0.0101 ] m
TiltMeter Mean Pitch: -1.06832636 and Roll:  1.56391000
LSQ Moment      Pitch:  0.68996432 and Roll:  0.59576721

```

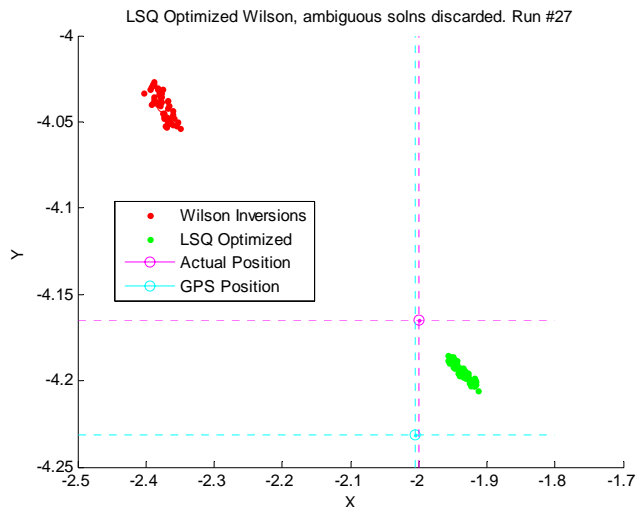


```

mean(FG_Bx): 174.90, mean(FG_By): -177.45, mean(FG_Bz): 161.00
mean(FG_Cx): 120.16, mean(FG_Cy): -213.29, mean(FG_Cz): -155.34
mean(FG_Dx): -222.03, mean(FG_Dy): 151.84, mean(FG_Dz): -288.89
Mean of final values (for static runs only - disregard for dynamic runs):
- Pos. estmtd: [ -3.27, -3.97, 0.44 ] - Wilson
- Pos. estmtd: [ -2.94, -4.22, 0.49 ] - LSQ Opt.
- Pos. actual: [ -3.00, -4.17, 0.42 ]
- Mom. estmtd: [ 38.99, 31.96, -414.11 ] - Wilson
- Mom. estmtd: [ 1.75, -8.61, -417.08 ] - LSQ Opt.
- Mom. actual: [ 0.00, 0.00, -415.70 ]
Standard deviation of optimized solution: [ 0.0085, 0.0053, 0.0038 ] m
TiltMeter Mean Pitch: -0.55888820 and Roll: 1.40171229
LSQ Moment Pitch: 0.40335081 and Roll: 0.58018723

```

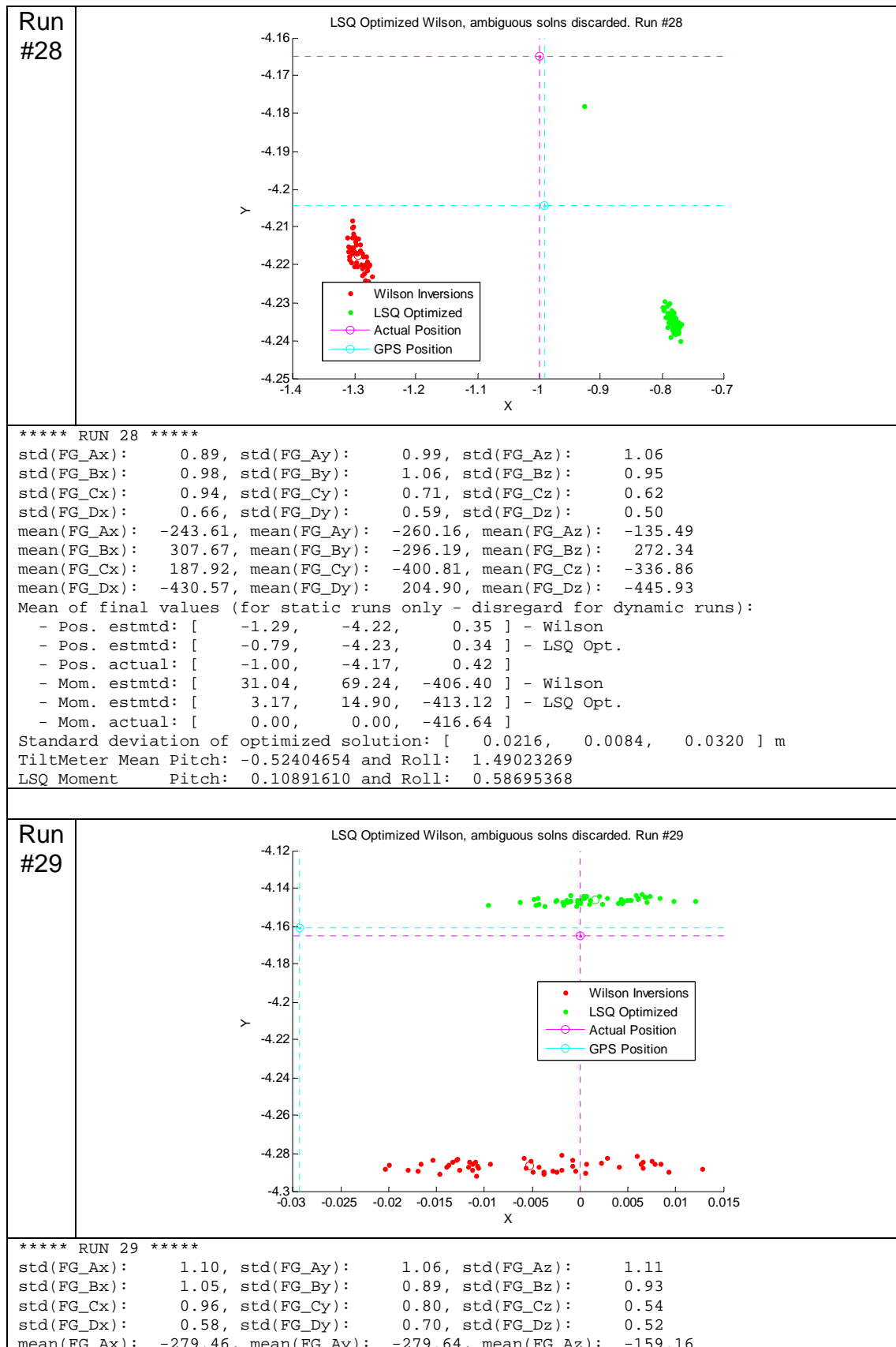
Run
#27



```

***** RUN 27 *****
std(FG_Ax): 0.82, std(FG_Ay): 1.11, std(FG_Az): 1.09
std(FG_Bx): 0.93, std(FG_By): 0.86, std(FG_Bz): 1.05
std(FG_Cx): 0.92, std(FG_Cy): 0.69, std(FG_Cz): 0.60
std(FG_Dx): 0.58, std(FG_Dy): 0.65, std(FG_Dz): 0.47
mean(FG_Ax): -193.23, mean(FG_Ay): -226.52, mean(FG_Az): -115.95
mean(FG_Bx): 245.88, mean(FG_By): -243.86, mean(FG_Bz): 213.23
mean(FG_Cx): 150.36, mean(FG_Cy): -309.45, mean(FG_Cz): -235.77
mean(FG_Dx): -330.18, mean(FG_Dy): 178.25, mean(FG_Dz): -391.05
Mean of final values (for static runs only - disregard for dynamic runs):
- Pos. estmtd: [ -2.38, -4.04, 0.41 ] - Wilson
- Pos. estmtd: [ -1.93, -4.20, 0.56 ] - LSQ Opt.
- Pos. actual: [ -2.00, -4.17, 0.42 ]
- Mom. estmtd: [ 46.64, 46.80, -412.06 ] - Wilson
- Mom. estmtd: [ 3.35, -16.53, -416.98 ] - LSQ Opt.
- Mom. actual: [ 0.00, 0.00, -415.53 ]
Standard deviation of optimized solution: [ 0.0139, 0.0057, 0.0060 ] m
TiltMeter Mean Pitch: -0.76205916 and Roll: 1.50015120
LSQ Moment Pitch: 0.26563896 and Roll: 0.57604974

```

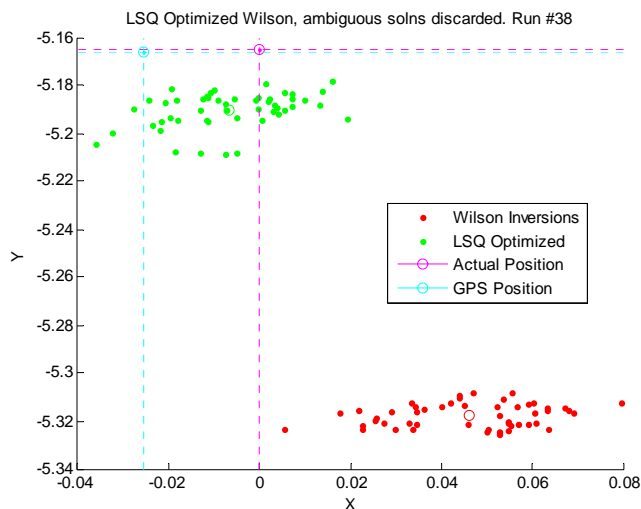


```

mean(FG_Bx): 341.34, mean(FG_By): -334.12, mean(FG_Bz): 325.91
mean(FG_Cx): 238.11, mean(FG_Cy): -470.51, mean(FG_Cz): -436.00
mean(FG_Dx): -479.22, mean(FG_Dy): 233.24, mean(FG_Dz): -444.92
Mean of final values (for static runs only - disregard for dynamic runs):
- Pos. estmtd: [ -0.01, -4.29, 0.35 ] - Wilson
- Pos. estmtd: [ 0.00, -4.15, 0.34 ] - LSQ Opt.
- Pos. actual: [ 0.00, -4.17, 0.42 ]
- Mom. estmtd: [ -10.49, 71.53, -412.97 ] - Wilson
- Mom. estmtd: [ 1.68, 8.86, -419.15 ] - LSQ Opt.
- Mom. actual: [ 0.00, 0.00, -417.80 ]
Standard deviation of optimized solution: [ 0.0045, 0.0016, 0.0069 ] m
TiltMeter Mean Pitch: -0.06061101 and Roll: 1.43744938
LSQ Moment Pitch: -0.00022079 and Roll: 0.56649650

```

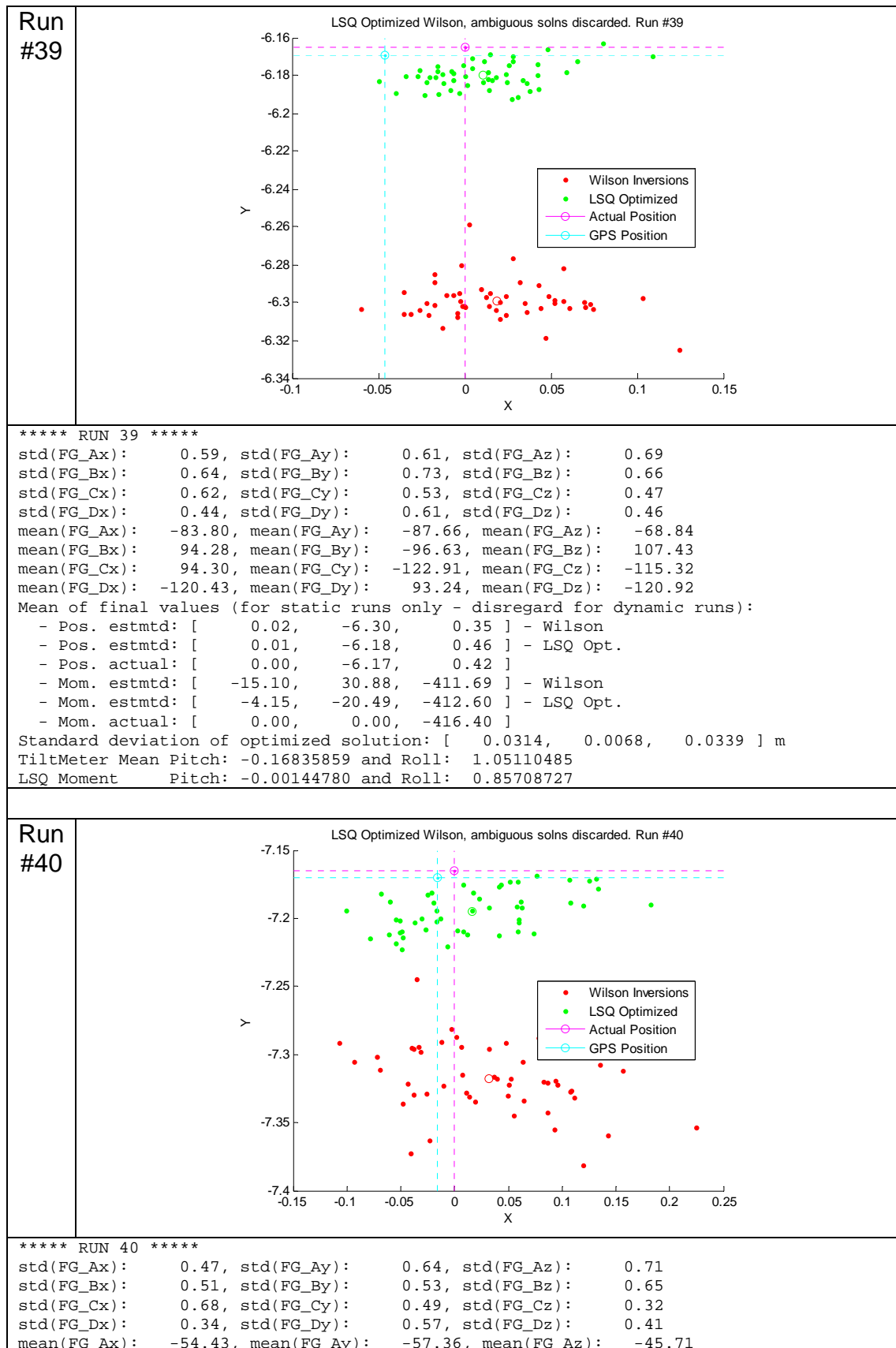
Run
#38



```

***** RUN 38 *****
std(FG_Ax): 0.57, std(FG_Ay): 0.86, std(FG_Az): 0.68
std(FG_Bx): 0.58, std(FG_By): 0.86, std(FG_Bz): 0.68
std(FG_Cx): 0.70, std(FG_Cy): 0.82, std(FG_Cz): 0.38
std(FG_Dx): 0.32, std(FG_Dy): 0.55, std(FG_Dz): 0.67
mean(FG_Ax): -138.92, mean(FG_Ay): -145.29, mean(FG_Az): -101.45
mean(FG_Bx): 160.54, mean(FG_By): -165.17, mean(FG_Bz): 174.75
mean(FG_Cx): 145.99, mean(FG_Cy): -218.68, mean(FG_Cz): -201.29
mean(FG_Dx): -214.00, mean(FG_Dy): 142.17, mean(FG_Dz): -212.61
Mean of final values (for static runs only - disregard for dynamic runs):
- Pos. estmtd: [ 0.05, -5.32, 0.35 ] - Wilson
- Pos. estmtd: [ -0.01, -5.19, 0.44 ] - LSQ Opt.
- Pos. actual: [ 0.00, -5.17, 0.42 ]
- Mom. estmtd: [ -18.52, 44.07, -409.30 ] - Wilson
- Mom. estmtd: [ -4.02, -14.89, -411.58 ] - LSQ Opt.
- Mom. actual: [ 0.00, 0.00, -415.32 ]
Standard deviation of optimized solution: [ 0.0129, 0.0075, 0.1103 ] m
TiltMeter Mean Pitch: 0.05566473 and Roll: 1.01273386
LSQ Moment Pitch: 0.00092103 and Roll: 0.72150854

```

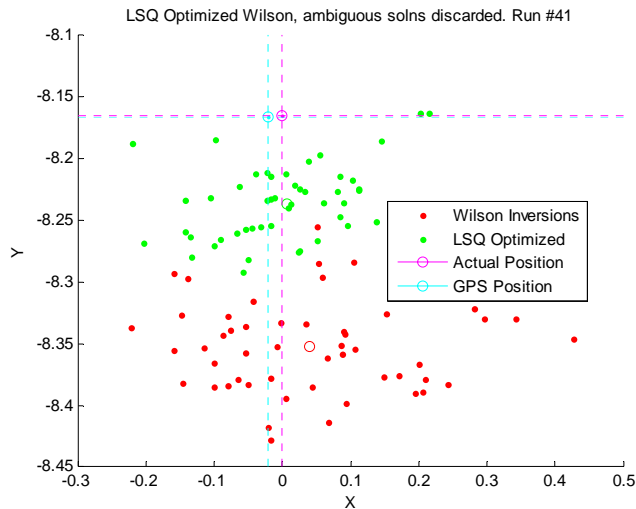


```

mean(FG_Bx):      60.20, mean(FG_By):     -62.17, mean(FG_Bz):      67.23
mean(FG_Cx):      60.27, mean(FG_Cy):     -76.60, mean(FG_Cz):     -71.60
mean(FG_Dx):     -74.34, mean(FG_Dy):     59.79, mean(FG_Dz):     -75.34
Mean of final values (for static runs only - disregard for dynamic runs):
- Pos. estmtd: [      0.03,     -7.32,      0.32 ] - Wilson
- Pos. estmtd: [      0.02,     -7.19,      0.42 ] - LSQ Opt.
- Pos. actual: [      0.00,     -7.17,      0.42 ]
- Mom. estmtd: [     -15.95,     30.13,   -412.44 ] - Wilson
- Mom. estmtd: [     -5.36,    -13.30,   -413.02 ] - LSQ Opt.
- Mom. actual: [      0.00,      0.00,   -417.22 ]
Standard deviation of optimized solution: [      0.0648,     0.0151,    0.2681 ] m
TiltMeter Mean Pitch: -0.07553846 and Roll:  0.99761025
LSQ Moment      Pitch: -0.00230141 and Roll:  0.99587601

```

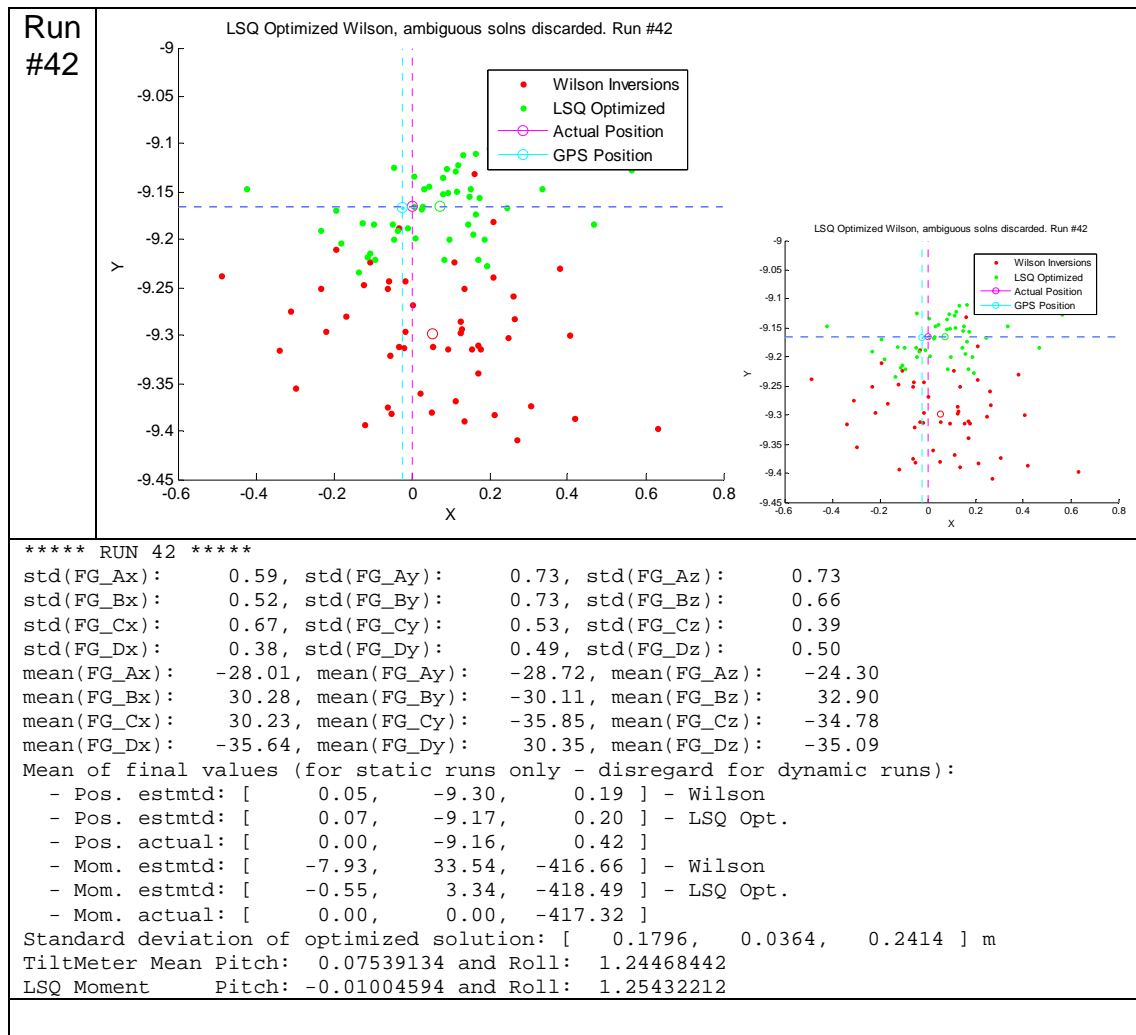
Run
#41



```

***** RUN 41 *****
std(FG_Ax):      0.53, std(FG_Ay):      0.75, std(FG_Az):      0.79
std(FG_Bx):      0.55, std(FG_By):      0.72, std(FG_Bz):      0.75
std(FG_Cx):      0.71, std(FG_Cy):      0.61, std(FG_Cz):      0.42
std(FG_Dx):      0.43, std(FG_Dy):      0.59, std(FG_Dz):      0.60
mean(FG_Ax):     -38.32, mean(FG_Ay):     -39.73, mean(FG_Az):     -29.78
mean(FG_Bx):      42.04, mean(FG_By):     -42.67, mean(FG_Bz):     42.36
mean(FG_Cx):     38.06, mean(FG_Cy):     -51.26, mean(FG_Cz):     -48.64
mean(FG_Dx):     -50.55, mean(FG_Dy):     37.92, mean(FG_Dz):     -50.11
Mean of final values (for static runs only - disregard for dynamic runs):
- Pos. estmtd: [      0.04,     -8.35,      0.26 ] - Wilson
- Pos. estmtd: [      0.01,     -8.24,      0.22 ] - LSQ Opt.
- Pos. actual: [      0.00,     -8.16,      0.42 ]
- Mom. estmtd: [     -13.40,     40.45,   -411.63 ] - Wilson
- Mom. estmtd: [     -2.90,     12.12,   -413.62 ] - LSQ Opt.
- Mom. actual: [      0.00,      0.00,   -417.37 ]
Standard deviation of optimized solution: [      0.1028,     0.0310,    0.1969 ] m
TiltMeter Mean Pitch:  0.43034425 and Roll:  1.15274331
LSQ Moment      Pitch: -0.00089039 and Roll:  1.13974792

```



6. Summary of Errors for each run

Below is a list of the positions, distances, errors and standard deviations for each run.

The error is the position of the EM63 subtracted from the mean position estimated from the associated inversion technique. The standard deviation (STD) is the standard deviation about the estimated mean position.

Error summary

```
Run # 3 (Pos A): GPS Position: [ -0.0248, 2.8265, 0.3887 ] m
Run # 3 (Pos A): Distance: 2.8532 m
Run # 3 (Pos A): Wilson Error: [ -0.0389, -0.1890, 0.1920 ] m
Run # 3 (Pos A): Wilson LSQ Error: [ -0.0202, -0.0523, 0.0456 ] m
Run # 3 (Pos A): Wilson STD: [ 0.0004, 0.0001, 0.0004 ] m
Run # 3 (Pos A): Wilson LSQ STD: [ 0.0007, 0.0003, 0.0003 ] m

Run # 5 (Pos B): GPS Position: [ -1.0362, 3.7898, 0.3480 ] m
Run # 5 (Pos B): Distance: 3.9443 m
Run # 5 (Pos B): Wilson Error: [ 0.3027, -0.0482, 0.1691 ] m
Run # 5 (Pos B): Wilson LSQ Error: [ -0.0776, -0.0127, -0.1884 ] m
Run # 5 (Pos B): Wilson STD: [ 0.0024, 0.0009, 0.0032 ] m
Run # 5 (Pos B): Wilson LSQ STD: [ 0.0028, 0.0014, 0.0012 ] m

Run # 6 (Pos C): GPS Position: [ -2.0288, 3.7458, 0.3880 ] m
Run # 6 (Pos C): Distance: 4.2776 m
Run # 6 (Pos C): Wilson Error: [ 0.4106, 0.1660, 0.0693 ] m
Run # 6 (Pos C): Wilson LSQ Error: [ 0.0785, 0.0546, -0.0157 ] m
```

```

Run # 6 (Pos C):      Wilson STD: [ 0.0043,  0.0019,  0.0057 ] m
Run # 6 (Pos C):      Wilson LSQ STD: [ 0.0051,  0.0031,  0.0035 ] m

Run # 7 (Pos D):      GPS Position: [ -3.0241,  3.7278,  0.3869 ] m
Run # 7 (Pos D):      Distance: 4.8158 m
Run # 7 (Pos D):      Wilson Error: [ 0.3334,  0.2863,  0.0074 ] m
Run # 7 (Pos D):      Wilson LSQ Error: [ 0.0629,  0.0558, -0.1096 ] m
Run # 7 (Pos D):      Wilson STD: [ 0.0088,  0.0060,  0.0142 ] m
Run # 7 (Pos D):      Wilson LSQ STD: [ 0.0084,  0.0067,  0.0022 ] m

Run #10 (Pos E):      GPS Position: [ -4.0285,  3.6970,  0.3960 ] m
Run #10 (Pos E):      Distance: 5.4821 m
Run #10 (Pos E):      Wilson Error: [ 0.2037,  0.3019, -0.0613 ] m
Run #10 (Pos E):      Wilson LSQ Error: [ 0.0874,  0.0719, -0.0411 ] m
Run #10 (Pos E):      Wilson STD: [ 0.0173,  0.0142,  0.0250 ] m
Run #10 (Pos E):      Wilson LSQ STD: [ 0.0145,  0.0143,  0.0051 ] m

Run #11 (Pos F):      GPS Position: [ -5.0239,  3.6660,  0.3980 ] m
Run #11 (Pos F):      Distance: 6.2320 m
Run #11 (Pos F):      Wilson Error: [ 0.0643,  0.2406, -0.0879 ] m
Run #11 (Pos F):      Wilson LSQ Error: [ 0.0770,  0.0934, -0.1107 ] m
Run #11 (Pos F):      Wilson STD: [ 0.0261,  0.0291,  0.0415 ] m
Run #11 (Pos F):      Wilson LSQ STD: [ 0.0214,  0.0252,  0.0065 ] m

Run #12 (Pos G):      GPS Position: [ -6.0211,  3.6531,  0.3879 ] m
Run #12 (Pos G):      Distance: 7.0533 m
Run #12 (Pos G):      Wilson Error: [ -0.0501,  0.1405, -0.1200 ] m
Run #12 (Pos G):      Wilson LSQ Error: [ 0.0524,  0.0996, -0.1028 ] m
Run #12 (Pos G):      Wilson STD: [ 0.0372,  0.0540,  0.0852 ] m
Run #12 (Pos G):      Wilson LSQ STD: [ 0.0352,  0.0455,  0.0127 ] m

Run #13 (Pos G'):      GPS Position: [ -6.9454,  3.6353,  0.3424 ] m
Run #13 (Pos G'):      Distance: 7.8467 m
Run #13 (Pos G'):      Wilson Error: [ -0.0874,  0.0554, -0.0955 ] m
Run #13 (Pos G'):      Wilson LSQ Error: [ 0.0616,  0.1093, -0.0674 ] m
Run #13 (Pos G'):      Wilson STD: [ 0.0573,  0.0996,  0.1305 ] m
Run #13 (Pos G'):      Wilson LSQ STD: [ 0.0482,  0.0809,  0.0222 ] m

Run #14 (Pos L):      GPS Position: [ -6.9206, -0.3533,  0.4675 ] m
Run #14 (Pos L):      Distance: 6.9454 m
Run #14 (Pos L):      Wilson Error: [ -0.0817, -0.4234, -0.1169 ] m
Run #14 (Pos L):      Wilson LSQ Error: [ -0.1165,  0.0601,  0.0536 ] m
Run #14 (Pos L):      Wilson STD: [ 0.0161,  0.0572,  0.0587 ] m
Run #14 (Pos L):      Wilson LSQ STD: [ 0.0129,  0.0611,  0.0069 ] m

Run #15 (Pos K):      GPS Position: [ -5.9662, -0.3198,  0.4597 ] m
Run #15 (Pos K):      Distance: 5.9924 m
Run #15 (Pos K):      Wilson Error: [ 0.0603, -0.4393, -0.0520 ] m
Run #15 (Pos K):      Wilson LSQ Error: [ 0.0314,  0.0658,  0.0454 ] m
Run #15 (Pos K):      Wilson STD: [ 0.0096,  0.0307,  0.0352 ] m
Run #15 (Pos K):      Wilson LSQ STD: [ 0.0057,  0.0366,  0.0033 ] m

Run #16 (Pos J):      GPS Position: [ -4.9810, -0.3088,  0.4309 ] m
Run #16 (Pos J):      Distance: 5.0091 m
Run #16 (Pos J):      Wilson Error: [ 0.0180, -0.4389, -0.0002 ] m
Run #16 (Pos J):      Wilson LSQ Error: [ -0.0410,  0.0311, -0.0204 ] m
Run #16 (Pos J):      Wilson STD: [ 0.0044,  0.0174,  0.0165 ] m
Run #16 (Pos J):      Wilson LSQ STD: [ 0.0043,  0.0228,  0.0026 ] m

Run #17 (Pos I):      GPS Position: [ -3.9716, -0.2820,  0.4429 ] m
Run #17 (Pos I):      Distance: 4.0062 m
Run #17 (Pos I):      Wilson Error: [ 0.1285, -0.4203,  0.0354 ] m
Run #17 (Pos I):      Wilson LSQ Error: [ 0.0723,  0.0291, -0.0016 ] m
Run #17 (Pos I):      Wilson STD: [ 0.0013,  0.0036,  0.0046 ] m
Run #17 (Pos I):      Wilson LSQ STD: [ 0.0010,  0.0052,  0.0008 ] m

Run #18 (Pos V):      GPS Position: [ -6.9229, -4.3466,  0.3608 ] m
Run #18 (Pos V):      Distance: 8.1823 m
Run #18 (Pos V):      Wilson Error: [ 0.0620,  0.1127, -0.0341 ] m
Run #18 (Pos V):      Wilson LSQ Error: [ 0.0091,  0.0686,  0.0149 ] m
Run #18 (Pos V):      Wilson STD: [ 0.0808,  0.1004,  0.1037 ] m

```

Run #18 (Pos V): Wilson LSQ STD: [0.0794, 0.1306, 0.0292] m
 Run #23 (Pos U): GPS Position: [-5.9974, -4.3098, 0.3532] m
 Run #23 (Pos U): Distance: 7.3938 m
 Run #23 (Pos U): Wilson Error: [-0.0345, 0.1398, 0.0064] m
 Run #23 (Pos U): Wilson LSQ Error: [-0.0520, 0.0049, 0.0345] m
 Run #23 (Pos U): Wilson STD: [0.0399, 0.0527, 0.0608] m
 Run #23 (Pos U): Wilson LSQ STD: [0.0578, 0.0748, 0.0214] m

 Run #24 (Pos T): GPS Position: [-4.9973, -4.3029, 0.3643] m
 Run #24 (Pos T): Distance: 6.6046 m
 Run #24 (Pos T): Wilson Error: [-0.0967, 0.1963, 0.0768] m
 Run #24 (Pos T): Wilson LSQ Error: [-0.0021, -0.0140, 0.2468] m
 Run #24 (Pos T): Wilson STD: [0.0277, 0.0273, 0.0378] m
 Run #24 (Pos T): Wilson LSQ STD: [0.0385, 0.0414, 0.0101] m

 Run #25 (Pos S): GPS Position: [-4.0110, -4.2818, 0.3954] m
 Run #25 (Pos S): Distance: 5.8803 m
 Run #25 (Pos S): Wilson Error: [-0.1855, 0.2585, 0.0478] m
 Run #25 (Pos S): Wilson LSQ Error: [-0.0071, 0.0050, 0.1143] m
 Run #25 (Pos S): Wilson STD: [0.0166, 0.0165, 0.0179] m
 Run #25 (Pos S): Wilson LSQ STD: [0.0280, 0.0235, 0.0079] m

 Run #26 (Pos R): GPS Position: [-3.0107, -4.2659, 0.3885] m
 Run #26 (Pos R): Distance: 5.2358 m
 Run #26 (Pos R): Wilson Error: [-0.2575, 0.3002, 0.0521] m
 Run #26 (Pos R): Wilson LSQ Error: [0.0748, 0.0428, 0.0993] m
 Run #26 (Pos R): Wilson STD: [0.0072, 0.0051, 0.0097] m
 Run #26 (Pos R): Wilson LSQ STD: [0.0085, 0.0053, 0.0038] m

 Run #27 (Pos Q): GPS Position: [-2.0052, -4.2311, 0.3924] m
 Run #27 (Pos Q): Distance: 4.6986 m
 Run #27 (Pos Q): Wilson Error: [-0.3700, 0.1900, 0.0139] m
 Run #27 (Pos Q): Wilson LSQ Error: [0.0706, 0.0357, 0.1646] m
 Run #27 (Pos Q): Wilson STD: [0.0119, 0.0081, 0.0105] m
 Run #27 (Pos Q): Wilson LSQ STD: [0.0139, 0.0057, 0.0060] m

 Run #28 (Pos P): GPS Position: [-0.9909, -4.2043, 0.3994] m
 Run #28 (Pos P): Distance: 4.3379 m
 Run #28 (Pos P): Wilson Error: [-0.3028, -0.0131, -0.0461] m
 Run #28 (Pos P): Wilson LSQ Error: [0.2052, -0.0294, -0.0632] m
 Run #28 (Pos P): Wilson STD: [0.0110, 0.0038, 0.0107] m
 Run #28 (Pos P): Wilson LSQ STD: [0.0216, 0.0084, 0.0320] m

 Run #29 (Pos N): GPS Position: [-0.0293, -4.1610, 0.4185] m
 Run #29 (Pos N): Distance: 4.1821 m
 Run #29 (Pos N): Wilson Error: [0.0240, -0.1256, -0.0717] m
 Run #29 (Pos N): Wilson LSQ Error: [0.0309, 0.0148, -0.0790] m
 Run #29 (Pos N): Wilson STD: [0.0087, 0.0027, 0.0100] m
 Run #29 (Pos N): Wilson LSQ STD: [0.0045, 0.0016, 0.0069] m

 Run #38 (Pos W): GPS Position: [-0.0255, -5.1661, 0.3953] m
 Run #38 (Pos W): Distance: 5.1813 m
 Run #38 (Pos W): Wilson Error: [0.0715, -0.1515, -0.0410] m
 Run #38 (Pos W): Wilson LSQ Error: [0.0188, -0.0242, 0.0472] m
 Run #38 (Pos W): Wilson STD: [0.0158, 0.0048, 0.0181] m
 Run #38 (Pos W): Wilson LSQ STD: [0.0129, 0.0075, 0.1103] m

 Run #39 (Pos X): GPS Position: [-0.0466, -6.1690, 0.4153] m
 Run #39 (Pos X): Distance: 6.1831 m
 Run #39 (Pos X): Wilson Error: [0.0649, -0.1300, -0.0623] m
 Run #39 (Pos X): Wilson LSQ Error: [0.0570, -0.0110, 0.0469] m
 Run #39 (Pos X): Wilson STD: [0.0380, 0.0104, 0.0344] m
 Run #39 (Pos X): Wilson LSQ STD: [0.0314, 0.0068, 0.0339] m

 Run #40 (Pos Y): GPS Position: [-0.0157, -7.1704, 0.4120] m
 Run #40 (Pos Y): Distance: 7.1822 m
 Run #40 (Pos Y): Wilson Error: [0.0476, -0.1477, -0.0888] m
 Run #40 (Pos Y): Wilson LSQ Error: [0.0323, -0.0244, 0.0094] m
 Run #40 (Pos Y): Wilson STD: [0.0709, 0.0256, 0.0753] m
 Run #40 (Pos Y): Wilson LSQ STD: [0.0648, 0.0151, 0.2681] m

```
Run #41 (Pos Z):      GPS Position: [ -0.0207, -8.1664,  0.3908 ] m
Run #41 (Pos Z):      Distance:  8.1758 m
Run #41 (Pos Z):      Wilson Error: [  0.0602, -0.1863, -0.1292 ] m
Run #41 (Pos Z):      Wilson LSQ Error: [  0.0272, -0.0698, -0.1743 ] m
Run #41 (Pos Z):      Wilson STD: [  0.1435,  0.0366,  0.1487 ] m
Run #41 (Pos Z):      Wilson LSQ STD: [  0.1028,  0.0310,  0.1969 ] m

Run #42 (Pos SS):      GPS Position: [ -0.0248, -9.1664,  0.3887 ] m
Run #42 (Pos SS):      Distance:  9.1747 m
Run #42 (Pos SS):      Wilson Error: [  0.0785, -0.1311, -0.1998 ] m
Run #42 (Pos SS):      Wilson LSQ Error: [  0.0982,  0.0008, -0.1844 ] m
Run #42 (Pos SS):      Wilson STD: [  0.2149,  0.0637,  0.2906 ] m
Run #42 (Pos SS):      Wilson LSQ STD: [  0.1796,  0.0364,  0.2414 ] m
```

APPENDIX B: EVALUATING THE ON-TIME RESPONSE OF A CONDUCTING, PERMEABLE HALF-SPACE

The results presented in this appendix leverage heavily from research conducted by Len Pasion under SERDP project MM-1573. Two steps are required to calculate the on-time response of a conducting, permeable half-space: (1) evaluate the frequency-domain response from a dipole transmitter source at an arbitrary receiver position; and (2) convolve the frequency-domain half-space response with the transmitter waveform. The first step is achieved using the expression given in Equation (1) in the main-text. In this appendix, we describe the method for convolution with the transmitter waveform.

The EM63 waveform consists of an exponential ramp on with a time-constant of 4.3 ms that is shut-off at 33.4 ms. The shut-off is a linear ramp that spans 0.1 ms. For positioning the transmitter using a B-field sensor, the field from about 20 to 33 ms would be utilized, as by that time most conductive effects would have dissipated. On the other hand, a dB/dt sensor would utilize the rapid turn-off of the primary field. Thus, to investigate the B-field response of a conductive/permeable ground we need to convolve the half-space response with the exponential ramp, while for the dB/dt response we need to convolve with a linear-ramp. As the exponential is on for a significant period of time (33.4 ms) relative to the pulse turn-off (0.1 ms), it can be modeled as a step-off response, and we then only have to convolve with the linear-ramp.

The transfer function for an exponential ramp-up can be derived from two transforms in the table of Fourier Transforms provided in Bracewell (1986). Specifically:

$$H(t) \exp\left(-\frac{t}{\tau}\right) \Rightarrow \frac{1-i\omega\tau}{1+(\omega\tau)^2}$$

where \Rightarrow indicates Fourier transformation and $H(t)$ is the Heaviside step function which has Fourier transform:=

$$H(t) \Rightarrow \frac{\delta(\omega)}{2} - \frac{i}{\omega}$$

where $\delta(\omega)$ is the Dirac delta-function. Putting these two Fourier transforms together we find:

$$G(t) = H(t) \left[1 - \exp\left(-\frac{t}{\tau}\right) \right] \Rightarrow G(\omega) = \frac{\delta(\omega)}{2} - \frac{i}{\omega} - \frac{1-i\omega\tau}{1+(\omega\tau)^2}$$

To obtain the half-space response of the field of a vertical dipole to the waveform $G(t)$ we compute:

$$B(\omega) = G(\omega) H_z(\omega)$$

And then calculate the inverse fourier transform of $B(\omega)$,

$$b(t) = \frac{1}{2\pi} \int_{-\infty}^{\infty} G(\omega) H_z(\omega) \exp(i\omega t) d\omega$$

Expanding this equation we find:

$$b(t) = \frac{H_z(0)}{2} - \int_{-\infty}^{\infty} \left(\frac{i}{\omega} + \frac{1-i\omega\tau}{1+(\omega\tau)^2} \right) H_z(\omega) \exp(i\omega t) d\omega$$

The integral can be evaluated using the digital filters of Anderson (1982).

The b-field and dB/dt response to the linear ramp can be obtained from the Fourier transform of the saw-tooth function:

$$r(t) = \begin{cases} 1 + t/\Delta t & \text{for } -\Delta t < t < 0 \\ 1 - t/\Delta t & \text{for } 0 < t < \Delta t \Rightarrow R(\omega) = \text{sinc}^2(\omega\Delta t) \\ 0 & \text{everywhere else} \end{cases}$$

where $\text{sinc}(t) = \sin(t)/t$ is the sinc function. We need to shift the function $r(t)$ by an amount of Δt so that the ramp up starts at 0. The function $r(t - \Delta t)$ has Fourier transform:

$$R(\omega) = \exp(i\omega\Delta t) \text{sinc}^2(\omega\Delta t)$$

Finally, the ramp function starts from 0 and rises to a maximum of 1 at $t = \Delta t$, whereas we want it to start at 1 and decrease to 0. Therefore we Fourier transform the function:

$$f(t) = 1 - r(t + \Delta t)$$

which becomes

$$F(\omega) = \delta(\omega) - \exp(i\omega\Delta t) \text{sinc}^2(\omega\Delta t)$$

The B-field response can be obtained as;

$$b(t) = H_z(0) - \int_{-\infty}^{\infty} \text{sinc}^2(\omega\Delta t) H_z(\omega) \exp[i\omega(t + \Delta t)] d\omega$$

The Fourier integral can be efficiently evaluated at a number of discrete times by using the trapezoidal integration formula evaluated over a logarithmically spaced frequency scale. The dB/dt response can be obtained by numerical differentiation of the derived $b(t)$ response. We could have obtained the dB/dt response directly through the Fourier transformation process if we had have used a rectangular convolution function in place of the linear ramp (the rectangular function is the derivative of the ramp-function). However, the sharp change in the rectangle function at either end point causes oscillations in the transformed response. It's more accurate to use the ramp function and then compute the derivative. The accuracy is also increased by allowing the waveform to ramp back-up as then there are no step changes in the waveform. We are only interested in the behavior during the turn-off ramp, so are not concerned with what happens afterwards.

APPENDIX C: REPRODUCTION OF INITIAL FEASIBILITY REPORT

Limits for magnetic localization of an EM transmitter coil.

David L Tilbrook

*CSIRO Division of Materials Science and Engineering**

(Dated: 2 October 2008)

Abstract

Intrinsic detector noise represents an intractable limit to the accuracy with which magnetic techniques can be used to provide information about the location of a magnetic dipole. Estimates of the localization precision have been carried out for high- T_c SQUID and low-noise flux-gate magnetometers, for coil systems and for SQUID based and flux-gate based magnetic gradiometers using the EM transmitter signal as an approximate magnetic dipole. It is shown that high- T_c SQUIDs provide the best performance with magnetometer-based localisation precision better than 10 cm for a realistic noise bandwidth at distances exceeding 50 m and less than 1 cm for distances up to about 40 m. The flux-gate magnetometer, by comparison, provides 10 centimeter localisation for distances of less than 25m, assuming a 100 Hz noise bandwidth, while the distance is restricted to less than 13 m for 1 cm localisation. The performance of coil-based systems was also examined briefly and found to be potentially superior to flux-gates for some EM pulse shapes.

The use of magnetic gradiometry to provide localization at 10 cm accuracy at distances approaching 30 m is possible only through the use of SQUID technology. Assuming a 100 Hz noise bandwidth, a 10 cm gradiometer baseline and a gradient noise density per unit baseline length of around $140\text{fT}/(\text{m}\sqrt{\text{Hz}})$, 10 cm localization is only achievable for distances up to around 20 m. The range can be increased to around 30 m for 30 cm localisation precision by increasing the gradiometer baseline length to 20 centimeters. By comparison, a low-noise flux-gate gradiometer with a 20 cm baseline length, can achieve 10 cm localisation only up to distances of around 11 m, increasing to 14 m for 30 centimeter localisation precision.

*PO Box 218, Lindfield, NSW, 2070, Australia; Electronic address: David.Tilbrook@CSIRO.au

Contents

I. Introduction	3
II. Magnetometer and gradiometer technology	3
A. Magnetic flux density as a function of distance.	4
1. EMI Tx signal.	4
B. Magnetic flux density	5
C. The first-order gradient tensor	6
III. Estimations of localization using the EMI transmit coil.	7
A. Localization precision limit imposed by magnetometer noise.	7
1. Bandwidth requirements and localization.	11
B. Other factors effecting magnetometer-based localization.	12
C. Localization precision limit for coil detector systems.	13
1. Precision estimates for the coil system.	17
D. Localization precision limit imposed by gradiometer noise.	17
1. Dipole on the x -axis	18
2. Gradiometer balance and system bandwidth	21
IV. Preliminary conclusions	25
V. Appendix - Geonics EM-63	27
VI. Appendix - Geonics EM-61	28
References	29

I. INTRODUCTION

Sky Research Inc. and CSIRO Division of Materials Science and Engineering have undertaken to conduct a proof-of-principle investigation to identify possible magnetic techniques by means of which it would be possible to determine the position (localization) and the orientation of an active EM-device used for the detection of unexploded ordinance (UXO). It has been shown [1], [2] that high signal-to-noise (SNR) ratios and centimeter-level positional accuracy are required of electromagnetic induction (EMI) systems to enable reliable discrimination between hazardous UXO and non-hazardous metallic items.

In theory, orientation information can be extracted by means of tiltmeters fitted to the UXO sensor, but in practice, these can be prone to drift and hysteresis, and while position information can be obtained through the use of grid setups and conventional surveying equipment, this is time-consuming in practice, and does not generally yield centimeter scale localization.

Use of the global positioning system (GPS) or line of sight laser technologies in conjunction with inertial motion units to provide orientation information, can provide localization accuracy which approaches, but generally does not meet, the required positional and orientation accuracy. Furthermore the performance of GPS-based systems can rapidly degrade in non ideal environments such as highly wooded terrains, under a dense tree canopy or under water.

The purpose of this work is to investigate the possibility for development of a new magnetic positioning system capable of providing positional information with accuracy of the order of 10 cm over baseline distances of up to 50 m, and with improved accuracy of the order of one centimeter, over shorter baselines. In principle, for baseline distances approximately 1 order of magnitude larger than the diameter of a transmitter coil, the controlled electromagnetic source employed for UXO detection provides an approximate dipole magnetic field, which can be measured to provide localisation and orientation information. The magnetic field deviates from that of a dipole for baseline distances approaching the diameter of the transmitter coil, and the effect of this on localisation accuracy will need to be taken into account.

II. MAGNETOMETER AND GRADIOMETER TECHNOLOGY

The potential localisation accuracy will depend on a number of factors but is ultimately limited by the sensitivity of the magnetic field sensors employed. The highest sensitivity magnetometers are based on superconducting technology and employ a superconducting quantum interference device

(SQUID) in conjunction with superconducting pickup loops. These systems are available in both low- and high- temperature superconducting technology, with noise spectral densities between $10 \text{ fT}/\sqrt{\text{Hz}}$ and $100 \text{ fT}/\sqrt{\text{Hz}}$ respectively; but high-temperature superconducting technology, requiring only a supply of liquid nitrogen as the liquid cryogen, offers the least impediment to practical implementation. The superconducting pick up loops employed in these devices may be configured in a number of different ways to form magnetometers, and planar- and axial-gradiometers.

The alternatives to superconducting technology capable of yielding vector information about the magnetic field include flux gate sensors and coil systems. Low noise flux-gate sensors have noise spectral densities approaching $5 \text{ pT}/\sqrt{\text{Hz}}$, approximately an order of magnitude inferior to superconducting technology, but with the advantage that no liquid cryogenic is required. As is shown below coil-based systems may also be viable and, depending upon the characteristics of the EM source, can have sensitivities superior to that of a flux gate sensor.

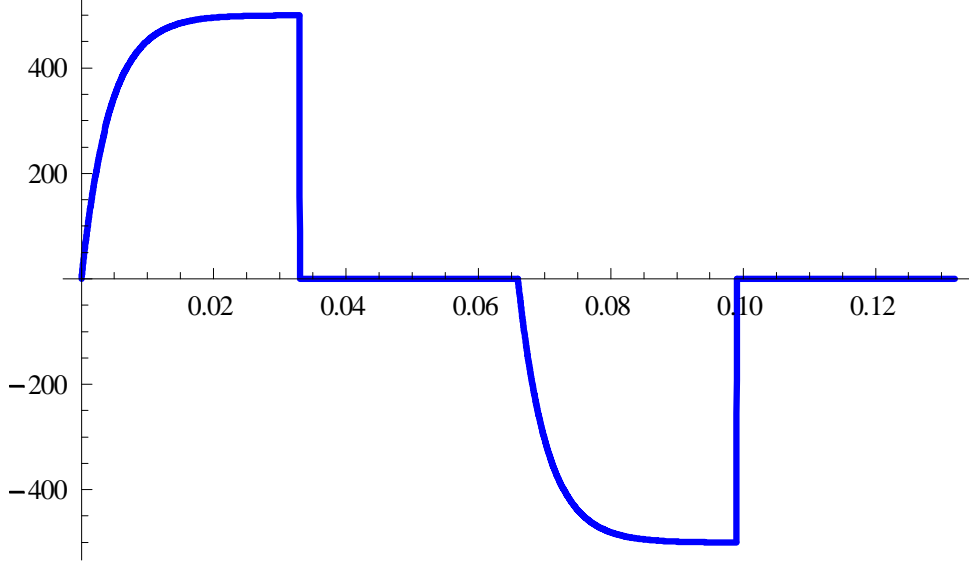
A. Magnetic flux density as a function of distance.

1. EMI Tx signal.

Consider an EM transmitter coil which is oriented approximately horizontally, i.e. its dipole moment, \mathbf{m} , is approximately vertical. The transmitter current is assumed to be bipolar and each half-cycle of the waveform may be broken into three distinct time intervals. For $t_0 \leq t < t_1$ the current rises exponentially, decreasing linearly to zero in the time interval $t_1 \leq t < t_2$ where it remains throughout $t_2 \leq t < t_3$. The second half-period mimics the first half, but is inverted. The magnetic moment may therefore be expressed as

$$m(t) = \begin{cases} m_0 (1 - e^{-(t-t_0)/\sigma}) & \text{if } t_0 \leq t < t_1 \\ m_0 (1 - e^{-(t_1-t_0)/\sigma}) \frac{t_2-t}{t_2-t_1} & \text{if } t_1 \leq t < t_2 \\ 0 & \text{if } t_2 \leq t < t_3 \\ -m_0 (1 - e^{-(t-t_3)/\sigma}) & \text{if } t_3 \leq t < t_4 \\ -m_0 (1 - e^{-(t_4-t_3)/\sigma}) \frac{t_5-t}{t_5-t_4} & \text{if } t_4 \leq t < t_5 \\ 0 & \text{if } t_5 \leq t < t_6 \end{cases} \quad (1)$$

For the Geonics EM-63 (see appendix V) $m_0 \doteq 512 \text{ Am}^2$, $\sigma = 4.3 \text{ mSec}$, and the repetition rates vary between: 7.5 Hz and 30 Hz. For the purpose of estimation take $t_1-t_0 = t_3-t_2 = t_4-t_3 = t_6-t_5 = 33 \text{ mSec}$, $t_2-t_1 = t_5-t_4 = 100 \mu\text{Sec}$, $\sigma = 4.3 \text{ mSec}$. The resulting transmit coil moment is plotted in fig II A 1.



B. Magnetic flux density

We consider the case of a $1\text{m} \times 1\text{m}$ square EM transmitter coil which is driven by the current waveform of the general type shown in figure (II A 1). Assume that the coil produces a peak dipole moment around 500 Am^2 .

Let $\mathbf{m} = m\mathbf{w}$, $m = |\mathbf{m}|$ and let $\mathbf{r} = r\mathbf{u}$, $r = |\mathbf{r}|$ be the displacement from the dipole to a point at which the magnetic flux density due to \mathbf{m} is measured. Vectors \mathbf{w} and \mathbf{u} are unit vectors in the directions of \mathbf{m} and \mathbf{r} , respectively. As is well known the flux density due to \mathbf{m} at \mathbf{r} is

$$\begin{aligned}\mathbf{B}(\mathbf{r}) &= \frac{\mu_0}{4\pi} \left(\frac{3(\mathbf{m} \cdot \mathbf{r})\mathbf{r}}{r^5} - \frac{\mathbf{m}}{r^3} \right) \\ &= \frac{\mu_0 m}{4\pi r^3} (3(\mathbf{w} \cdot \mathbf{u})\mathbf{u} - \mathbf{w})\end{aligned}\quad (2)$$

The magnitude of \mathbf{B} follows from

$$\begin{aligned}|\mathbf{B}|^2 &= \mathbf{B} \cdot \mathbf{B} = \left(\frac{\mu_0 m}{4\pi r^3} \right)^2 (3(\mathbf{w} \cdot \mathbf{u})\mathbf{u} - \mathbf{w}) \cdot (3(\mathbf{w} \cdot \mathbf{u})\mathbf{u} - \mathbf{w}) \\ &= \left(\frac{\mu_0 m}{4\pi r^3} \right)^2 (3(\mathbf{w} \cdot \mathbf{u})^2 + 1)\end{aligned}\quad (3)$$

hence

$$B \triangleq |\mathbf{B}| = \frac{\mu_0 m}{4\pi r^3} \sqrt{(3(\mathbf{w} \cdot \mathbf{u})^2 + 1)}, \quad (4)$$

or, if γ is the angle between \mathbf{w} and \mathbf{u}

$$B = \frac{\mu_0 m}{4\pi r^3} \sqrt{(3 \cos^2 \gamma + 1)}. \quad (5)$$

Two important special cases occur when $\mathbf{w} \perp \mathbf{u}$:

$$\left. \begin{aligned} \mathbf{B}_\perp &= -\frac{\mu_0 m}{4\pi r^3} \mathbf{w} \\ B_\perp &= \frac{\mu_0 m}{4\pi r^3} \end{aligned} \right\} \quad (6)$$

and when $\mathbf{w} \parallel \mathbf{u}$:

$$\left. \begin{aligned} \mathbf{B}_\parallel &= \frac{\mu_0 m}{2\pi r^3} \mathbf{u} = \frac{\mu_0 m}{2\pi r^3} \mathbf{w} \\ B_\parallel &= \frac{\mu_0 m}{2\pi r^3}. \end{aligned} \right\} \quad (7)$$

C. The first-order gradient tensor

The first-order gradient, \hat{g} , of a vector field in three dimensions is a second-rank tensor,

$$\hat{g} = \begin{pmatrix} g_{xx} & g_{xy} & g_{xz} \\ g_{yx} & g_{yy} & g_{yz} \\ g_{zx} & g_{zy} & g_{zz} \end{pmatrix}, \quad (8)$$

the components of which must satisfy Maxwell's equations. Its nine components: $g_{ij} \triangleq \partial B_i / \partial j$, $i, j = x, y, z$ are reduced to eight in the case of magnetic fields because

$$\mathbf{div}(\mathbf{B}) = 0 \Rightarrow g_{xx} + g_{yy} + g_{zz} = 0, \quad (9)$$

i.e. tensor is traceless. Also, from Ampere's law in a source free region,

$$\mathbf{curl}(\mathbf{B}) = \frac{1}{c^2} \frac{\partial \mathbf{E}}{\partial t} \Rightarrow \begin{cases} g_{zy} - g_{yz} = \frac{1}{c^2} \frac{\partial E_x}{\partial t} \\ g_{xz} - g_{zx} = \frac{1}{c^2} \frac{\partial E_y}{\partial t} \\ g_{yx} - g_{xy} = \frac{1}{c^2} \frac{\partial E_z}{\partial t} \end{cases} \quad (10)$$

so, assuming that contributions from changing electric fields in the vicinity of the gradiometer are small, we get that $g_{ij} \doteq g_{ji}$ when $i \neq j$, and the first-order gradient tensor is approximately symmetric. When combined with equation 1 only five of the gradient components are independent in this pseudo-static case. To determine the first-order gradient tensor it is therefore necessary to measure all five of these components, which may be done by deploying a suite of at least 5 intrinsic

gradiometers, a larger number of magnetometers with electronic differencing, or a combination of these.

The Cartesian components of the gradient tensor are then

$$g_{xx} = \partial_x B_x = \frac{3\mu_0}{4\pi} \frac{\left((y^2 - 4x^2 + z^2) (ym_y + zm_z) + m_x x (3(y^2 + z^2) - 2x^2) \right)}{(x^2 + y^2 + z^2)^{\frac{7}{2}}}, \quad (11)$$

$$g_{yy} = \partial_y B_y = \frac{3\mu_0}{4\pi} \frac{\left((x^2 - 4y^2 + z^2) (xm_x + zm_z) + m_y y (3(x^2 + z^2) - 2y^2) \right)}{(x^2 + y^2 + z^2)^{\frac{7}{2}}}, \quad (12)$$

$$g_{zz} = \partial_z B_z = \frac{3\mu_0}{4\pi} \frac{\left((x^2 + y^2 - 4z^2) (xm_x + ym_y) + m_z z (3(x^2 + y^2) - 2z^2) \right)}{(x^2 + y^2 + z^2)^{\frac{7}{2}}}, \quad (13)$$

$$g_{xy} = \partial_y B_x = \frac{3\mu_0}{4\pi} \frac{\left(-5m_z xyz + m_y x (z^2 + x^2 - 4y^2) + m_x y (y^2 + z^2 - 4x^2) \right)}{(x^2 + y^2 + z^2)^{\frac{7}{2}}}, \quad (14)$$

$$g_{yz} = \partial_z B_y = \frac{3\mu_0}{4\pi} \frac{\left(-5m_x xyz + m_z y (x^2 + y^2 - 4z^2) + m_y z (z^2 + x^2 - 4y^2) \right)}{(x^2 + y^2 + z^2)^{\frac{7}{2}}}, \quad (15)$$

$$g_{zx} = \partial_x B_z = \frac{3\mu_0}{4\pi} \frac{\left(-5m_y xyz + m_x z (y^2 + z^2 - 4x^2) + m_z x (x^2 + y^2 - 4z^2) \right)}{(x^2 + y^2 + z^2)^{\frac{7}{2}}}. \quad (16)$$

As has been previously pointed out [3], isolated magnetic dipoles can be localized by means of a number of analytic inversion algorithms based on measurement of the magnetic gradient [4] [5] [6]. The algorithm discussed by Wilson[6] is easily implemented, and when used with additional magnetometer information, or if multiple measurements are carried out at different locations, it is capable of yielding a unique localization solution.

III. ESTIMATIONS OF LOCALIZATION USING THE EMI TRANSMIT COIL.

A. Localization precision limit imposed by magnetometer noise.

Localization and orientation determination of the UXO transmitter coil requires determining the distance, pitch and roll of the UXO coil with respect to the reference station, but to obtain an estimate of the maximum potential localization accuracy, it is sufficient to consider the simplest possible localization procedure conceivable: use of equations 6 and 7 assuming knowledge of m .

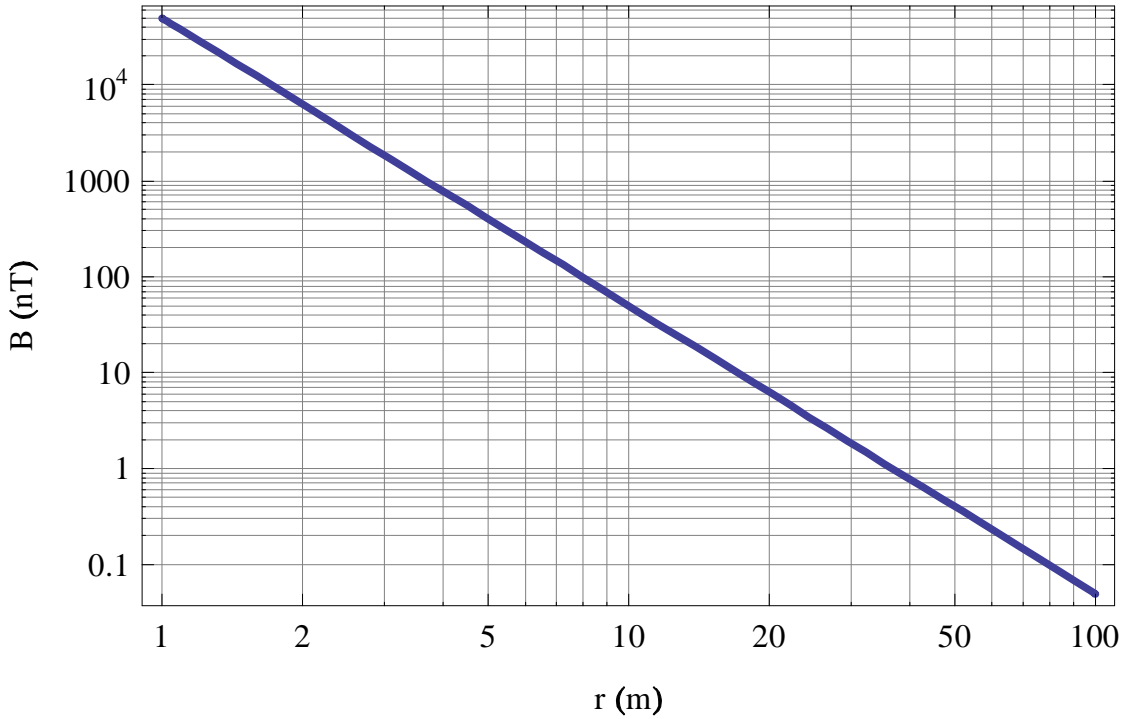


FIG. 1: Magnitude of the perpendicular component of the magnetic field as a function of distance.

Since the EMI Tx coil of the UXO transmitter is approximately horizontal, \mathbf{m} and \mathbf{r} are approximately normal (assuming flat terrain). As mentioned above, for the Geonics EM-63 (see appendix V) $m_0 \doteq 500 \text{ Am}^2$, so from equation 6

$$B_{\perp} \doteq \frac{\mu_0 m_0}{4\pi r^3} \doteq \frac{10^{-4}}{2r^3}, \quad (17)$$

which is graphed in figure 1.

In order to estimate the useable range of a magnetometer based localization system we solve equation 6 for r :

$$r = \sqrt[3]{\frac{\mu_0 m_0}{4\pi B_{\perp}}} \quad (18)$$

from which the uncertainty in the position due to an uncertainty in B is

$$\Delta r = -\frac{\Delta B_{\perp}}{3B_{\perp}} \sqrt[3]{\frac{\mu_0 m_0}{4\pi B_{\perp}}} = -\frac{r}{3B_{\perp}} \Delta B_{\perp} \quad (19)$$

or

$$\Delta r = -\frac{4\pi \Delta B_{\perp}}{3\mu_0 m_0} r^4; \quad (20)$$

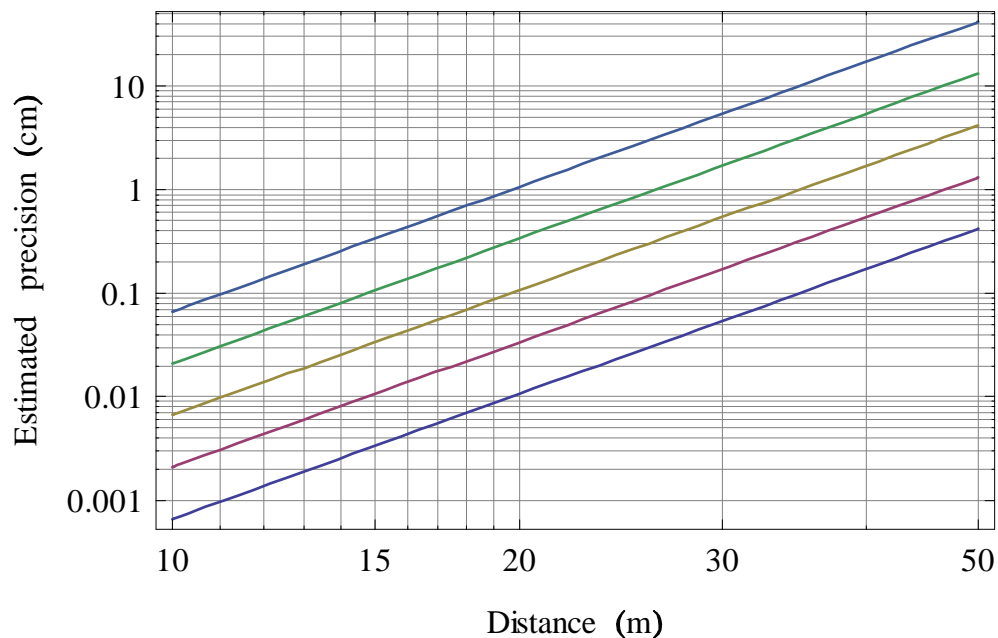
i.e. the uncertainty in position which results from an uncertainty in the measurement of the magnitude of the magnetic flux density is proportional to the forth power of the distance.

If the intrinsic noise of the detectors dominates, the resulting positional-error spectral density which follows from equation 19 are shown in the following tables for both a high-temperature SQUID (assumed noise density $100 \text{ fT}/\sqrt{\text{Hz}}$) and a low-noise flux-gate (assumed noise density $5 \text{ pT}/\sqrt{\text{Hz}}$):

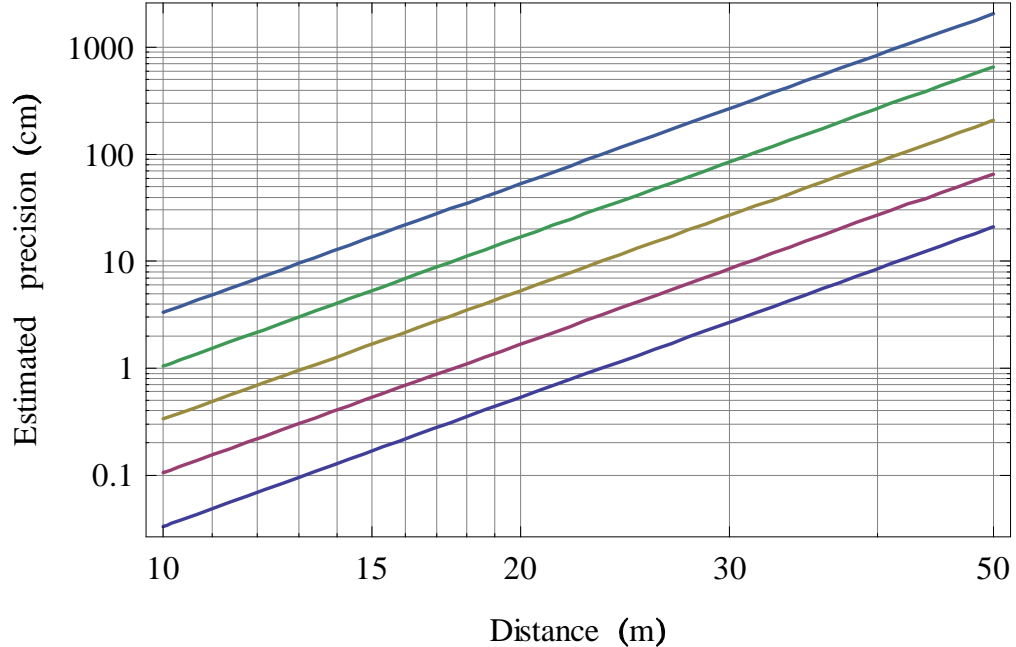
r (m)	B_{\perp} (nT)	SQUID for $\Delta B_{\perp} = 100 \text{ fT}/\sqrt{\text{Hz}}$	Flux-gate for $\Delta B_{\perp} = 5 \text{ pT}/\sqrt{\text{Hz}}$
5	400	4.2×10^{-5}	2.1×10^{-3}
10	50	6.7×10^{-4}	3.3×10^{-2}
15	14.8	3.4×10^{-3}	0.17
20	6.25	1.1×10^{-2}	0.53
25	3.2	2.6×10^{-2}	1.3
30	1.85	5.4×10^{-2}	2.7
35	1.15	0.10	5.1
40	0.78	0.17	8.6
45	0.55	0.27	14
50	0.4	0.42	21

The corresponding positional accuracies will depend on the required noise bandwidth and are graphed in figures III A and III A for noise bandwidths of 1 Hz, 10 Hz, 100 Hz, 1kHz and 10kHz.

Estimated maximum localization precision (cm)
for a high-T_c SQUID (100fT/√Hz) as a function of distance,
for noise bandwidths 1Hz,10Hz,100Hz,1kHz,10kHz.



Estimated maximum localization precision (cm)
 or a low-noise flux-gate ($5\text{pT}/\sqrt{\text{Hz}}$) as a function of distance
 for noise bandwidths 1Hz, 10Hz, 100Hz, 1kHz, 10kHz.



1. Bandwidth requirements and localization.

Assuming the EM system is moved at approximately 1m/s, a localization of 1 cm will require a system bandwidth of at least 100 Hz, and in a practical system, employing digital sampling of the TEM transmitter signal, the system bandwidth will need to be considerably greater. At 100 Hz bandwidth, from figures 3 and 4, the estimated maximum localization precision is around 1 cm at a distance of 33 m, degrading only to 4 cm at 50 m for the high-temperature SQUID. The performance of the flux-gate system is significantly inferior, achieving 1cm localization at a distance of 13 m and around 10 cm localization at a distance of only 23 m. If a digital sampling system is used to capture the EM waveform and it is necessary to increase the system bandwidth to say 10kHz, the high-temperature SQUID system still provides a maximum localization precision of 1 cm at a useful distance around 20m, and 10cm at around 33m, while the flux-gate system achieves 1 cm precision for distances around 5 m and 10 cm precision at 13 m.

B. Other factors effecting magnetometer-based localization.

The estimates of localization precision given are based on the intrinsic white noise of the magnetometers. Both SQUIDs and flux-gates exhibit low-frequency noise with an approximate $1/f$ noise density spectrum, which will degrade the noise performance at low-frequencies. Further, since the magnetometers are operated in the geophysical magnetic field, B_E , in excess of around 50,000 nT, any vibrations or movement that lead to rotation of the magnetometers will further degrade the noise performance and hence the localization precision. Vector magnetometers are most sensitive to these effects when the direction of the background magnetic field is approximately normal to the direction of the magnetometer sensitivity vector. i.e. when the coupling is least. Since the coupled magnetic field is $B_E \cos \chi$ where χ is the angle between the magnetic field and the effective area, and $\chi \neq \pi/2$, the coupled field is approximately given by χB_E . So, depending on the noise spectrum density, vibrations which give rise to rotations of the magnetometer of only 2 nRad for the high-temperature SQUID and 100 nRad for a low-noise flux-gate will potentially degrade the localization precision by 3 dB.

Another factor effecting the choice of magnetometer technology is dynamic range. Flux-gates are "true" magnetometers, so operation in the large geophysical background field requires that the system be capable of the full dynamic range extending from the noise floor of around 50 pT for a 100Hz bandwidth system to over 50,000 nT - a dynamic range of over 120 dB or around 21 bits.

In this application, however, the dynamic range requirements for SQUID-based systems can be relaxed considerably, compared to flux-gate systems, because during operation the magnetometer is stationary. As mentioned briefly above, a directly-coupled SQUID-based magnetometer employs a superconducting pick-up loop as the primary detector of the magnetic field. In the presence of magnetic fields a Meissner shielding current is induced in the pick-up loop which is proportional to the projection of the magnetic field onto the direction of the effective area vector of the pick-up loop. This current is sensed using the SQUID, which in these devices, operates as a transimpedance amplifier - producing an output voltage in response to an input current. If, once the directly-coupled SQUID magnetometer is located at its reference position, the device is reset by heating the pick-up loop momentarily above its superconducting transition temperature, magnetic flux due to the geophysical background fills the pick-up loop. Upon re-cooling below the transition temperature the Meissner effect locks this flux into the pick-up loop, establishing only sufficient current to quantize the flux to an integral number of flux quanta, and establishing a stable offset flux in the device which greatly reduces the required dynamic range.

C. Localization precision limit for coil detector systems.

It may also be possible to use a system of coils in conjunction with the EM Tx signal for localization. The coil electromotance is given by Neumann's law

$$\mathcal{E} = -\frac{\partial \Phi}{\partial t} \quad (21)$$

and

$$\Phi \doteq NAB \quad (22)$$

where A is the geometric area of the coil, N is the number of turns, and we have assumed an approximately homogeneous magnetic flux density in the vicinity of the coil given by equation 6

$$B_{\perp} = \frac{\mu_0 m(t)}{4\pi r^3}.$$

The flux in the vicinity of the coil is therefore approximately given by

$$\Phi \doteq NA \frac{\mu_0 m(t)}{4\pi r^3} \quad (23)$$

and its rate of change is

$$\frac{\partial \Phi}{\partial t} \doteq NA \frac{\mu_0}{4\pi r^3} \frac{\partial}{\partial t} m(t) \quad (24)$$

Use of equation 21 then gives

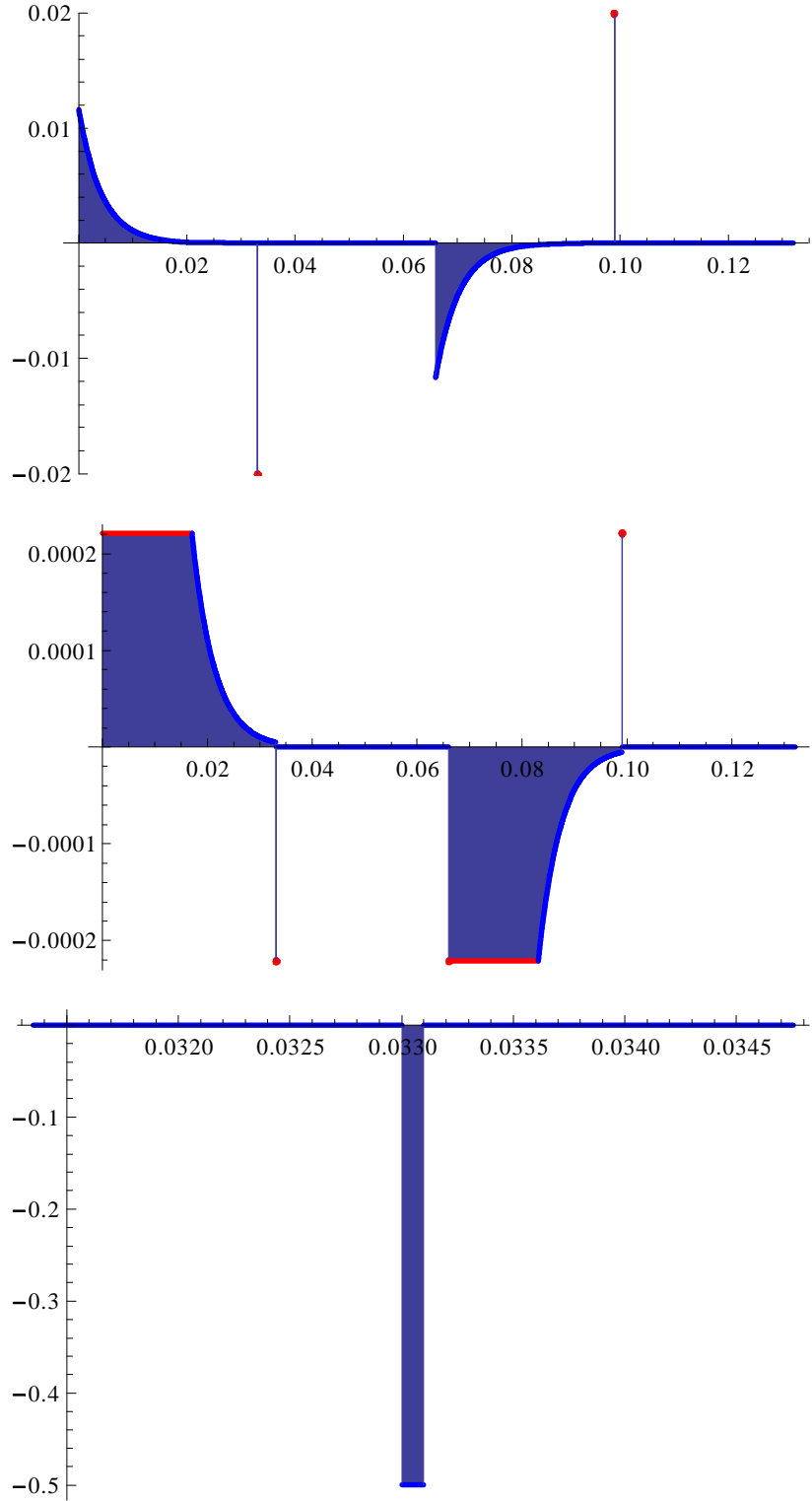
$$\mathcal{E} = \frac{\mu_0 m_0 N A}{4\pi r^3} \begin{cases} -\frac{1}{\sigma} \exp(-(t-t_0)/\sigma) & \text{if } t_0 \leq t < t_1 \\ -\left(\frac{1}{t_2-t_1} \left(\exp\left(-\frac{t_1-t_0}{\sigma}\right) - 1\right)\right) & \text{if } t_1 \leq t < t_2 \\ 0 & \text{if } t_2 \leq t < t_3 \\ \frac{1}{\sigma} \exp((t_3-t)/\sigma) & \text{if } t_3 \leq t < t_4 \\ \left(\frac{1}{t_5-t_4} \left(\exp\left(\frac{t_3-t_4}{\sigma}\right) - 1\right)\right) & \text{if } t_4 \leq t < t_5 \\ 0 & \text{if } t_5 \leq t < t_6 \end{cases} \quad (25)$$

As above, choose $t_1 - t_0 = t_3 - t_2 = t_4 - t_3 = t_6 - t_5 = 33$ mSec, $t_2 - t_1 = t_5 - t_4 = 100$ μ Sec, $m_0 \doteq 512 \text{ Am}^2$, $\sigma = 4.3 \text{ mSec}$, similar to the Tx waveform used in the Geonics EM-63 operating in

mode "M" at 7.5 Hz repetition rate, and let $t_0 = 0$. Then

$$\mathcal{E} = \frac{NA}{r^3} \begin{cases} -1.1907 \times 10^{-2} \exp(-232.56t) & \text{if } 0 \leq t < 0.033 \\ 0.51176 & \text{if } 0.033 \leq t < 0.0331 \\ 0 & \text{if } 0.0331 \leq t < 0.066 \\ 1.1907 \times 10^{-2} \exp(15.349 - 232.56t) & \text{if } 0.066 \leq t < 0.099 \\ -0.51176 & \text{if } 0.099 \leq t < 0.0991 \\ 0 & \text{if } 0.0991 \leq t < 0.132 \end{cases} \quad (26)$$

which is graphed in figures III C, III C and III C for $N = 10$, $A = 0.1 \text{ m}^2$ at $r = 1 \text{ m}$.



The magnitude of the coil voltage is a maximum on the intervals $t_1 \leq t < t_2$ and $t_4 \leq t < t_5$, during which

$$|\mathcal{E}| \doteq 0.51 \frac{NA}{r^3} . \quad (27)$$

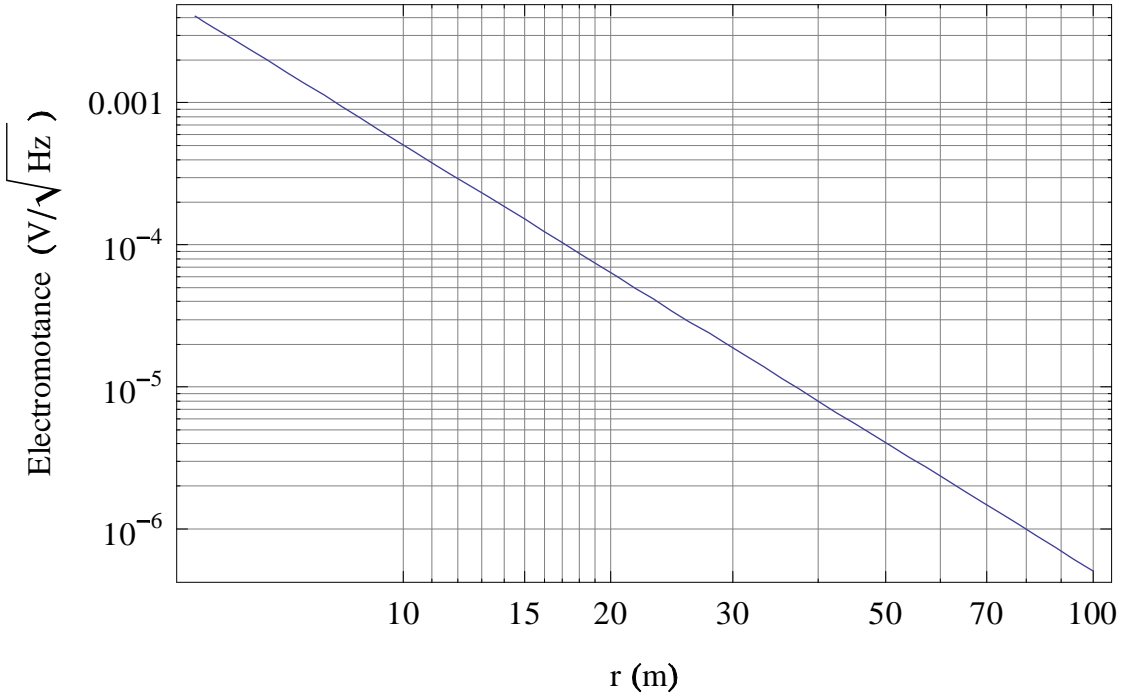


Figure III C graphs the induced electromotance spectral density as a function of r , for $NA = 1$.

Equation 27 may be solved for r :

$$r \doteq \left(0.51 \frac{NA}{|\mathcal{E}|} \right)^{1/3} \quad (28)$$

and potentially used for localization. The uncertainty in position which results from an uncertainty in electromotance is approximately

$$\Delta r = 0.267 \sqrt[3]{\left(\frac{NA}{\mathcal{E}^4} \right)} \Delta \mathcal{E} \quad (29)$$

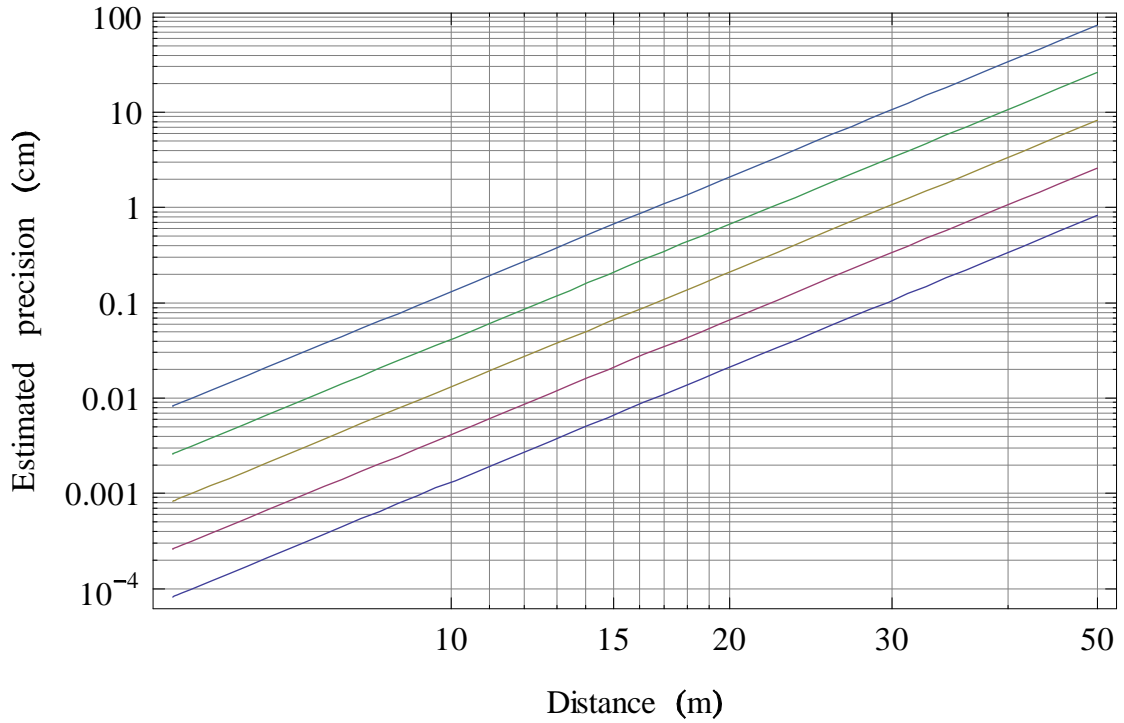
or

$$\Delta r = 0.66 \frac{r^4}{AN} \Delta \mathcal{E} \quad (30)$$

In a well designed system, for a given detector coil, the limit of precision will be determined by the total equivalent input noise of the first stage analogue preamplifier used to amplify the coil signal. The best low-noise preamplifiers have noise spectral densities approaching 2 nV/sqrt(Hz) in this frequency range, from which the resulting positional-error spectral density is

$$\Delta r = 1.32 \times 10^{-9} \frac{r^4}{AN} (m) / \sqrt{Hz} \quad (31)$$

which is graphed in figure III C for noise bandwidths of 1 Hz, 10 Hz, 100 Hz, 1kHz and 10kHz, and assuming $NA = 1$.



1. *Precision estimates for the coil system.*

Assuming a 100 Hz noise bandwidth, as above, yields an estimated maximum precision around 1cm at 30 m and under 10cm at 50 m. It should be noted, however, that the sensitivity of the coil system relies on the fast t_{off} time of the EM signal to generate considerable electromotance in the localization pick-up coils, which is likely to be strongly affected by environmental factors such as ground conductivity and the presence of UXO and non-hazardous non-UXO targets.

D. Localization precision limit imposed by gradiometer noise.

Using the spherical polar coordinates, (r, ϕ, θ) , in which ϕ is the colatitude and θ is the azimuthal angle,

$$x = r \cos \theta \sin \phi$$

$$y = r \sin \theta \sin \phi$$

$$z = r \cos \phi$$

and from equations 11-16 ?? the components of the gradient may be brought to the forms:

$$g_{xx} = \frac{3\mu_0}{16\pi r^4} \begin{pmatrix} 4m_z \cos^3(\phi) + 4(3m_x \cos(\theta) + m_y \sin(\theta)) \sin(\phi) \cos^2(\phi) \\ -2m_z(5 \cos(2\theta) + 3) \sin^2(\phi) \cos(\phi) \\ -(3m_x \cos(\theta) + 5m_x \cos(3\theta) + m_y(\sin(\theta) + 5 \sin(3\theta))) \sin^3(\phi) \end{pmatrix} \quad (32)$$

$$g_{yy} = \frac{3\mu_0}{16\pi r^4} \begin{pmatrix} 4m_z \cos^3(\phi) + 4(m_x \cos(\theta) + 3m_y \sin(\theta)) \sin(\phi) \cos^2(\phi) \\ +2m_z(5 \cos(2\theta) - 3) \sin^2(\phi) \cos(\phi) \\ +(-m_x \cos(\theta) + 5m_x \cos(3\theta) - 3m_y \sin(\theta) + 5m_y \sin(3\theta)) \sin^3(\phi) \end{pmatrix} \quad (33)$$

$$g_{zz} = -\frac{3\mu_0}{16\pi r^4} \begin{pmatrix} (3m_z \cos(\phi) + 5m_z \cos(3\phi)) \\ +(m_x \cos(\theta) + m_y \sin(\theta))(\sin(\phi) + 5 \sin(3\phi)) \end{pmatrix} \quad (34)$$

$$g_{xy} = \frac{3\mu_0}{4\pi r^4} \sin(\phi) \begin{pmatrix} (m_y \cos(\theta) + m_x \sin(\theta)) \cos^2(\phi) \\ -5m_z \cos(\theta) \sin(\theta) \sin(\phi) \cos(\phi) \\ -\frac{1}{4}(m_y \cos(\theta) - 5m_y \cos(3\theta)) \\ +m_x(\sin(\theta) + 5 \sin(3\theta)) \sin^2(\phi) \end{pmatrix} \quad (35)$$

$$g_{yz} = \frac{3\mu_0}{8\pi r^4} \begin{pmatrix} 2m_y \cos^3(\phi) - 8m_z \sin(\theta) \sin(\phi) \cos^2(\phi) \\ +(5 \cos(2\theta)m_y - 3m_y - 5m_x \sin(2\theta)) \sin^2(\phi) \cos(\phi) \\ +2m_z \sin(\theta) \sin^3(\phi) \end{pmatrix} \quad (36)$$

$$g_{zx} = \frac{3\mu_0}{8\pi r^4} \begin{pmatrix} 2m_x \cos^3(\phi) - 8m_z \cos(\theta) \sin(\phi) \cos^2(\phi) \\ -(5 \cos(2\theta)m_x + 3m_x + 5m_y \sin(2\theta)) \sin^2(\phi) \cos(\phi) \\ +2m_z \cos(\theta) \sin^3(\phi) \end{pmatrix} \quad (37)$$

1. Dipole on the x -axis

In order to estimate the localization accuracy afforded by the use of gradiometry let the dipole be located on the x -axis. Then $\theta = 0$ and $\phi = \pi/2$, and equations 1 - 6 reduce to

$$g_{xx} = -\frac{3\mu_0 m_x}{2\pi r^4} \quad (38)$$

$$g_{yy} = \frac{3\mu_0 m_x}{4\pi r^4} \quad (39)$$

$$g_{zz} = \frac{3\mu_0 m_x}{4\pi r^4} \quad (40)$$

$$g_{xy} = \frac{3\mu_0 m_y}{4\pi r^4} \quad (41)$$

$$g_{yz} = 0 \quad (42)$$

$$g_{zx} = \frac{3\mu_0 m_z}{4\pi r^4} \quad (43)$$

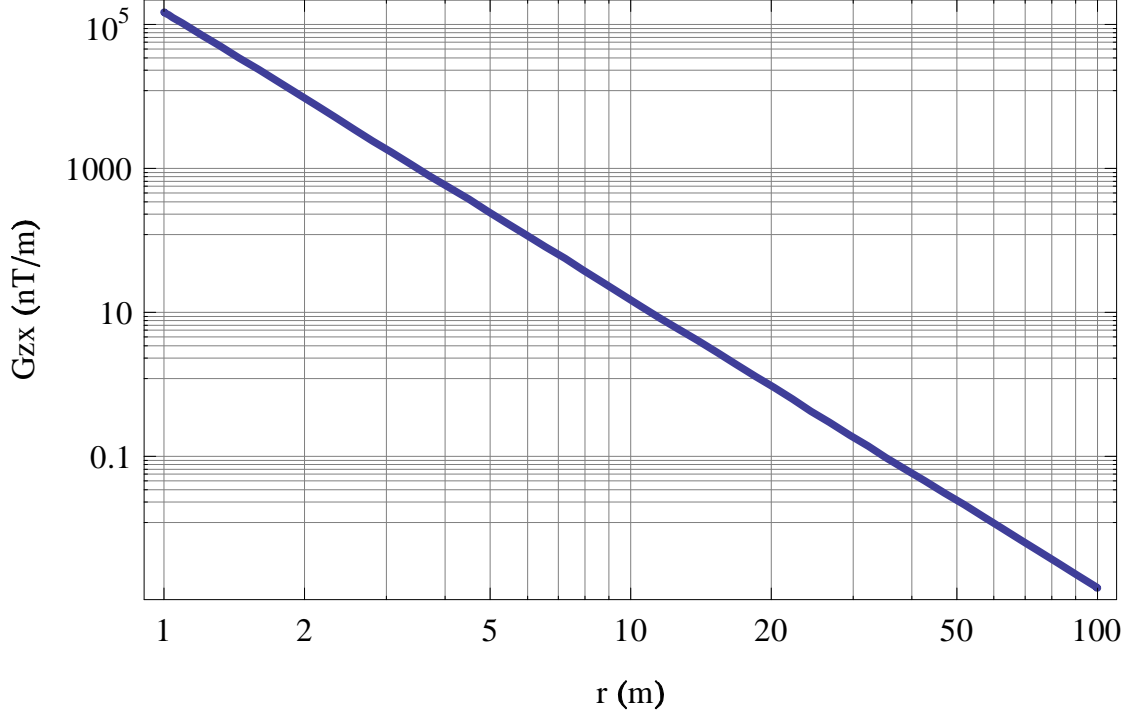
If the dipole is directed vertically, as above, then $m_x = m_y = 0$, and $m_z = m_0$, $g_{xx} = g_{yy} = g_{zz} = g_{xy} = g_{yz} = 0$, and

$$g_{zx} = \frac{3\mu_0 m_0}{4\pi r^4}. \quad (44)$$

With $m_0 = 500 \text{ Am}^2$

$$g_{zx} = \frac{0.00015}{r^4}$$

which is graphed in figure III D 1



Magnitude of the g_{zx} component of the first-order gradient tensor as a function of distance.

In order to estimate the useable range of a gradiometer based localization system we solve equation 44 for r :

$$r = \sqrt[4]{\frac{3\mu_0 m_0}{4\pi g_{zx}}} \quad (45)$$

from which the uncertainty in the position due to an uncertainty in g_{zx} is

$$|\Delta r| = \frac{\Delta g_{zx}}{4g_{zx}} \sqrt[4]{\frac{3\mu_0 m_0}{4\pi g_{zx}}} = \frac{r}{4g_{zx}} \Delta g_{zx} \quad (46)$$

or

$$|\Delta r| = \frac{1}{3} \frac{\pi \Delta g_{xz}}{m_0 \mu_0} r^5. \quad (47)$$

The uncertainty in position which results from an uncertainty in the measurement of the g_{zx} component of the first-order magnetic gradient is proportional to the fifth power of the distance.

If the intrinsic noise of the detectors dominate, the resulting positional-error spectral density which follows from equation 47 are shown in the following table for gradiometers formed by electronic differencing of a pair of high-temperature SQUIDs and a pair of low-noise flux-gates. The noise spectrum of the magnetometers comprising the gradiometers are assumed to be white and uncorrelated, so the resulting noise spectral density figures for the gradiometers is

$$\Delta g_{xz} = \sqrt{2} \Delta B/d \quad (48)$$

where d is the baseline distance of the gradiometer. The gradiometer noise density figures are therefore taken to be $(140/d)$ fT/ $(\text{m}\sqrt{\text{Hz}})$ and $(7/d)$ pT/ $(\text{m}\sqrt{\text{Hz}})$ for the SQUID and flux-gate systems respectively.

r (m)	g_{zx} (nT/m)	SQUID $ \Delta r (cm) / \sqrt{Hz}$ for $\Delta g_{zx} = 140/d fT / (m\sqrt{Hz})$	Flux-gate $ \Delta r (cm) / \sqrt{Hz}$ for $\Delta g_{zx} = 7/d pT / (m\sqrt{Hz})$
5	240	7.293125×10^{-5}	3.645834×10^{-3}
10	15.0	0.0023338	0.1166667
15	2.96	1.772229×10^{-2}	0.8859377
20	0.938	0.0746816	3.733334
25	0.384	0.2279102	11.39323
30	0.185	0.5671134	28.35001
35	0.100	1.225756	61.27553
40	0.0586	2.389811	119.4667
45	0.0366	4.306517	215.2829
50	0.024	7.293125	364.5834

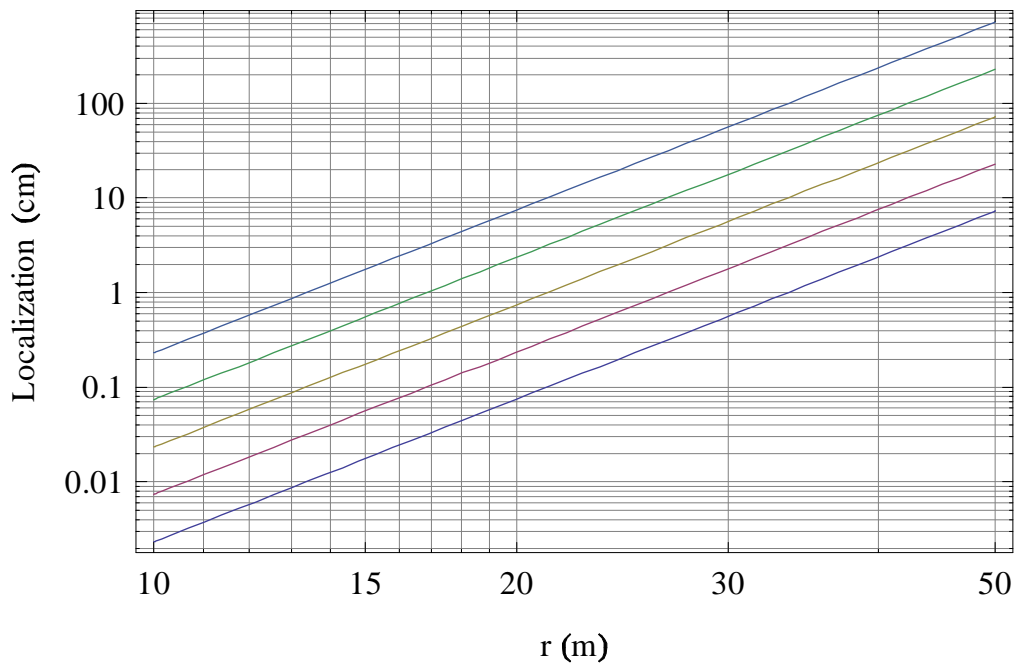
2. Gradiometer balance and system bandwidth

The ultimate positional accuracies of gradiometer-based systems will depend on both the required noise bandwidth and the gradiometer baseline distance. Although in theory, gradiometers with large baseline distances have more sensitivity, this is not generally true in practice. A major limitation encountered with practical gradiometers is their finite gradiometer balance, which generally degrades strongly as a function of increasing distance, and which leads to contamination of gradient measurements by background magnetic fields. Even superconducting gradiometers fabricated with micron scale lithography on rigid substrates, and with gradiometer baselines of only a few centimeters, commonly achieve gradiometer balances of only order 10^3 . Such a gradiometer, deployed in the geophysical background field of say $60\mu T$, will exhibit a magnetic contamination error of around $\pm 60nT$; equivalent to an error gradient of order $\pm 1000nT$ for a gradiometer with a 6 cm baseline - around four orders of magnitude greater than the gradient expected at a distance of 30 metres.

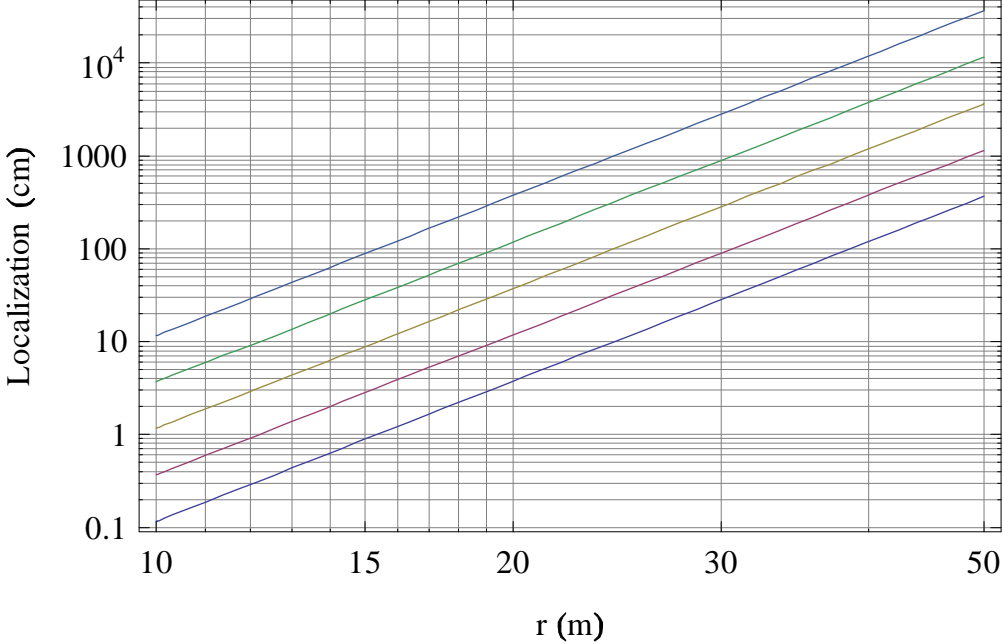
High-quality integrated SQUID-based gradiometers typically have baselines of only a few centimeters and have gradient sensitivities limited by SQUID noise of around $0.01\text{nT}/(m\sqrt{Hz})$ and gradiometer balance around 10^3 . Systems employing discrete magnetometers with electronic differencing and 10cm baselines, for example, seldom exceed a gradiometer balance of 10^2 . In practice, it is very difficult to achieve acceptable gradiometer performance for either SQUID or flux-gate

systems with baselines longer than 30cm. Figures III D 2 and III D 2 show graphs of the maximum localization precision available for SQUID-based and flux-gate based gradiometers as a function of noise bandwidth and baseline distance.

Estimated maximum localization precision (cm) per unit
 of baseline length for a SQUID gradiometer ($140\text{fT}/(\text{m}\sqrt{\text{Hz}})$)
 as a function of distance, for noise bandwidths
 1Hz, 10Hz, 100Hz, 1kHz, 10kHz.



Estimated maximum localization precision (cm) per unit of baseline length for a flux–gate gradiometer ($7\text{pT}/(\text{m}\sqrt{\text{Hz}})$) as a function of distance, for noise bandwidths 1Hz,10Hz,100Hz,1kHz,10kHz.

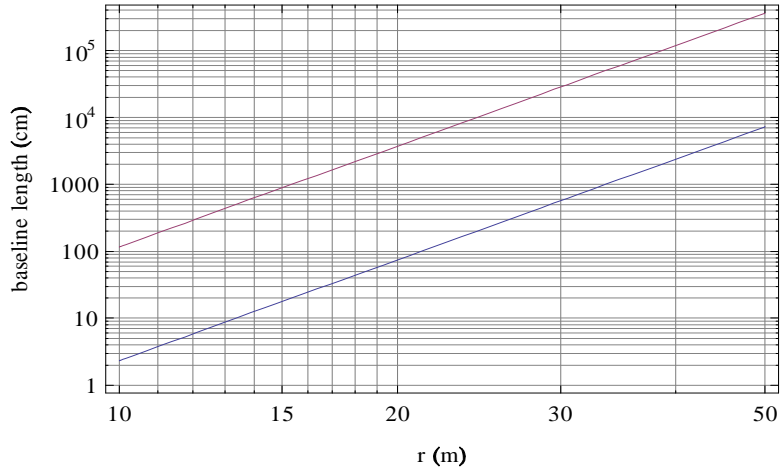


Using equations 47 and 48 and solving for the baseline distance gives

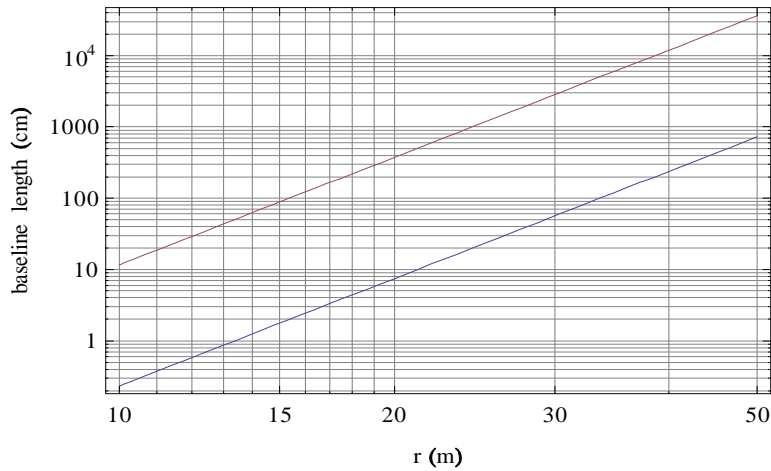
$$d = \frac{1}{3} \frac{\pi \Delta g_{zx} \Delta f}{m_0 \mu_0 \Delta r} r^5 \quad (49)$$

where Δf is the noise bandwidth of the system. Using this equation Figures III D 2, III D 2 and III D 2 show the required gradiometer baseline distances to achieve localization precisions of 1 cm, 10 cm and 30 cm, respectively, assuming a 100 Hz noise bandwidth for both the SQUID and flux-gate based gradiometer systems.

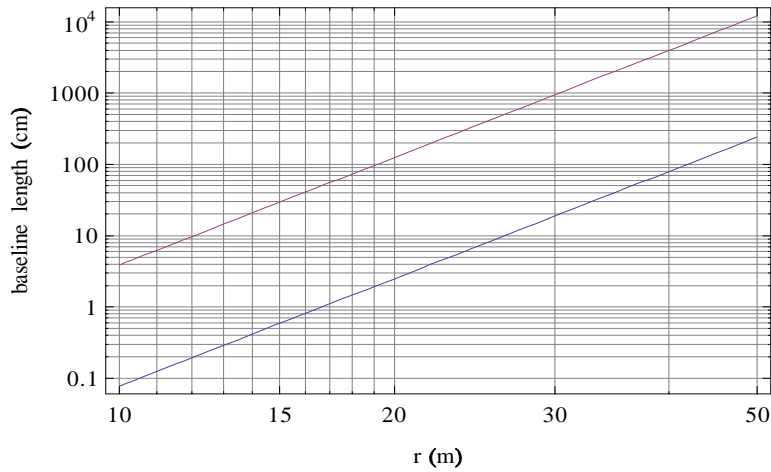
Estimated gradiometer baseline as a function
of distance for 1 cm localization (100Hz noise bandwidth)



Estimated gradiometer baseline as a function
of distance for 10cm localization (100Hz noise bandwidth)



Estimated gradiometer baseline as a function
of distance for 30cm localization (100Hz noise bandwidth)



IV. PRELIMINARY CONCLUSIONS

Although many factors will influence the localization precision that can be achieved by magnetic techniques, the intrinsic detector noise represents a relatively intractable limit. Estimates of the localisation precision have been carried out for high- T_c SQUID and low-noise flux-gate magnetometers, for coil systems and for SQUID based and flux-gate based magnetic gradiometers using the EM transmitter signal as approximate magnetic dipole. As expected, magnetometry provides superior localisation due to the slower fall-off is a function of distance when compared to gradiometry.

High- T_c SQUIDs with noise densities around $100 \text{ fT}/\sqrt{\text{Hz}}$ provide the best performance. When configured as a magnetometer the limit of localisation precision falls well inside the required specification of 10 cm for realistic noise bandwidths at distances exceeding 50 m, and is less than 1 cm for distances up to about 40 m. Assuming a 100 Hz noise bandwidth the flux-gate magnetometer, by comparison, provides 10 centimeter localisation for distances of less than 25 m, decreasing to less than 13 m for 1 cm localisation.

It has been shown that in theory, when combined with a fast changing EM pulse, coil systems can provide localisation precision which is superior to a flux gate. It is likely, however, that coil-based systems will exhibit dependence on environmental factors which effect the rate of change of the magnetic field, such as ground conductivity and the presence of UXO and non-hazardous UXO targets.

The use of magnetic gradiometry to provide localisation at 10 cm accuracy at distances approaching 30 m is possible only through the use of SQUID technology. Assuming a 100 Hz noise bandwidth, a 10 cm gradiometer baseline and a gradient noise density per unit baseline length of around $140 \text{ fT}/(\text{m}\sqrt{\text{Hz}})$, 10 cm localisation is only achievable for distances up to around 20 m. The range can be increased to around 30 m for 30 cm localisation precision by increasing the gradiometer baseline length to 20 centimeters. By comparison, a low-noise flux gate gradiometer with a 20 cm baseline length, can achieve 10 cm localisation only up to distances of around 11 m, increasing to 14 m for 30 centimeter localisation precision.

Although magnetometry provides superior localisation than gradiometry, due to the slower fall-off is a function of distance, it should be noted that this work has not addressed issues associated with the solution of the inverse problem, and it has been assumed throughout that the magnitude of the dipole moment is known. The orientation of the dipole moment may need to be determined by tilt meters fitted to the UXO cart, but it may also be possible to solve for the

dipole moment uniquely by use of a combination of magnetometer and gradiometer measurements. This will be addressed in future work.

V. APPENDIX - GEONICS EM-63

Specifications:

- Transmitter 1m^2 square loop.
- Peak moment: 512 Am^2 (1024 Am^2 P-P)
- Charging pulse: $1 - \exp(- (t - 1) / (4.3 \times 10^{-3}))$
- 26 time gates of secondary response in mV

covering range from $180\mu\text{s}$ to 25 ms.

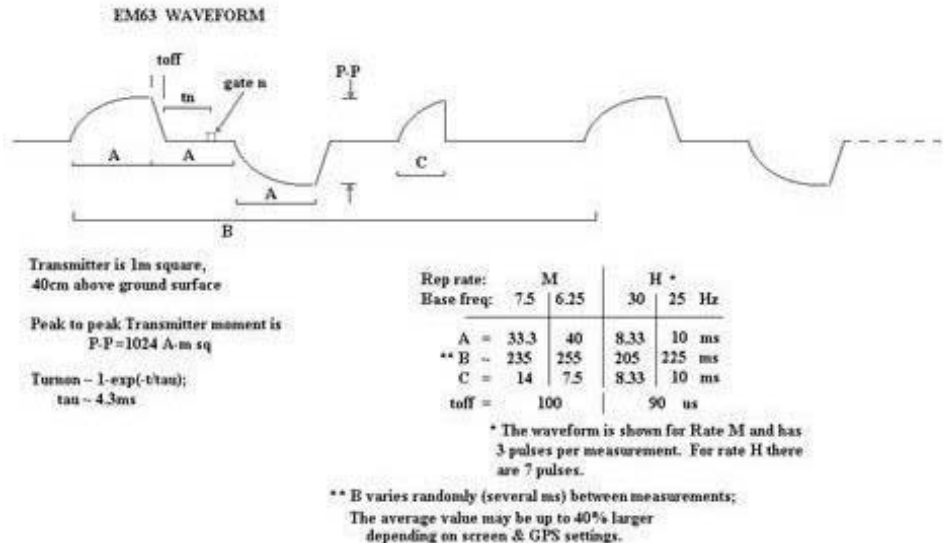
- Air-cored coil, 1×1 metre size
- Bipolar rectangular current
- Measured Quantities 26 time gates of secondary response in mV

covering range from $180\mu\text{s}$ to 25 ms

- EM Source Air-cored coil, 1×1 metre size

EM Sensors

- 1. Main: Air-cored coil, 0.5×0.5 m in size, coincident with EM source
- 2. Focusing: Air-cored coil, 0.5×0.5 m in size, 60 cm above main coil
- 3. Gates 2 - 10 in the EM63 are $180\text{-}689\mu\text{Sec}$
- 4. Measuring Ranges 10,000 mV
- 5. Dynamic Range 18 bits



VI. APPENDIX - GEONICS EM-61

Specifications

MEASURED QUANTITY Four channels of secondary response in mV

EM SOURCE Air-cored coil, $1 \times 0.5\text{m}$ size

CURRENT WAVEFORM Unipolar rectangular current with 25% duty cycle

EM SENSORS Bottom coil: Air-cored coil, $1 \times 0.5\text{ m}$ in size,
coincident with EM source

Top coil: Air-cored coil, $1 \times 0.5\text{ m}$ in size

28 cm above main coil

MAXIMUM OUTPUT 10 000 mV

DYNAMIC RANGE 18 bits

TIME GATES Four gates of bottom coil response only,
centered at 216, 366, 660 and $1266\mu\text{sec}$; or,
three gates of bottom coil response at 216,
366 and $660\mu\text{sec}$, with one gate of top coil
response at $660\mu\text{sec}$.

- [1] Smith, J. T., H. F. Morrison and A. Becker, 2004, Resolution Depths for Some Transmitter-Receiver Configurations, IEEE Trans. Geosc. & Rem. Sen., 42(6), pp. 1215-1221.
- [2] Bell, T., 2005, Geo-location Requirements for UXO Discrimination: Paper prepared for UXO Location Workshop, Annapolis, May 2005.
- [3] Billings, S.D., Leslie K.E., Schmidt P.W., 2008, SERDP proposal, SON MMSEED-08-01.
- [4] Frahm, C.P., 1972, Inversion of the magnetic field gradient equation for a magnetic dipole field: NCSL Informal Report, 135-72.
- [5] Wynn, W.M., Frahm, C.P., Carroll, P.J., Clark, R.H., Wellhoner, J., and Wynn, M.J., 1975, Advanced superconducting gradiometer/magnetometer arrays and a novel signal processing technique: IEEE Trans. Mag., MAG-11, 701-707.
- [6] Wilson, H., 1985, Analysis of the magnetic gradient tensor. Defence Research Establishment Pacific: Canada Technical Memorandum, 85-13, 47.